

Typeset in [L<sup>A</sup>T<sub>E</sub>X 2 <sub>\$\epsilon\$</sub>](#) .  
Copyright © 2024 Laksh Gupta.  
All Rights Reserved.

# **Study of White Dwarfs in NGC2808**

*Submitted towards Partial Fulfilment of  
the Requirements for the Degree of*

BACHELORS OF SCIENCE (HONOURS)

*with a Major in*

PHYSICS

*to the*

Division of Mathematical and Physical Sciences  
School of Arts & Sciences  
Ahmedabad University

*by*

LAKSH GUPTA  
(AU2020152)

*under the supervision of*

PROFESSOR SAMYADAY CHOUDHURY

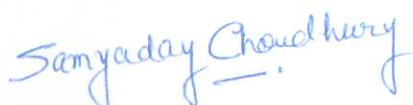


APRIL 2024

# Declaration / Approval Form

This thesis of Laksh Gupta, submitted for the degree of Bachelor of Science (Honours) with a Major in Physics and titled "Study of White Dwarfs in NGC2808," has been reviewed in final form. As indicated by the signatures and dates below, permission is now granted to submit final copies to the College of Undergraduate Studies for approval.

## Review Committee:



Date of Signature

13.05.2024

Samyaday Choudhury  
Assistant Professor, Division of Mathematical and  
Physical Sciences, School of Arts & Sciences,  
Ahmedabad University.  
Thesis Advisor



20.05.2024

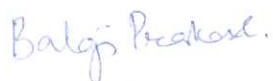
Gaurav Goswami  
Assistant Professor, Division of Mathematical and  
Physical Sciences, School of Arts & Sciences,  
Ahmedabad University.  
External Examiner

## Approved By:



20/5/24

Raghavan Rangarajan  
Dean, School of Arts & Sciences,  
Ahmedabad University.



20.05.2024

Balaji Prakash  
Associate Dean, School of Arts & Sciences,  
Ahmedabad University.

# Acknowledgement

I would like to thank my advisor, Professor Samyaday Choudhury, for teaching me the fundamentals of astronomy and astrophysics in a thorough manner. I extend my sincere thanks for allowing me to work on this project. Through this project, his pragmatic approach and voracity for science have contributed to my understanding of physics. Over the last few months, his encouragement and mentorship have significantly improved my academic learning.

Secondly, I thank Dr. Annalisa Calamida from the Space Telescope Science Institute for collaborating on this project and sharing constructive feedback and extensive knowledge about the subject, which has seriously contributed to the nature of this work.

I thank Professor Gaurav Goswami for assessing this work and providing valuable insights and comments. His method of teaching physics has been pivotal in my understanding of nature.

I would also like to thank Professor Jitesh Bhatt (Physical Research Laboratory), various members of Professor Annapurni Subramaniam's (Indian Institute of Astrophysics) research group, various members of the Astronomy and Astrophysics Group (at Ahmedabad University) for sharing their crucial insights and scientific knowledge about the project.

I am grateful to Anshuman, Devansh, Yashwardhan, Abraham, Prerna, Archisha, and Prithviraj for the conversations that have shaped me through this degree.

I am indebted to my friends Dev, Pooja, Akhil, Pujitha, and Kanak for supporting me.

Lastly, I thank my family for providing me with unfailing support.

# Abstract

NGC2808 is a very intriguing and unusual galactic globular cluster that purportedly has undergone more than one episode of star formation, hosting distinct stellar sub-populations. In this study, the white dwarf (WD) stars in NGC 2808 have been analyzed using near-ultraviolet and optical data (F275W, F336W, and F438W) from the Hubble Space Telescope. The identification and studies of various types of WDs - e.g. ones with a core composed of carbon and oxygen (CO-core) and ones with a core composition of helium (He-core) are crucial for understanding their formation scenario, which remains elusive and could depend on factors like – binarity, cluster mass, etc. In this study, the color-magnitude diagrams of NGC2808 using various combinations of filters and theoretical models of WD cooling sequences were used to identify WDs. Star counts of the main sequence turnoff stars and red giant branch stars were performed, and artificial star test results corrected their completeness. These were then compared with the WDs to constrain the number of WDs in the cluster. This is needed to understand the formation scenario of He-core WDs since such stars supposedly form through binary interactions for the Universe's  $\sim 13$  billion-year history.

**Keywords:** *White Dwarfs, Globular Cluster: NGC2808, Star Counts, He-core WDs*

# Contents

<b>Acknowledgement</b>	iv
<b>Abstract</b>	v
<b>List of Figures</b>	xi
<b>List of Tables</b>	xii
<b>1 Introduction</b>	1
<b>2 Stellar Evolution</b>	8
2.1 Introduction	8
2.2 Evolution of Low-mass Stars	9
2.3 WD Stars	15
<b>3 Photometric Data of NGC2808</b>	25
3.1 Introduction	25
3.2 Data Cleaning	35
3.3 CMD Features of NGC2808	38
<b>4 Methodology and Analysis</b>	45
4.1 Introduction	45
4.2 Star Counts and Crossing Times	48
4.3 Ratios	64
<b>5 Results and Discussions</b>	67
5.1 Ratios	67
5.2 Bimodality in the White Dwarf Sequence	70
5.3 Conclusion	74
<b>A Sommerfeld's Free Electron Approximation</b>	
<b>Bibliography</b>	

# List of Figures

1.1	Figure shows the evolution of a $1 M_{\odot}$ star on a HRD. It begins from the Zero-Age Main Sequence (ZAMS) to the WD phase of a star. Figure adapted from Carroll & Ostlie (1996, pg. 458)	2
1.2	This image was taken by the Hubble Space Telescope and shows the bright star, Sirius A, and its tiny stellar companion, Sirius B. This binary system is 8.6 ly away from the Earth. (Credit: ESA/Hubble)	4
1.3	Image of the globular cluster NGC 2808 combined using separate exposures made by the Advanced Camera Survey and Wide Field Camera 3 onboard the Hubble Space Telescope. (Credit: NASA/ESA)	6
2.1	Henry Norris Russell's first diagram, whose y-axis has spectral types and x-axis has absolute magnitudes. A star named 40 Eridani B appears in the diagram at (A,+11) point. Figure adapted from Russell (1914).	15
2.2	This plot shows the mass-radius relation for relativistic (solid curve) and non-relativistic (dashed curve) momentum. Figure adapted from Chandrasekhar (1984).	21
2.3	Left plot shows the luminosity vs. surface temperature relation (blue curve) whereas the right plot shows the luminosity vs. cooling age (pink-curve) of a CO-core and H-envelope $0.54 M_{\odot}$ WD Model downloaded from the BaSTI dataset. As is evident, with decreasing luminosity, the temperature decreases, and the cooling time increases.	23
2.4	An artist's impression of a binary system comprising of a red giant star and a WD star. The WD accretes matter from the RGB leaving the core of the RGB exposed. This is the He-core WD and one of the mechanisms through which they form. This image is sourced from here.	24
3.1	Image of the Hubble Space Telescope. Source: NASA.	26
3.2	Figure shows all possible CMDs plotted using 5 filters. The color and magnitude are mentioned at each plot's top. Each plot has 343134 points, i.e., these are plotted using the raw data.	29
3.3	The left-hand-side plots show the error in magnitude (d-param) vs. magnitude for each object in the dataset, whereas the right-hand-side plots show the histogram of error in magnitude.	31
3.4	The left-hand-side plots show the q-param vs. magnitude for each object, whereas the right-hand-side plots show the histogram of q-param values.	32

3.5	The left-hand-side plots show the sharpness parameter (s-param) vs. magnitude for each object, whereas the right-hand-side plots show the histogram of sharpness parameter values. . . . .	33
3.6	Figure shows the two CMDs which will be used for further analysis. The left CMD is a F275W - F336W vs. F275W, whereas the right CMD is a F275W - F438W vs. F275W. Same as figure 3.2, each plot has 343134 points. . . . .	34
3.7	Top-left plot is the F275W - F336W vs. F275W CMD with no cuts. Other plots are of the same color and magnitude but with varying $P_\mu$ cut as 60% (top-right), 80% (bottom-left), and 95% (bottom right). The number of objects retained in each case is noted in the respective plots. . . . .	36
3.8	Same as figure 3.7 but with color F275W - F438W. . . . .	37
3.9	Figure shows a F475W - F814W vs. F814W CMD shows the split in the MS in three. (Adapted from Piotto et al. (2007, fig. 2)). . . . .	39
3.10	Figure shows an F275W - F336W vs. F336W CMD highlighting the blue straggler stars (pink colored) in NGC2808. (Adapted from Prabhu et al. (2021, fig. 3)). . . . .	40
3.11	Figure shows a F275W - F438W vs. F336W CMD highlighting the UV-bright stars (purple coloured) in NGC2808 (Adapted from Prabhu et al. (2021, fig. 3)). . . . .	41
3.12	Figure shows a plot with a “special” plotted on both the y-axis and highlights the three gaps in the HB of NGC2808. Additionally, various varieties of HB stars, such as red horizontal branch (RHB) stars (in red), blue horizontal branch (BHB) stars (in blue), extreme horizontal branch (EHB) stars (in green), B-gap objects (in cyan) and blue hook (BHk) stars (in yellow). (Adapted from Prabhu et al. (2021, fig. 3)). . . . .	42
3.13	Figure shows a F275W - F438W vs. F275W CMD showing the spilted WD sequence in $\omega$ Centauri. (Adapted from Bellini et al. (2013, fig. 3)). . . . .	43
3.14	Figure shows an RA vs DEC plot of objects retained after a 60% cut on $P_\mu$ . . . . .	44
4.1	The teal-colored triangles are the completeness parameter for the MS-RGB ( $\Phi_1$ ) artificial star test corresponding to the $m_{F275W}$ . A function ( $\Phi_{MS-RGB}$ ) was fit to this and is highlighted as the pink curve. A red dashed-dot vertical line shows the magnitude of the completeness at 0.75, i.e., 75%. . . . .	47
4.2	The blue-colored triangles are the completeness parameter ( $\Phi_2$ ) for the WD artificial star test corresponding to the $m_{F275W}$ . A function ( $\Phi_{WD}$ ) was fit to this and is highlighted as the pink curve. A red dashed-dot vertical line shows the magnitude of the completeness at 0.5, i.e., 50%. . . . .	47

- 4.3 Left plot are the 336CMD and 438CMD from top to bottom respectively, with a  $P_\mu \geq 60\%$  cut. The blue curve is a 10.9 Gyr isochrone. The objects in pink lie between  $0.82 \pm 0.0030 M_\odot$ . The lime green region has been highlighted since this is the varying mass region, i.e., mass corresponding to these points lies between  $0.82 \pm 0.0030 M_\odot$ . The golden-colored star is the theoretical MSTO point on the CMD, better visible in the figure 4.4. The right plots are color histograms of the pink objects in the respective CMDs. All objects in  $2\sigma$  of the highest point on the histogram were considered MSTO stars. . . . . 50
- 4.4 Plotted are two CMDs, cleaned with a  $P_\mu \geq 60\%$  cut. In the left panel is the 336CMD. The blue and cyan lines represent the 10.9 Gyr isochrone and evolutionary track of mass  $0.82 M_\odot$ , respectively. The lime-green line on the CMD is the part on the isochrone where the mass is  $0.82 \pm 0.0030 M_\odot$ . A gold-colored star (better visible in the inset plot) is the theoretical MSTO derived from the isochrone. The light-pink (1086 and 1100 star counts in the 336CMD and 438CMD, respectively) and coral-brown (1129 and 1141 star counts in the 336CMD and 438CMD, respectively) triangles are the *upper bin* and *lower bin* stars, respectively. These have been zoomed into and are presented in the inset plot. Overplotted on the evolutionary track (red-colored) are three teal-colored triangles denoting the corresponding magnitude limits on the evolutionary track. The right panel has the 438CMD with the same analysis. For completeness corrected star counts and corresponding lifetimes refer to the 0.0030 rows of table 4.1 for this plot. 52
- 4.5 Both CMDs (left plots) have been cleaned with a  $P_\mu \geq 60\%$  cut. They are the 336CMD and 438CMD from top to bottom respectively. The blue curve is a 10.9 Gyr isochrone. The curve is thicker from the 490<sup>th</sup> to the 1290<sup>th</sup> point (see text for detail). The purple vertical dashed line goes through the theoretical foot of the RGB (see text for detail). The right plots are color histograms of objects from 18 to 23 mag in the respective CMDs. All objects between 19.4 and 21.4 color values on the histogram were considered RGB stars since a “dip” is seen at these values. . . . . 54
- 4.6 Plotted are two CMDs, cleaned with a  $P_\mu \geq 60\%$  cut. In the left panel is the 336CMD. The blue curve is the same as in figure 4.5. The purple dashed lines were drawn to select RGB stars highlighted in pink (4895 objects in 336CMD and 5027 objects in 438CMD; note that these are not completeness corrected counts.). The green-colored hexagon is the point corresponding to which time was calculated. The right panel has the 438CMD with the same analysis. not completeness corrected. For star counts and corresponding lifetimes, refer to the 60% column of table 4.2. . . . . 55

4.7	The plots are the luminosity functions of RGBs as selected by the method elaborated above. The left plot corresponds to the 336CMD, whereas the right one corresponds to the 438CMD. The dark pink-colored bars are without completeness accountability (for 336CMD, the cumulative star count is 4895; for 438CMD, the cumulative star count is 5027). In contrast, the light pink bars are completeness accounted counts (for 336CMD, the cumulative star count is 6234; for 438CMD, the cumulative star count is 6402). The completeness corrected counts are given in table 4.2. . . . .	56
4.8	The CMDs were cleaned as discussed in the text above. The left plot is the 336CMD, where all stars in triangles are WDs. Teal-colored triangles are WDs brighter than 21 mag, whereas pink triangles are fainter than that. This distinction was made to explain completeness counts. The right plot is 438CMD with the understanding. . . . .	58
4.9	Plots are WD luminosity functions of 336CMD and 438CMD from left to right. The dark pink is the observed data number, whereas the light pink is the corrected completeness (see text for counts). . . . .	59
4.10	To understand the different parameters of each model which the legend contains first the core of the WD model is written (say CO-core), then followed by a “/” is the envelope type of the model (say He) followed by a “-” and metallicity of the model (say 0.04), followed by another model parameter, called the electron conduction opacity. “20” (Blouin et al. (2020)) or “7” (Cassisi et al. (2007)) are the choices for the same, which refer to the year of the paper from which they were adopted to generate these plots by BaSTI (see (Pietrinferni et al. 2021) and (Salaris et al. 2022)). Then, in brackets is the mass of the WD model. For figure 4.11, the corresponding crossing is also given following the mass. These 20 models are given model numbers, which will be used to find ratios in the next section. . . . .	60
4.11	336CMD and 438CMD with those models for which crossing time could be found for both CMDs. Pink and teal-colored triangles are the same stars as in previous plots. . . . .	61
4.12	The left plots show 336CMD and 438CMD from top to bottom respectively. The blue cutout is the manual selection made to select the HB stars. On the right are the pink stars from 336CMD and 438CMD plotted to check if they belong to the horizontal branch. . . . .	63
5.1	Values from the table 4.6 have been plotted. On the y-axis are the various $N_{\text{Obsv}}$ (all colors circles except purple circles) and $\tau_{\text{Theo}}$ (purple circles) values, whereas on the x-axis are the ratio number from table 4.6. . . . .	69

5.2	Values from the tables 4.7 and 4.8 have been plotted. “Observational” and “theoretical” in the legend mean $N_{\text{Obsv}}$ (-1 and 0) and $\tau_{\text{Theo}}$ (1 to 20) ratios respectively. In table 4.8, model number starts from 1 till 20, but in the above plot, the x-axis (model number) starts from -1; -1 and 0 are the $N_{\text{Obsv}}$ values and do not indicate any model number whereas 1 to 20 are the $\tau_{\text{Theo}}$ values from the table 4.8. The last model number corresponds to the He-core model and the others to the CO-core with different parameters. . . . .	69
5.3	Values from the tables 4.9 and 4.10 have been plotted. -1 and 0 on the x-axis correspond to the same as in figure 5.2. Here also the last model number corresponds to the He-core model. Triangles are the various $\tau_{\text{Theo}}$ ratios, whereas the circles and stars are the various $N_{\text{Obsv}}$ values. . . . .	70
5.4	Straightened WD Sequence. The left plot corresponds to the 336CMD, whereas the right plot corresponds to the 438CMD. . . . .	71
5.5	The 336CMD straightened WD sequence was divided into three halves and straightened color histogram for each case was plotted. . . . .	72
5.6	The 438CMD straightened WD sequence was divided into three halves and straightened color histogram for each case was plotted. . . . .	73

# List of Tables

2.1	This table showcases the characteristics and effective temperatures ( $T_e$ in units of 1000 K) of the spectrum of different types of WDs. Values used in this table have been taken from Carroll & Ostlie (1996, pg. 559) and Althaus et al. (2010, pg. 9). . . . .	17
3.1	Table shows the positional, photometric, and structural parameters of NGC2808. The subscripted parameters means: <sup>a</sup> Total visual magnitude, <sup>b</sup> Core radius, <sup>c</sup> Half-mass radius, <sup>d</sup> Tidal radius, <sup>e</sup> Log of relaxation time, <sup>f</sup> Reddening, <sup>g</sup> True distance modulus. . . . .	38
4.1	Counts and crossing times of MSTO stars for various varying mass values in the 336CMD and 438CMD with probability membership cut of 60% & 95% have been presented. Note that these star counts are accounted for completeness. . . . .	51
4.2	Counts and crossing times of RGB stars in the 336CMD and 438CMD with probability membership cut of 60% & 95% have been presented. Note that these star counts are accounted for completeness. . . . .	53
4.3	Summary of the d-param and s-param values for the 336CMD and 438CMD. . . . .	57
4.4	Crossing Times of Various WD Cooling Models. ZPoor refers to metallicity values $< 0.01$ . '*' parameters are to be taken from literature . . .	62
4.5	Star counts of HB stars in the 336CMD and 438CMD with probability membership cut of 60% & 95% have been presented. Note that these star counts are not completeness accounted for since the AST for these stars wasn't performed. . . . .	63
4.6	4 sets of $N_{\text{Obsv}}$ and the corresponding $\tau_{\text{Theo}}$ values have been presented. Note that all these ratios are $\frac{\text{MSTO}}{\text{RGB}}$ . . . . .	64
4.7	$\frac{\text{WD}}{\text{RGB}}$ $N_{\text{Obsv}}$ (observed) values . . . . .	65
4.8	$\frac{\text{WD}}{\text{RGB}}$ $\tau_{\text{Theo}}$ (theoretical) values . . . . .	65
4.9	$\frac{\text{WD}}{\text{MSTO}}$ $N_{\text{Obsv}}$ values . . . . .	66
4.10	$\frac{\text{WD}}{\text{MSTO}}$ $\tau_{\text{Theo}}$ values . . . . .	66

*Dedicated to my sister,  
Aakriti*

# Chapter 1

## Introduction

*Stars which end as WDs (as our Sun probably will) can rest in peace.*

- Shu (1982, pg. 129)

The evolution of a star, or simply stellar evolution, describes how a star changes over time. It is primarily studied via computer simulations and is quite complicated in its detail. The understanding of stellar evolution has seen significant development since the 1960s, thanks to better computational power, observational techniques, and a better grasp of physical processes inside the star. However, the stars in stages of evolution, such as the protostars (developing stage of a star) and WDs (dead stars), are far from understood.

The evolution is predominantly dependent on the mass of the star at the time when it starts burning hydrogen in its core. This mass is called the initial mass of the star. The initial mass of a star decides the rate of evolution, the rate of nuclear fuel burning, and its ultimate fate. Stars of the initial mass of higher end (i.e.,  $> 8M_{\odot}$ <sup>1</sup>) end their lives as black hole stars or neutron stars, whereas less massive ones end their lives as white dwarf (WD) stars. However, this classification depends upon other parameters, such as metallicity and binarity. The evolution of stars is best understood and explained via a special kind of diagram called the Hertzsprung–Russell Diagram

---

<sup>1</sup> $1 M_{\odot} = 1.99 \times 10^{30}$  kg and  $1 L_{\odot} = 3.828 \times 10^{26}$  W

(HRD). It is a plot of the surface temperature of a star (also called effective temperature,  $T_e$ ) versus luminosity per solar luminosity ( $\frac{L}{L_\odot}$ ) on the natural log scale. Figure 1.1 shows the evolution of a  $1 M_\odot$  star on an HRD. For an observer, the HRD is transformed into the observational plane called a Color-Magnitude Diagram (CMD), plotting the two quantities of a star. On a CMD, “color” corresponds to  $T_e$  and is plotted on the x-axis, whereas magnitude corresponds to luminosity and is plotted on the inverted y-axis.

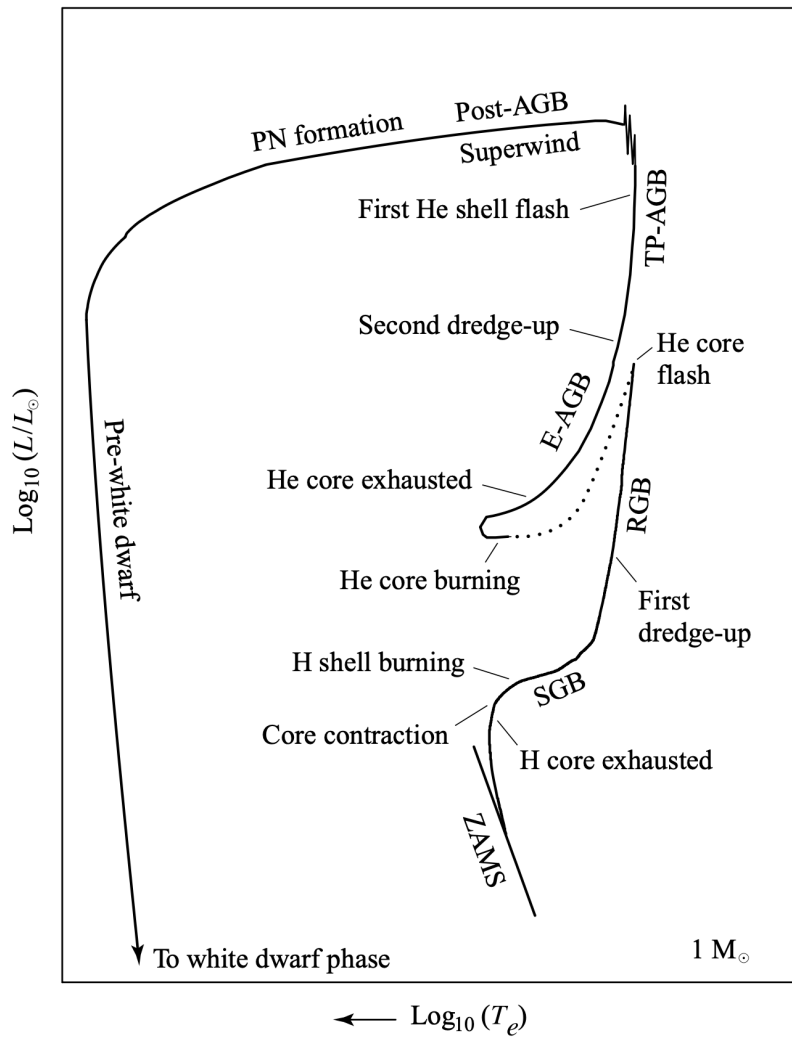


Figure 1.1: Figure shows the evolution of a  $1 M_\odot$  star on a HRD. It begins from the Zero-Age Main Sequence (ZAMS) to the WD phase of a star. Figure adapted from [Carroll & Ostlie \(1996, pg. 458\)](#)

Tersely, the evolution of a star of mass  $1 M_\odot$  is described as follows. It first

appears on the HRD on the main sequence (MS), where it burns hydrogen at nuclear timescale ( $\tau_{\text{nuc}} \approx 10^{10}$  years). As the hydrogen is depleted in the core of the star (this is marked at the main sequence turnoff point or MSTO), its core starts to contract, leading to hydrogen-shell burning. The hydrogen shell burns around the He core on the sub-giant branch (SGB), and the star ascends on the red giant branch (RGB) and loses mass from the outer layers. The temperature of the core continues to rise during this phase. At the tip of the RGB, the core has temperatures high enough to fuse He and the star starts to burn He. The star then moves onto the horizontal branch (HB) where it evolves on a much shorter timescale, burning He in the core. Next, it ascends the asymptotic giant branch (AGB) phase of evolution, where it again loses mass from the outer layers and finally becomes a WD. Chapter 2 of this thesis describes each of these phases in detail. This study focuses on the analysis of WDs.

WDs are extremely faint celestial relics of stars whose initial mass  $< 8M_{\odot}$ <sup>2</sup> with a typical radius  $\sim 10^4$  km (Choudhuri 2010, pg. 137). They are exposed cores of stars that fused hydrogen and/or He in their past. 95~98 % of the stars in the Galaxy will likely end their lives as WDs (Salaris & Cassisi 2005; Winget & Kepler 2008). A detailed discussion on WDs follows in section 2.3. Figure 1.2 is an image of a binary system containing a WD (tiny bottom left dot).

For the following reasons, WDs are interesting and important objects to study.

- Firstly, since these stars are one of the densest objects in the universe with densities of the order of  $\sim 10^9$  kg/m<sup>3</sup> (Carroll & Ostlie 1996, pg. 473) they qualify as excellent astrophysical laboratories to test physical processes occurring under extreme conditions.
- Secondly, their study holds abundant information about their progenitor stars' physical properties, binarity and evolution mechanisms.
- Lastly, though, they are born as extremely hot objects (surface temperature

---

<sup>2</sup>with a potential extension to  $11 M_{\odot}$  (Woosley & Heger 2015; C  rsico et al. 2019)

ranges from 5000~80000 K ([Carroll & Ostlie 1996](#), pg. 559)), they neither produce nuclear energy nor thermal energy during their evolution and hence their evolution is often described as a pure cooling process, i.e., as they age, they become dimmer and cooler (see figure 2.3). This establishes a tight relation between WD luminosity and their ages. They are exceptional cosmic chronometers to constrain the ages of the Galaxy and star clusters (more details in [2.3.3](#)).

The models that predict this cooling process are known as WD Cooling Models (WD evolutionary models). Because these are fainter and smaller objects, these cooling models are yet to be tested and hold immense opportunity to be improved.

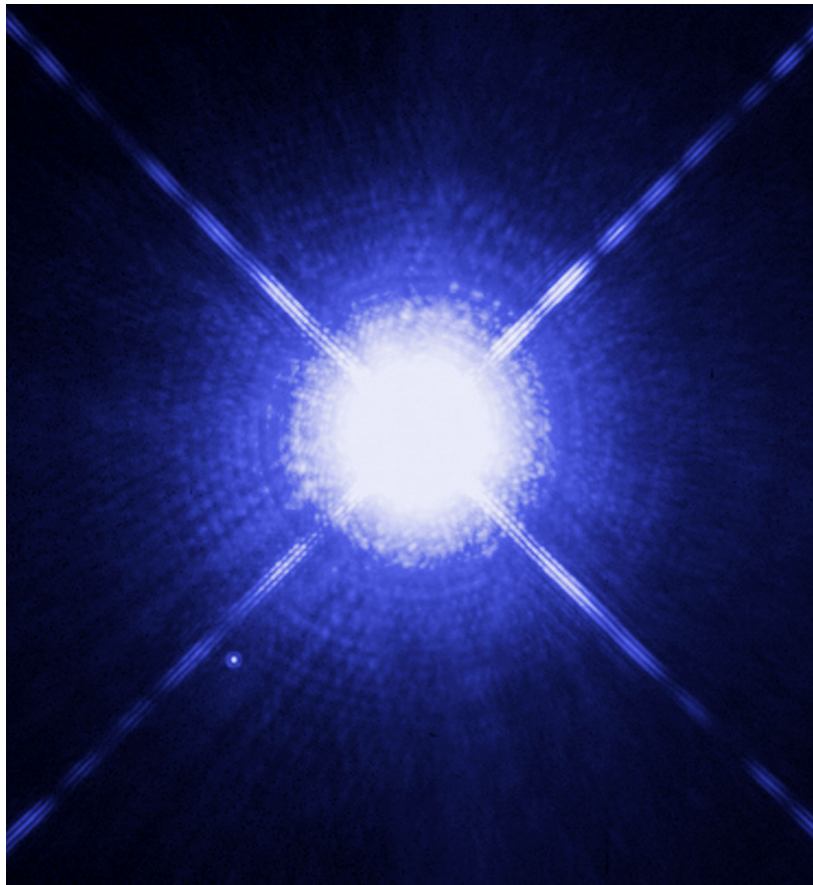


Figure 1.2: This image was taken by the Hubble Space Telescope and shows the bright star, Sirius A, and its tiny stellar companion, Sirius B. This binary system is 8.6 ly away from the Earth. (Credit: [ESA/Hubble](#))

WDs negotiate a balance between the electron degeneracy pressure and self-gravity. Due to this, the maximum mass of a WD can never exceed  $1.4 M_{\odot}$ . This was first

discovered by the Indian physicist Subrahmanyan Chandrasekhar, for which he was awarded the Nobel Prize in Physics in 1983, alongside William Alfred Fowler. This mass limit is now celebrated as the *Chandrasekhar Mass Limit* (section 2.3.2).

These degenerate stars come in two varieties based on their core composition - WDs with carbon (C) and oxygen (O) in their core are called the carbon-oxygen-core WDs (CO-core WDs), and WDs with He in their core, called the He-core WDs (He-core WDs). They are further subdivided based on their atmosphere composition,

- H envelope (known as the DA-type),
- He envelope (DB-type).

WDs are present in both the field and the star clusters. This study considers WDs in globular clusters (a type of star cluster) for reasons elaborated upon shortly. For decades, globular clusters (GCs) for studying sub-stellar populations have been an exquisite choice for astronomers. They are spherical, gravitationally tightly bound systems containing population I  $10^5$  to  $10^6$  low-mass stars, found in the halo of spiral galaxies, like Milky Way Galaxy. They contain a range of stars, from the familiar stars, inside whose core hydrogen or He is being fused, to exotic stars, such as blue stragglers (BSS) and cataclysmic variables (CVs), including binary star systems. Among these stars is also the one of interest in this study —WDs. GCs provide a consistent sample to examine, i.e., well-constrained reddening, age, chemical composition, and distance modulus. For this study, the globular cluster NGC2808 is under scrutiny (figure 1.3 is an image of the cluster, which is a part of the Carina constellation). The primary objective of this study is to constrain the number of WDs and test WD evolutionary models in NGC2808. The forthcoming chapters (chapter 2 and 3) will provide additional motivation for this investigation as pertinent topics are examined and discussed.

NGC2808, which James Dunlop discovered in the 1820s, is an unusual globular cluster. It was one of the first GCs where main sequence splits were observed (Piotto et al. 2007). It is filled with exotic stars, such as BSS, blue hook (BHk) stars, ex-

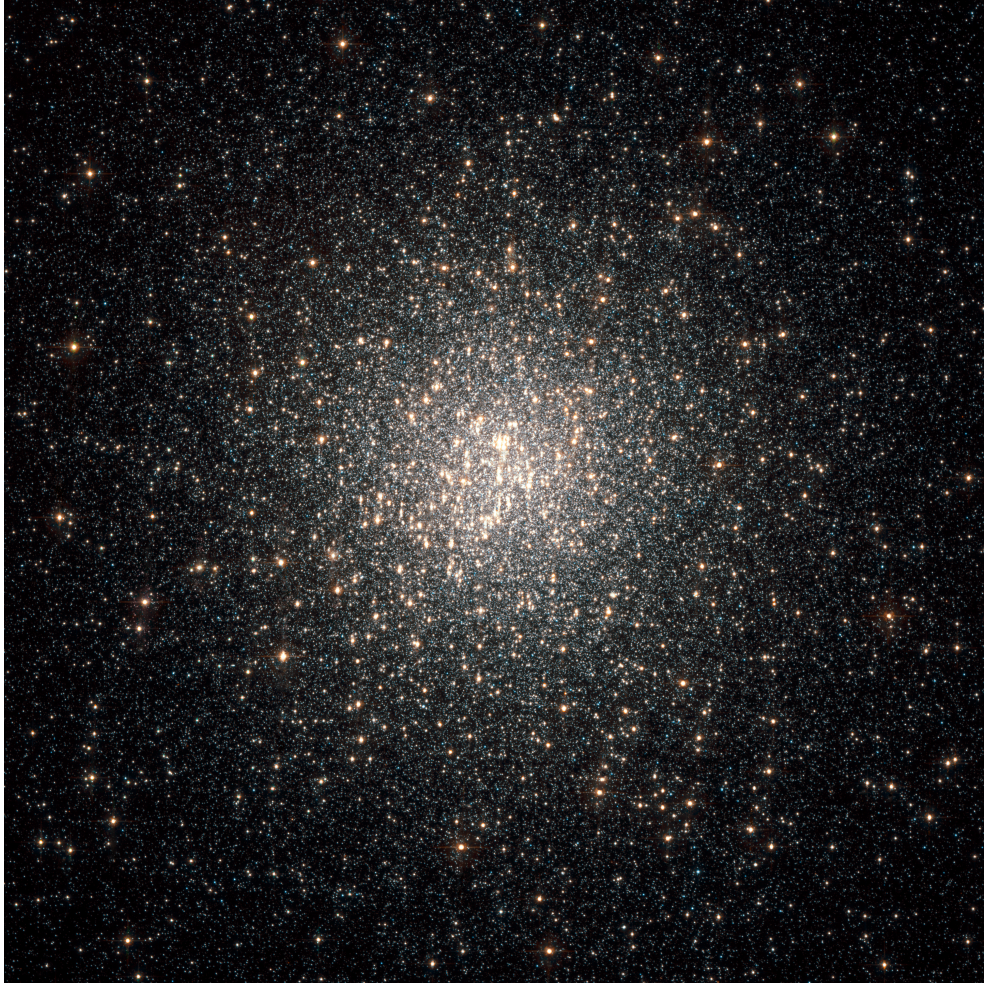


Figure 1.3: Image of the globular cluster NGC 2808 combined using separate exposures made by the Advanced Camera Survey and Wide Field Camera 3 onboard the Hubble Space Telescope. (Credit: [NASA/ESA](#))

tended horizontal branch (EHB) stars, and other Ultraviolet-bright (UV-bright) stars. The features of this cluster will be discussed in detail in section 3.3. It is crucial to investigate WDs in this particular GC; they are the least studied sub-stellar population since they are faint. Now, with more high-precision photometry more could be said about this cluster. Further, such an investigation could enhance the understanding of the formation scenario of this GC, specifically in this case because it contains multiple stellar populations (more on this in section 3.1).

It is preposterous to observe WDs in a GC without special telescopes such as the Hubble Space Telescope (HST), which probes the universe into deeper magnitudes

since these are small and faint objects. For this reason, the precise photometric data (or catalog) of NGC2808 used for this study has been taken from the ‘Hubble Space Telescope Ultraviolet Globular Cluster Survey,’ popularly known as the HUGS Survey (Nardiello et al. 2018). The same was downloaded from the MAST Archive<sup>3</sup> which is available as a High Level Science Product<sup>4</sup> (HLSP). Several theoretical models from the BaSTI (Salaris et al. 2022; Pietrinferni et al. 2021) dataset such as the MS-RGB evolutionary models, isochrones, WD cooling models for various masses were used to analyze stars in different evolutionary phases. This will be discussed in detail in section 4.1. All the theoretical models that were fitted to the CMD were done after correcting for reddening, using Cardelli’s Reddening Law, Cardelli et al. (1989), and distance.

The flow of this document is as follows: chapter 2 gives a basic description of how a low-mass star evolves, followed by chapter 3, which describes the data that has been used for the study and elaborates on the peculiar features in the CMD of NGC2808. Next, chapter 4 discusses the methodology of this study and explains in-depth how the WD’s data analysis has been to achieve the study’s goals. Chapter 5 presents the results and discussions of this study.

---

<sup>3</sup><https://archive.stsci.edu/prepds/hugs/>

<sup>4</sup><https://mast.stsci.edu/hlsp/#/>

# Chapter 2

## Stellar Evolution

Everything passes away - suffering, pain, blood, hunger, pestilence. The sword will pass away too, but the stars will remain when the shadows of our presence and our deeds have vanished from the Earth. There is no man who does not know that. Why, then, will we not turn our eyes toward the stars? Why?

---

*Mikhail Bulgakov*

### 2.1 Introduction

As stated in chapter 1, the most important factor determining the evolution of a star is its initial mass. The scope of this study pertains to the evolution of stars which evolve to become WDs from the stage where they start to burn H in their core until they become WDs, and hence, this section only discusses the evolution of low-mass stars ( $< 4M_{\odot}$ ). To begin with, a concise description of the birth of a star cluster is expanded upon. Following this, the evolution of low-mass stars is discussed in detail. In the latter half of the chapter, the discussion on WDs from chapter 1 continues. The ideas of structure, evolution, and classifications of these stellar relics are canvases.

Stars are born from a dramatic collapse of a cloud of molecular H, gas and dust. A dust cloud becomes gravitationally unstable and collapses. Inhomogeneities in the density of the dust cloud cause a series of cascading local collapses and “fragments” the collapsed dust cloud in the so-called fragmentation process. The center of a fragment keeps contracting until the temperature is hot enough to generate energy to counter gravity. This contraction is followed on the free-fall timescale ( $\tau_{\text{ff}} \approx 1000$  seconds). Once it can generate energy to counter gravity, the fragment’s center is nearly in hydrostatic equilibrium, and the central region of the fragment is called a protostar. The protostar evolves to be a real star, i.e., it becomes capable of converting H to He. For a  $1 M_{\odot}$  star, it takes  $\approx 39$  Myrs to fuse H in its core ([Carroll & Ostlie 1996](#), pg. 427). Since the energy source of the star is the energy coming from core contraction but not the nuclear energy, this evolution is typically on the Kelvin-Helmholtz timescale ( $\tau_{\text{KH}}$ ), which is of the order of  $10^7$  years. The above description of the birth of stars has been adapted from ([Carroll & Ostlie 1996](#), pg. 412 - 422). The discussion from here on is restricted to stars with low mass.

## 2.2 Evolution of Low-mass Stars

### 2.2.1 H-burning and Post-H Burning Phase

Once a protostar’s dominant and stable energy source is the energy from the conversion of H into He it is considered to be born. It emerges on the CMD on the supposed zero age main sequence (ZAMS) and is now called MS star. On a CMD of a globular cluster, the MS is one of the prominent sequences. It is not a thin line but has a width due to many factors, including observational errors and stars with different chemical compositions. The upper MS stars are massive stars burning nuclear fuel at higher temperatures, converting H to He via the Carbon-Oxygen-Nitrogen (CNO) cycle. On the other hand, the low-mass stars are located at the lower end of the MS and convert H to He via the pp chain mechanism. For stars with mass  $< 1.2 M_{\odot}$ , the core of the star is radiative, while for stars more than  $> 1.2 M_{\odot}$  the core is convective since

radiation is insufficient to transport all energy ([Carroll & Ostlie 1996](#), pg. 447). The following discussion entails only the evolution of a star on the MS of mass  $< 1.2M_{\odot}$ .

While on the MS, a star evolves due to the increased molecular weight of the star's core; this results from the conversion of H to He. According to the ideal gas law, to counter this increase in molecular weight, the core's density and/or temperature must increase to maintain the hydrostatic equilibrium. Hence, the core of the star must be compressed. The density of the core increases, which leads to the temperature of the gas being increased, and consequently, there is more region of nuclear fuel burning. However, this increase in temperature and density compensates for more than the decrease in the mass fraction of H, due to which the star's luminosity increases together with its radius and  $T_e$ .

On a CMD of a globular cluster, one finds that the MS is highly populated. This is because the timescale prominent in this sequence is the nuclear timescale ( $\tau_{\text{Nuc}}$ ), which is of the order of  $10^{10}$  years almost three orders of magnitude larger than the  $\tau_{\text{KH}}$  which is dominant in the protostellar evolution. Given this, it takes more time for a star to evolve from this phase; hence, more stars are found in the MS.

The H eventually gets completely depleted in the core of the star. For a  $1M_{\odot}$ , this is reached after 9.8 Gyrs ([Carroll & Ostlie 1996](#), pg. 450). On the HRD (see figure [1.1](#)), this is marked as the main-sequence turnoff (MSTO). The energy generation in the core via the proton-proton (pp) chain stops. This marks the end of MS, and the core cannot support itself against gravity, so it starts to contract (in figure [1.1](#), this is highlighted as *core contraction*). Further explanation of stellar evolution is limited to a star of mass  $1M_{\odot}$  since the evolution off the MS strongly depends on total stellar mass ([Salaris & Cassisi 2005](#), pg. 141).

The contraction heats the star's core, and consequently, the temperature around the predominant He core rises, and a thick H-burning shell starts to fuse H. The H is fused into He via the CNO cycle in this shell. H-shell burning marks the start of the sub-giant branch (SGB) phase (in figure [1.1](#) it is marked as *H shell burning*) of evolution and evolves on the  $\tau_{\text{KH}}$ . Additionally, the core contraction leads to the

expansion of the envelope and a decrease in effective temperature following a drastic increase in opacity, and the star “swells”. ([Salaris & Cassisi 2005](#), pg. 142). The decrease in surface temperature is yet to be understood physically; nevertheless, all theoretical models seem to present this as a fact ([Salaris et al. 2002](#)). From the start to the end of the SGB, the H-burning shell keeps getting thinner<sup>1</sup> and the He content in the core keeps increasing. The shell reduces from about  $0.2M_{\odot}$  to  $0.001M_{\odot}$  ([Salaris & Cassisi 2005](#), pg. 143). At the same time, the luminosity during the SGB remains almost constant ([Salaris & Cassisi 2005](#), pg. 142). Alongside this, the temperatures on the star’s surface cool down enough since  $H^-$  is produced, which results in a convection zone being developed near the surface ([Carroll & Ostlie 1996](#), pg. 460). At the end of the SGB, the He core is degenerate but cannot support the inward gravity. The core contraction now stops, but the temperature of the core continues to rise when He can fuse. This point on the HRD (see figure 1.1) is called the foot of the red-giant branch (RGB). As stated in [De Becker \(2020\)](#), at the start of the red-giant phase of the star, it has four distinct layers: a degenerate, isothermal He-core surrounded by a H-burning shell. At the surface is a convective envelope, and between this and the H-burning shell is a radiative zone.

The evolution of a star on the RGB occurs as the convective zone extends deep into the interiors of the star. This is due to Kramers’ Law, which informs us that a decrease in temperature implies an increase in opacity, which in turn makes the convective envelope go deeper into the star. Consequently, the convective zone extends deep enough towards the center of the star where the chemical composition has been modified due to nuclear reactions; the “processed” material gets mixed with the material above the convective zone. Essentially, this results in exchanges of chemical abundances; for example, Li, produced outside the core, is now brought to the core. Similarly,  $^3_2He$ , which is produced in the core, is now brought to the surface. This material exchange phase is called the first dredge-up phase ([Carroll & Ostlie 1996](#), pg.

---

<sup>1</sup>since the H-shell burning occurs via CNO cycle, its temperature sensitivity shrinks the shell as H is converted to He on the inner region of the shell and the temperature cools in the outer region of the shell ([Salaris & Cassisi 2005](#), pg. 143)

461). Simultaneously, the H-burning shell keeps getting even thinner (since it burns) until the tip of the RGB is reached (where it is about  $0.0001M_{\odot}$  ([Salaris & Cassisi 2005](#), pg. 144)).

An important relation between the surface luminosity and mass of the electron degenerate core is noticed during the RGB evolution of low-mass stars, which tells us that increased He core mass results in increased surface luminosity and hence the star's surface luminosity, i.e., it ascends the RGB (See [Salaris & Cassisi \(2005, pg. 144\)](#) and [Kippenhahn et al. \(2012, ch. 33\)](#)). However, the increase in luminosity is disrupted when the H-burning shell crosses the chemical discontinuity left over by the (convective) envelope following the first dredge-up phase, which causes the star to pass the same luminosity value thrice on the CMD. This is the so-called RGB bump (also called Thomas Peak), as is very evident on CMDs plotted with high-quality photometry ([Kippenhahn et al. 2012, pg. 397 - 400](#)).

Mass loss during the RGB phase of a star is common due to the star's reduced ability to hold on to the material in the outer layers. The pressure gradient right above the He core is several orders larger than that of the pressure gradient above the H-burning shell ( See [Salaris & Cassisi \(2005, pg. 145\)](#) [Choudhuri \(2010, pg. 112 - 113\)](#)). Although, an exact theory of what mass is lost during the RGB awaits an answer([Kippenhahn et al. 2012, pg. 408](#)). Furthermore, an interesting event transpires at the end of the RGB (the so-called tip of the RGB), associated with the core of the star. During the entirety of the RGB evolution, the central density, He-core mass, degree of electron degeneracy, and core temperature increase. At the tip of the RGB, when the temperature reaches  $\approx 10^8$  K, He-burning is ignited.

**A note on stars of ZAMS mass between 0.1 - 0.5  $M_{\odot}$ :** In a classic paper by [Iben & Webbink \(1989\)](#), the authors showed that stars of ZAMS mass in the range 0.1 - 0.5  $M_{\odot}$  evolve differently. These stars do not undergo He flashes at the tip of the RGB and cool down. However, the universe is too young for stars of this mass even to turn off from the MS. The progeny of these stars are He-core WDs. However, several accounts of He-core WDs are found in the universe (see [Strickler et al. \(2009\)](#))

and references therein). So, how does one reconcile their existence of these exotic stars? This is done by explaining their presence via other mechanisms and has been discussed in detail in section [2.3.4](#).

### 2.2.2 He-burning and Post-He Burning Phase

Refocusing on the He ignition, initially, the He is ignited in a shell around the core. The temperature rises rapidly, i.e., without a cooling stabilizing expansion, and since the He fusion reactions are temperature sensitive, this process is further accelerated. Quickly, the entire core starts to fuse He. This phase is referred to as He core flash (in figure [1.1](#) it is marked as the *He core flash*). The overlaying layers of the envelope absorb the energy produced during this rapid phase. First, it “lifts” the degeneracy of the core by decreasing the density and temperature and hence slows the reaction rate ([Carroll & Ostlie 1996](#), pg. 462). The star now enters a new stage of life. On an HRD (see figure [1.1](#)), it is called the horizontal branch (HB); since it is only that the  $T_e$  increases and luminosity remains constant more or less, the stars in this stage move almost horizontally on the HRD. Increase in  $T_e$  is analogous to MS, i.e., core-He burning increases the  $T_e$ , but with a much shorter timescale. Simultaneously, H burns in a shell around the He core. From Figure [1.1](#), it is clear that the star doesn’t spend much time burning He in the core. Furthermore, since the star suffers mass loss during the RGB phase, the position of the HB depends upon how much mass was lost. The more mass loss, the bluer their position is on the HB ([Kippenhahn et al. 2012](#), pg. 408). This has “exotic” consequences in massive globular clusters, i.e., it gives rise to extended horizontal branch stars. The evolution on the HB is analogous to the evolution on the MS. The He is converted to carbon and oxygen by the triple-alpha process on the HB ([Kippenhahn et al. 2012](#), pg. 462).

Eventually, the core is He-depleted, and temperatures are too cool to fuse products from He fusion (carbon and oxygen). This leads the core of the star to contract once again. This contraction ignites a He-shell (analogous to the one during the SGB) and a H-shell at different locations in the star. Core contraction again swells up the star,

and the star enters an evolutionary phase, similar to the RGB, called the asymptotic giant branch (AGB) phase.

### 2.2.3 Advanced Phases of Stellar Evolution

The AGB could perhaps be thought of as the He-shell-burning analog of H-burning-shell. However, the dominant energy source of the star is the He-shell-burning, and H-burning-shell is almost inactive ([Carroll & Ostlie 1996](#), pg. 463). At this moment, the star is called an early-AGB (E-AGB) star. Similar to what happens along the RGB, the convective layer is formed at the surface, which deepens, and the star goes through a second dredge-up phase. The star keeps ascending the AGB and goes through another evolutionary phase called the thermally pulsing AGB (TP-AGB), during which the star periodically experiences intense energy production due to H and He shell burning. Mass loss is prominent during this phase, similar to the RGB phase. It is this event which enriches the interstellar medium with elements other than H and He. Next, the star goes through a third dredge-up phase, and similar to earlier dredge-ups, material from the core is brought to the surface of the star. Finally, what is left is the exposed core of the star. The star now enters the final evolutionary stage of life called the WD .

Before the discussion moves forward to WDs, it is worth noting that not all stars go through all phases of the AGB as described above after their HB evolutionary phase; the evolution of a star after the HB phase depends strongly on the envelope mass. Since the CO-core size and mass loss during RGB are still poorly understood. A star with high envelope mass ascends the AGB and goes through TPs, eventually losing their outer layers and becoming extremely hot stars called post-AGB (pAGB) stars. For stars with intermediate envelope mass stars, they ascend the AGB but skip the TPs, eventually losing their outer layers and becoming hot stars called post-early-AGB (p-e-AGB) stars. Finally, stars with low envelope mass stars skip the AGB and TPs and directly become WDs with CO-core (see [Prabhu et al. \(2021\)](#) and references therein).

## 2.3 WD Stars

### 2.3.1 Introduction

Before delving into the discussions on the structure and evolution of WD stars, it is wise to briefly discuss the historical developments alongside a few crucial physical properties of WDs. The following discussion has been majorly adopted from [Althaus et al. \(2010\)](#).

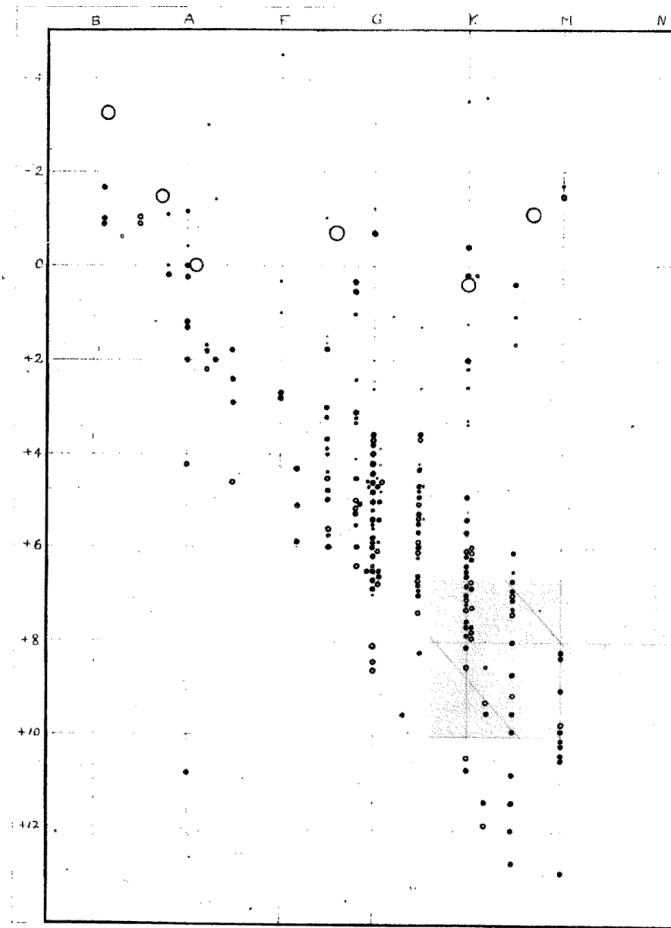


Figure 2.1: Henry Norris Russell's first diagram, whose y-axis has spectral types and x-axis has absolute magnitudes. A star named 40 Eridani B appears in the diagram at (A,+11) point. Figure adapted from [Russell \(1914\)](#).

WD stars have engrossed astronomers ever since they were discovered by Henry Norris Russell in 1914 when he noticed an unusual star now named 40 Eridani B below the main sequence on the HRD (see figure 2.1). The observations of 40 Eridani

B and Sirius B disclosed that these stars have radii comparable to Earth's (hence called "dwarf") and thus were intriguing ever since they were discovered. Based on its mass and luminosity, initial estimates of Sirius B's density implied it was extraordinarily high. In 1915, when Walter Sydney Adams determined the spectral type and luminosity of Sirius B, the mean density of a WD was calculated for the first time, which was found to be of the order of  $10^7$  kg/m<sup>3</sup>. However, the generally accepted value of the density of a WD in recent times is  $10^9$  kg/m<sup>3</sup>. This *new* variety of stars was different from ordinary stars and could only be explained theoretically after the birth of quantum mechanics. In truth, the existence of these stars provided initial proof of Pauli's Exclusion Principle, one of the most fundamental principles of quantum mechanics. In 1926, William Alfred Fowler discovered that it is a pressure due to "closely" packed electrons, called the electron degeneracy pressure, that counters a WD star's gravity. Investigations by Wilhelm Robert Karl Anderson, Edmund Clifton Stoner, and Subrahmanyan Chandrasekhar on this topic resulted in discovering the upper mass limit of a WD , known as the Chandrasekhar's mass limit (CML). This has been discussed in detail in section 2.3.2. Imaging surveys such as the Sloan Digital Sky Survey (SDSS) have expanded our knowledge of WDs. As mentioned in [Althaus et al. \(2010, pg. 6\)](#), the mass distribution of WDs peaks at  $0.562 M_{\odot}$ ; the tail of this distribution extends to higher values of WDs. Out of various methods to classify stars, one is done based on their spectral class. The spectral type of WD stars is "D" (for degenerate), which has several further divisions, such as DA, DB, DC, DQ, and DZ (See Table 2.1). Now, with this knowledge, the discussion on the structure and evolution of WDs resumes.

### 2.3.2 Degeneracy Pressure

This section discusses the nature of the matter and the structure of WDs. WDs exist because electron degeneracy pressure counters the gravity of the star. The matter inside is degenerate, and the ideal gas equation can no longer explain the equation of

Type	Characteristics of Spectra	$T_e$ (K)
DA	Only H absorption lines	11000 – 30000
DB	Only He absorption lines	11000 – 30000
DC	No lines, only continuum devoid of features	< 11000
DQ	Carbon absorption lines	< 11000
DZ	Metal absorption lines	< 11000

Table 2.1: This table showcases the characteristics and effective temperatures ( $T_e$  in units of 1000 K) of the spectrum of different types of WDs. Values used in this table have been taken from [Carroll & Ostlie \(1996, pg. 559\)](#) and [Althaus et al. \(2010, pg. 9\)](#).

state. Quantum mechanical tools are required to write the equation of state. At first, an expression for *degree of degeneracy* ( $\mathcal{D}$ ) is derived, which helps differentiate between a WD's degenerate and non-degenerate matter as is illustrated upon in section [2.3.3](#). Following this, an expression for degeneracy pressure is derived, and its application is used to write the equation of state for degenerate matter. Further, Chandrasekhar's theory of the WD is discussed, and a special relation between the mass of a WD ( $M_{WD}$ ) and its radius ( $R_{WD}$ ) is derived at the end of this section.

### Degree of Degeneracy

For matter made of fermions (fermionic matter), at  $T = 0$  K, all fermions are at the lowest energy state according to Pauli's exclusion principle. Matter now is called *degenerate* matter. At  $T > 0$  K, some fermions will be in an energy state other than the lowest energy state possible, and the matter would not be degenerate state. However, this is only true for low-density environments. As discussed now, the matter could still be degenerate, given the density is sufficiently high. Hence, the notion of the degree of degeneracy ( $\mathcal{D}$ ) comes into the picture. It is calculated here by the prescription given in [Carroll & Ostlie \(1996, pg. 565 - 566\)](#). It is known that Fermi energy<sup>2</sup> is given by,

$$E_F = \frac{\hbar^2}{2m} (3\pi^2 N(k_F))^{2/3}. \quad (2.1)$$

Here,  $N(k_F)$  is the number of electrons per unit volume, which can be estimated

---

<sup>2</sup>See Appendix.

as  $\frac{Z}{A} \frac{\rho_{\text{WD}}}{m_H}$ , where  $Z$  and  $A$  are the number of protons and nucleons, respectively, in the WD's nuclei, and  $m_H$  is the mass of a H atom and  $\rho_{\text{WD}}$  is the density of the WD. An electron will be *degenerate* if the thermal energy is less than the  $E_F$ , i.e., the electron will not be able to occupy higher energy states, therefore<sup>3</sup>,

$$\frac{3}{2}kT < \frac{\hbar^2}{2m} \left( 3\pi^2 \frac{Z}{A} \frac{\rho_{\text{WD}}}{m_H} \right)^{2/3} \implies \boxed{\frac{T}{\rho_{\text{WD}}^{2/3}} < \mathcal{D}} \quad (2.2)$$

The smaller the value of  $\frac{T}{\rho_{\text{WD}}^{2/3}}$ , the more degenerate the gas. The implications of this will be further used in section 2.3.3. Next, a derivation of the degeneracy pressure follows.

### Degeneracy Pressure of Electron (Fermi) Gas

From the kinetic theory of gas, it is known that the pressure  $\mathcal{P}$  arising from the random motion of particles constituting the gas is given by the following expression,

$$\mathcal{P} = \int \frac{1}{3} vp f(p) 4\pi p^2 dp. \quad (2.3)$$

Here,  $f(p)4\pi p^2 dp$  is the number of particles with momentum between  $p$  and  $p+dp$ , and  $v$  is the velocity of the particle with momentum  $p$ . As discussed previously, electrons exert tremendous pressure at high densities since they are closely packed, which is called degeneracy pressure. On comparing eqn. 2.3 and A.1,  $f(p) = \frac{2}{h^3}$ , and hence the following relation for the degeneracy pressure is obtained.

$$\mathcal{P}_{\text{Dgn.}} = \frac{8\pi}{3h^3} \int_0^{p_F} vp^3 dp. \quad (2.4)$$

For non-relativistic calculations,  $v$  is given as  $v_{\text{non-rel.}}$ ,

$$v_{\text{non-rel.}} = \frac{p}{m_e}. \quad (2.5)$$

---

<sup>3</sup>here  $k$  is the Boltzmann's constant,  $k = 1.38 \times 10^{-23}$

Hence, combining 2.4 and 2.5, the final degeneracy pressure is obtained as,

$$\mathcal{P}_{\text{Dgn.}} = \frac{8\pi}{3h^3} \int_0^{p_F} \frac{p}{m_e} p^3 dp \implies \boxed{\mathcal{P}_{\text{Dgn.}} = \frac{8\pi p_F^5}{15h^3 m_e}}. \quad (2.6)$$

### Equation of State

Since the ideal gas equation is also classical, a new equation of state must be found. The equation of state of a WD can be written by calculating the electron number density ( $N(k)$ ). If  $X$  is the H mass fraction, then  $\frac{X\rho_{\text{WD}}}{m_H}$  is the  $N(k)$  contribution from H. From He the contribution is  $\frac{(1-X)\rho_{\text{WD}}}{2m_H}$ , since 0.5 electrons per atomic mass (Choudhuri 2010, pg. 130). Hence,

$$N(k) = \frac{X\rho_{\text{WD}}}{m_H} + \frac{(1-X)\rho_{\text{WD}}}{2m_H} = \frac{\rho_{\text{WD}}}{2m_H}(1+X). \quad (2.7)$$

From A.1,

$$\frac{8\pi p_F^3}{3h^3} = \frac{\rho_{\text{WD}}}{2m_H}(1+X) \implies p_F = \left(\frac{3h^3 \rho_{\text{WD}}}{8\pi \mu_e m_H}\right)^{1/3}, \quad (2.8)$$

where,  $\mu_e$  is the mean molecular weight of electrons ( $= \frac{2}{1+X}$ ). By substituting the above equation to 2.6, the equation of state for degenerate matter for non-relativistic momentum is obtained. It is given as,

$$\mathcal{P}_{\text{Dgn.}} = \left(\frac{3}{\pi}\right)^{2/3} \frac{h^2}{20m_e} \left(\frac{\rho_{\text{WD}}}{m_H \mu_e}\right)^{5/3} \implies \boxed{\mathcal{P}_{\text{Dgn.}} \approx \frac{10^7 \rho_{\text{WD}}^{5/3}}{\mu_e^{5/3}}}. \quad (2.9)$$

### Chandrasekhar's Theory

Subrahmanyan Chandrasekhar's pioneering work on WDs revolutionized the understanding of stellar evolution. Apart from profoundly influencing astrophysics and cosmology, this limit shaped the understanding of supernovae, neutron stars, and black holes. This limit is the upper bound on how massive a WD star could be. Classical physics fails to derive this since the distance between two particles is of the order of de Broglie wavelength, and hence, quantum mechanical effects are crucial to inculcate.

Moreover, since a WD is primarily made of electrons, which are indistinguishable particles, Pauli's exclusion principle comes into play early on. To understand CML in detail, the mathematical equation of a WD's structure is a prerequisite. Equation 2.9 is a polytropic relation. Even if relativistic momentum is considered, the equation of state relation is still a polytropic relation. Polytropic relations can be reduced to the Lane-Emden equation, which is solvable, given the boundary conditions. This treatment has been done in [Choudhuri \(2010, pg. 132 - 137\)](#) in detail. It follows from the solution of the Lane-Emden equation that for non-relativistic momentum, the mass and radius are related, which is the so-called mass-radius relation of a WD star.

$$R_{WD} \propto M_{WD}^{-1/3}. \quad (2.10)$$

A surprising thing happens when one solves the Lane-Emden equation considering relativistic momentum;  $M_{WD}$  is independent of the central value of density and is given by the following relation.

$$M_{Ch.} = 1.46 \left( \frac{2}{\mu_e} \right)^2 M_\odot. \quad (2.11)$$

This is celebrated as the Chandrasekhar mass limit. In a nutshell, when one solves the relativistic equation of state of degenerate matter, the maximum mass of the system has a limit. However, why is a fixed mass only valid for the relativistic momentum equation of state? The relativistic (solid curve) and non-relativistic (dashed curve) mass-radius relations match for less massive WDs (see figure 2.2). This is because for massive WDs, the  $p_F$  value increases due to an increase in  $\rho_{WD}$ , contrary to less massive WDs for which  $p_F$  increases due to  $\rho_{WD}$  and relativistic effects. By relativistic effects, it is meant that  $p_{FC} \approx m_e c^2$  ([Salaris & Cassisi 2005, pg. 202](#)). Further, WDs are stars that have no H left in their core; hence, by approximating  $X \approx 0$ ,  $\mu_e = 2$ , the  $M_{Ch.}$  becomes,

$$M_{\text{Ch.}} = 1.4 M_{\odot}. \quad (2.12)$$

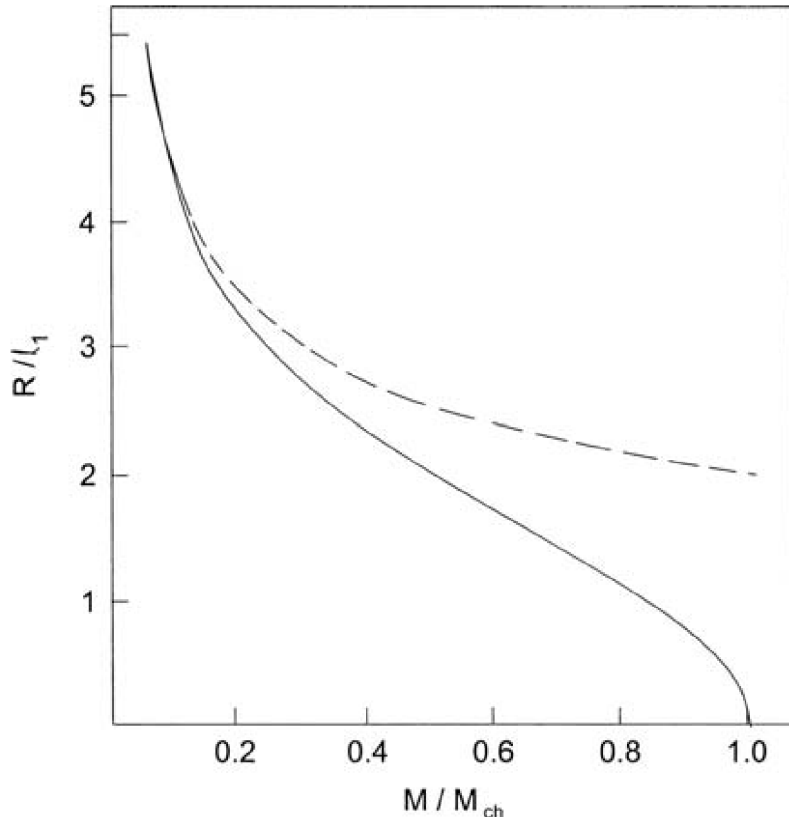


Figure 2.2: This plot shows the mass-radius relation for relativistic (solid curve) and non-relativistic (dashed curve) momentum. Figure adapted from [Chandrasekhar \(1984\)](#).

### 2.3.3 Cooling of WDs

Since no nuclear fusion occurs in WDs, their evolution is described as a pure cooling process. The source of their luminosity is the thermal energy of the ions (non-degenerate matter). This can easily be thought of since degenerate electrons are already in their lowest energy state and can't give away significant energy. This section discusses the cooling of WDs in two different regions of the star, the interior and the exterior.

The degenerate interior (the core of the star) of a WD is isothermal (due to very low opacity) [Salaris & Cassisi \(2005, pg. 204\)](#). In contrast, the non-degenerate outer

layers (the envelope of the star, refer to equation 2.2) have a steep temperature gradient. Only  $\sim 1\%$  of the total WD radius is the envelope. This creates an “edge” of the degenerate matter. A relation between the luminosity of the star and the temperature at the “edge” of the degenerate matter ( $T_{\text{Ed}}$ ) can be written  $L_{\text{WD}} \propto T_{\text{Ed}}^{7/2}$  (Salaris & Cassisi 2005, pg. 205). But it is known that the luminosity varies as the fourth power of surface temperature (effective temperature ( $T_e$ )). Hence, the core cools faster than the envelope. Furthermore, as mentioned in 1, WD luminosities and cooling ages have a tight relation. A simple model as discussed in Carroll & Ostlie (1996, pg. 575 - 576) shows that,

$$T_{\text{Ed}} = T_0 \left( 1 + \frac{5}{2} \frac{t}{\tau_{\text{cool}}} \right). \quad (2.13)$$

where,  $T_0$  is the temperature of the interior at time  $t = 0$  and  $\tau_{\text{cool}}$  is the timescale for cooling. This model is a good representation of the relationship between temperature and cooling time, but it is not the exact one. A more realistic model (see figure 2.3) includes H and He layers and considers crystallization. Since the core cools faster than the envelope, the center of the WD forms a crystalline lattice during which some latent heat is released. This latent heat extends the cooling time. Ultimately, the star becomes a “diamond in the sky” and ends as a solid crystalline black dwarf.

#### 2.3.4 He-core WDs

The discussions till now entailed the natural evolution of a low-mass star, i.e., evolution with no “external interventions” like stellar collisions or mass transfer. The product of such evolution is a CO-core WD . However, as mentioned in section 2.2.1, WDs with He core, called the He-core WDs, also exist. He-core WDs are an interesting class of WDs due to their formation scenarios. As discussed briefly, these WDs are yet to evolve without external interventions like stellar collisions or mass transfer; both cases are related to binarity. The relation to binarity for the formation of He-core WDs is natural. Suppose a red giant branch (RGB) star’s envelope is removed

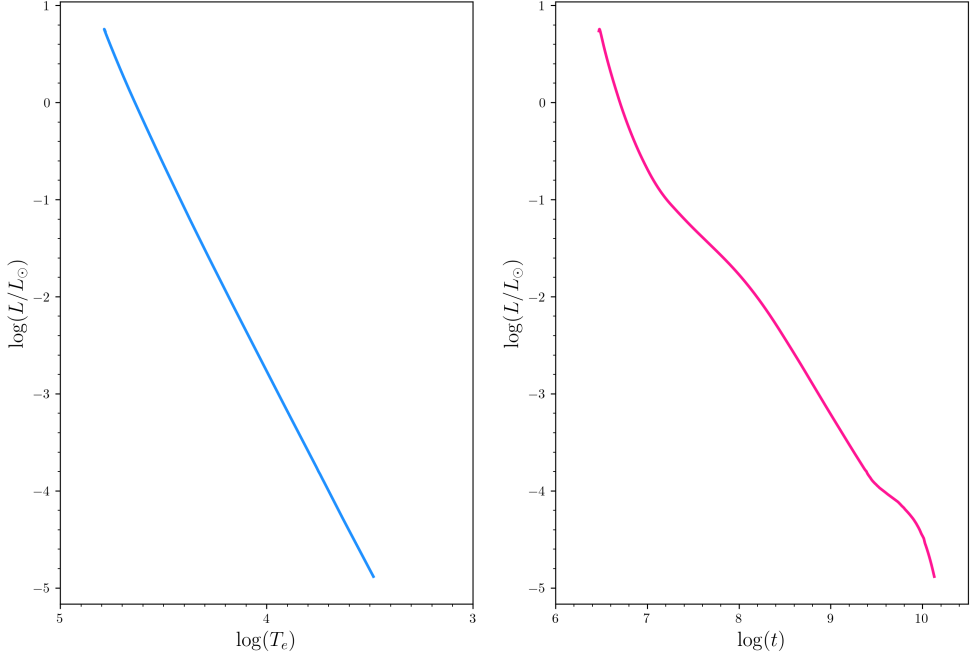


Figure 2.3: Left plot shows the luminosity vs. surface temperature relation (blue curve) whereas the right plot shows the luminosity vs. cooling age (pink curve) of a CO-core and H-envelope  $0.54 M_{\odot}$  WD Model downloaded from the [BaSTI](#) dataset. As is evident, with decreasing luminosity, the temperature decreases, and the cooling time increases.

before the He ignition at the tip of the RGB. In that case, the star's core will be exposed, resulting in a low-mass WD with a He core, whereas, if the star envelope is not removed, the star could evolve and become a CO-core WD. As proposed by [Webbink \(1975\)](#) this could occur via the Roche-lobe overflow mechanism and is the most widely accepted formation mechanism for these stars ([Althaus et al. 2010](#), pg. 25).

Apart from the aims stated in chapter 1, this study also investigates the presence of He-core WDs in NGC2808. In the field, He-core WDs are commonly found in binary systems, whereas, in globular clusters, only a few He-core WDs have been identified (like in NGC6397 ([Strickler et al. 2009](#)) and references therein) since it is difficult to detect these faint objects.

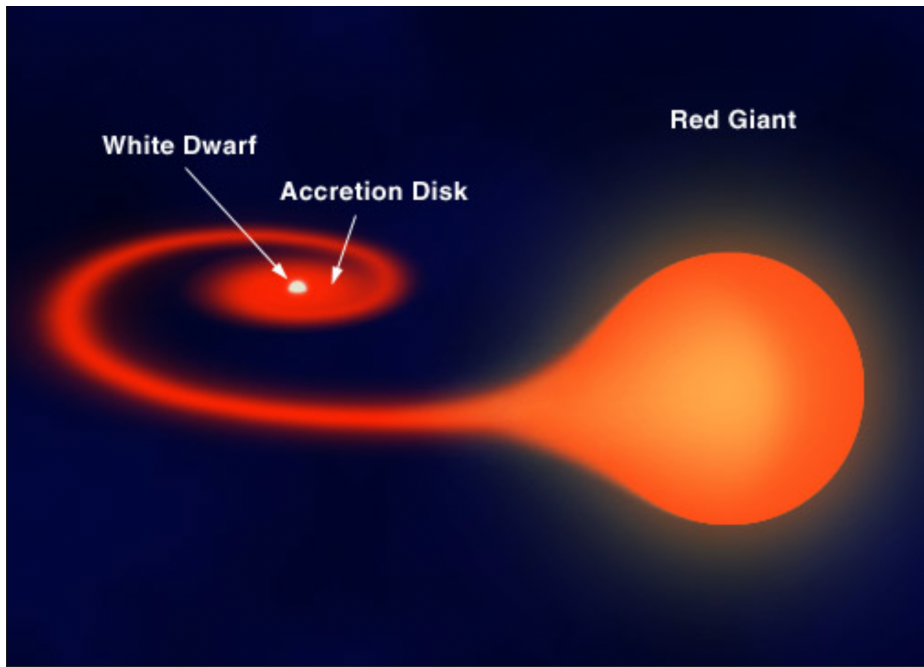


Figure 2.4: An artist's impression of a binary system comprising of a red giant star and a WD star. The WD accretes matter from the RGB leaving the core of the RGB exposed. This is the He-core WD and one of the mechanisms through which they form. This image is sourced from [here](#).

# Chapter 3

## Photometric Data of NGC2808

When Herr Wackher told Kepler about Galileo's telescope, the fellow astronomer immediately recognized its potential and wrote a eulogy: '*O telescope, instrument of much knowledge, more precious than any sceptre! Is not he who holds thee in his hand made king and lord of the works of God?*' Galileo would become that king and lord.

---

*Big Bang*, Simon Singh

### 3.1 Introduction

In this chapter, the discussion focuses on the data used in this study as well as the features of the “astrophysical laboratory” NGC2808. NGC2808 is a globular cluster located in the Carina constellation. Out of the 150 to 200 globular clusters that the Milky Way Galaxy hosts, it is one of the most massive clusters— $M_{\text{NGC2808}} = 7.42 \times 10^5 M_\odot$  ([Baumgardt & Hilker 2018](#)). Table 3.1 gives some parameters of this cluster. It is a highly unusual GC. But before discussing this cluster in detail, the data used in this study has been discussed.

As mentioned in chapter 1, this work utilizes data from the Hubble Space Telescope (HST). Hubble Space Telescope is a 2.4-meter reflecting telescope, which was deployed in low-Earth orbit (600 kilometers) by the crew of the space shuttle Discovery (STS-31) on 25 April 1990 and is operated by the Space Telescope Science Institute (STScI). It images the universe at ultra-violet (UV) and infrared (IR) wavelengths. The telescope also has low resolution spectroscopic capabilities in UV. On board the HST are the Advanced Camera for Surveys (ACS) and Wide Field Camera 3 (WFC3); apart from other instruments like Cosmic Origins Spectrograph (COS), Space Telescope Imaging Spectrograph (STIS), The Fine Guidance Sensors (FGS) and more.



Figure 3.1: Image of the Hubble Space Telescope. Source: [NASA](#).

The HST revolutionized the scientific understanding of globular clusters, which were thought to be “simple stellar population systems”, i.e., all stars belonged to a single generation. However, globular clusters are now known to host multiple stellar

populations (multiple generations) instead of the long-held view that they comprise a single stellar population (all stars formed in one burst). This is evident from spectroscopic and photometric data of various GCs. [Piotto et al. \(2015\)](#) presents the current understanding of GCs, summarized as follows. Firstly, except for Rup 106 and IC 4499, all known globular clusters are ubiquitous in terms of distinct stellar populations (from two to six or more, in example  $\omega$  Centauri). Secondly, the generation 1 (1G) stars (the first lot of stars that were born in the cluster) were formed from the proto-galactic interstellar matter and, during their evolution, went through mass loss events<sup>1</sup> which enriched the interstellar medium, forming the generation 2 (2G) stars. The 2G stars are enriched in N, Na, and He but depleted in C and O, possibly if 1G stars were relatively massive. Thirdly, no two GCs have been found to manifest the multiple stellar population phenomena similarly. Lastly, on a CMD, the multiple stellar populations can be separated using appropriate color (different combinations of UV, optical and IR filter systems).

One of the latest surveys of GCs by HST was the Hubble Space Telescope Ultraviolet Globular Cluster Survey (abbreviated as the HUGS survey). This study uses NGC2808 Method 3 photometric data from the HUGS survey available on the MAST<sup>2</sup> archive. The downloaded data (also called the catalog) contained photometric data of stars in five photometric filters named - F275W, F336W, F438W, F606W, and F814W. These range from near-ultraviolet (F275W and F336W) to optical (F438W and F606W) and infrared (F814W). Images in the F275W, F336W, and F438W filters were taken from the WFC3 facility, whereas images from the F606W and F814W were taken from the ACS facility. The HUGS survey provides data reduced by three different photometric techniques. Of the three methods, Method 1 works best for bright stars. Since the study's primary focus is faint objects, Method 1 was rejected. Out of Method 2 and 3, Method 3 works better in crowded environments and allows to resolve the cluster's center better than Method 2. Finally, the Method 3 photometry catalog was selected. The downloaded catalog contained data for 343134 objects.

---

<sup>1</sup>another scenario is that 1G stars were Fast Rotating Stars and enriched the interstellar medium

<sup>2</sup>[MAST Website](#)

The end-product of photometry is a catalog of all the objects detected in the image which has been reduced (Nardiello et al. 2018). For each object, the corresponding value of magnitude<sup>3</sup>, error in magnitude (d-param), sharpness parameter (s-param), and a PSF-fit correlation parameter (q-param) in each filter were given. Each has been discussed in section 3.1.1. Additionally, probability membership ( $P_\mu$ ), the RA and Dec, and ID were also given for each object.

Since the photometric data obtained from the HUGS survey is in five filters and plotting a unique CMD requires two filters, the total possible CMDs is ten (see figure 3.2). As will be shown next, for this study, only two of these ten CMDs were selected. The reason for this can only be explained after a brief discussion on d-param, q-param, and s-param. To plot a CMD, whose magnitude axis is  $m_{F275W}$  and color is  $m_{F275W} - m_{F336W}$ , for each star, the quantities  $m_{F275W}$  versus  $m_{F275W} - m_{F336W}$  were estimated and plotted.

---

<sup>3</sup>for the F275W, corresponding magnitude is written as  $m_{F275W}$

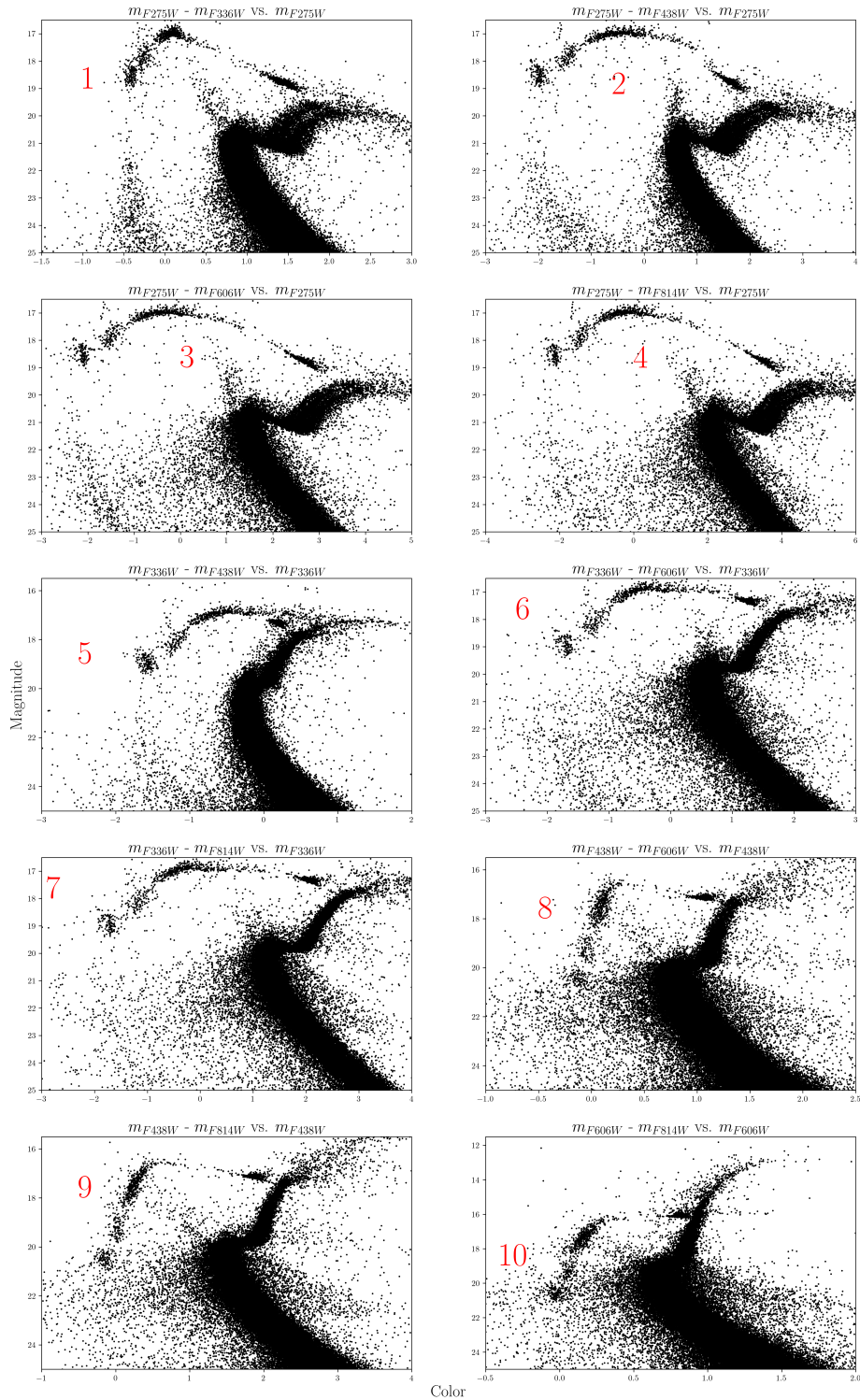


Figure 3.2: Figure shows all possible CMDs plotted using 5 filters. The color and magnitude are mentioned at each plot's top. Each plot has 343134 points, i.e., these are plotted using the raw data.

### 3.1.1 Quality Parameters

For each object, an error in magnitude (d-param), sharpness parameter (s-param), and a PSF-fit correlation parameter (q-param) was given. Together, these are called quality parameters. d-param is a parameter which the *kitchen\_sync2*<sup>4</sup> (KS2) routine returns and is the error in magnitude for a given object in a given filter. q-param is the goodness of the point source function (PSF<sup>5</sup>) fitting during the measurement of the position and flux of the star. It is useful to distinguish between stars and other astrophysical sources, such as cosmic rays and extended sources. The goodness is given as a linear correlation coefficient between the observed and the modeled pixels during the PSF fitting. The q-param value close to 1 implies the fit is good, whereas close to 0 implies the fit was poor. Next, the s-param is a shape parameter that helps distinguish between sources deviating from the PSF shape. It measures the excess flux in the pixels just outside of the core than the PSF prediction (Bedin et al. 2008). For objects whose s-param  $> 0$ , the source is an extended source (for example, a galaxy), whereas for objects whose s-param  $< 0$ , the source is sharper than expected (for example, a cosmic ray). Figures 3.3, 3.4, 3.5 show how d-param, q-param, and s-param vary for each across different filters, with magnitude. Corresponding parameter histograms are been plotted in the same figure.

---

<sup>4</sup>It is a FORTRAN software (Nardiello et al. 2018) used to reduce the images taken by the HST.

<sup>5</sup>The point spread function (PSF) characterizes how a focused optical imaging system responds to a point source or object.

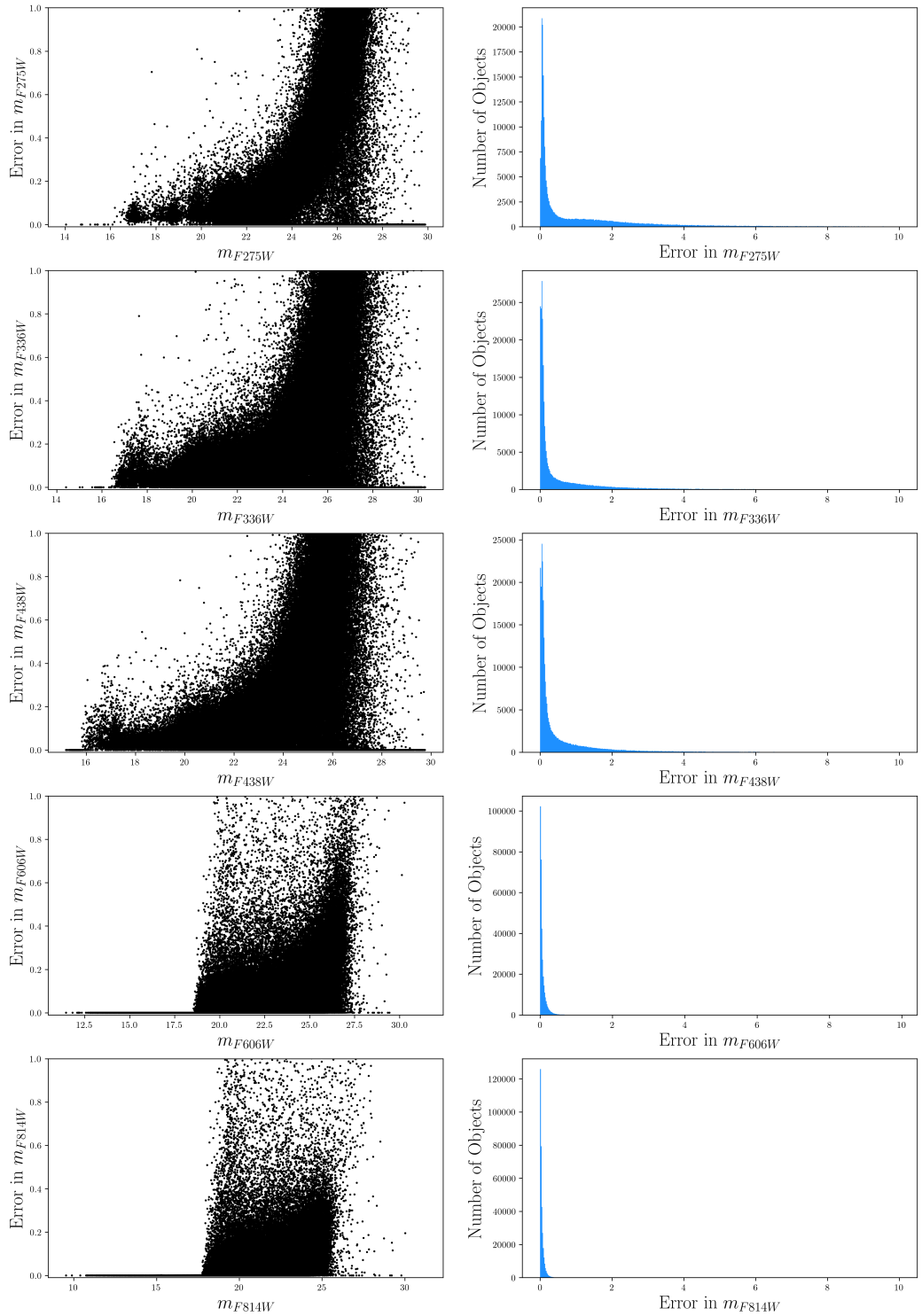


Figure 3.3: The left-hand-side plots show the error in magnitude (d-param) vs. magnitude for each object in the dataset, whereas the right-hand-side plots show the histogram of error in magnitude.

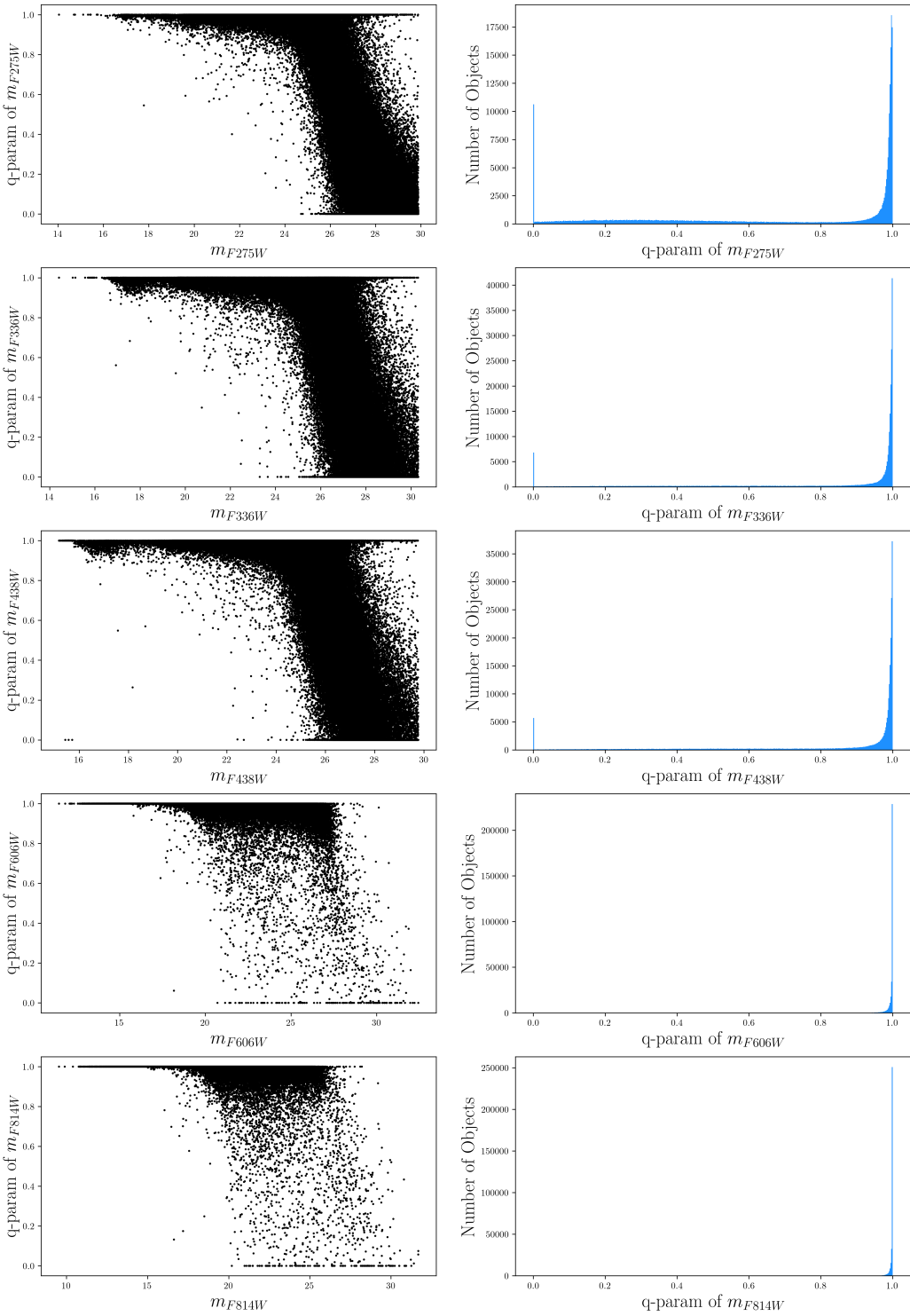


Figure 3.4: The left-hand-side plots show the q-param vs. magnitude for each object, whereas the right-hand-side plots show the histogram of q-param values.

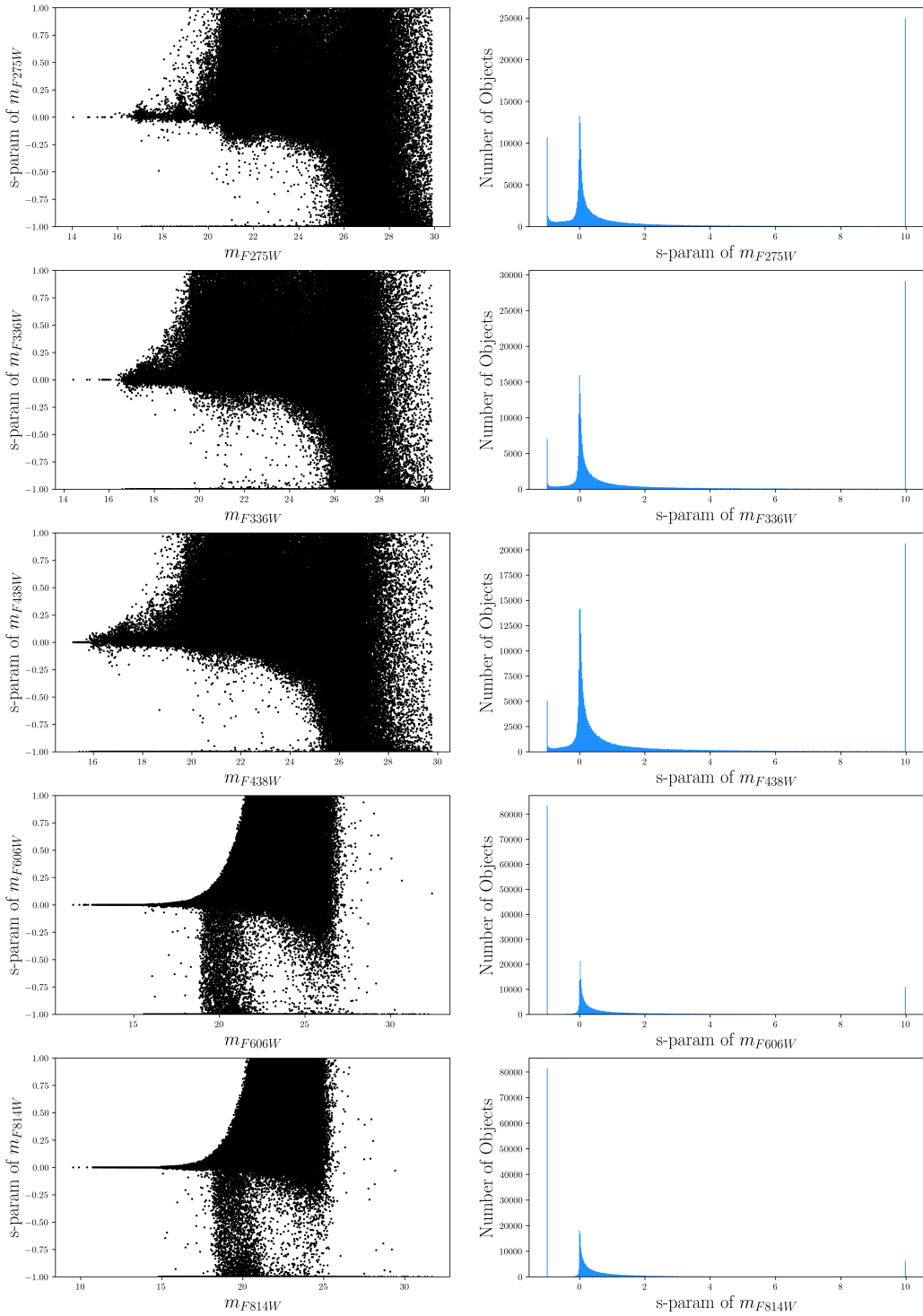


Figure 3.5: The left-hand-side plots show the sharpness parameter (s-param) vs. magnitude for each object, whereas the right-hand-side plots show the histogram of sharpness parameter values.

### 3.1.2 CMD Selection

The discussion returns to the selection procedure for selecting the two CMDs used in this study. Out of the photometric data obtained for the five filters, the photometric data from the F606W and F814W lacked depth and hence were not suitable for studying WDs. This can be shown from the figure 3.3, 3.4 and 3.5. The trend from the data plotted using these filters varies from the other three. After this, only 1, 2, and 5 subplots from figure 3.2 were retained. Since this study's primary objective is WDs which are brighter in UV and also bluer in color filters. Hence we choose to work with one of the UV filter (F275W) and the two optical filters F336W and F438W to estimate the color with respect to F275W. The two resulting CMDs are given in figure 3.6.

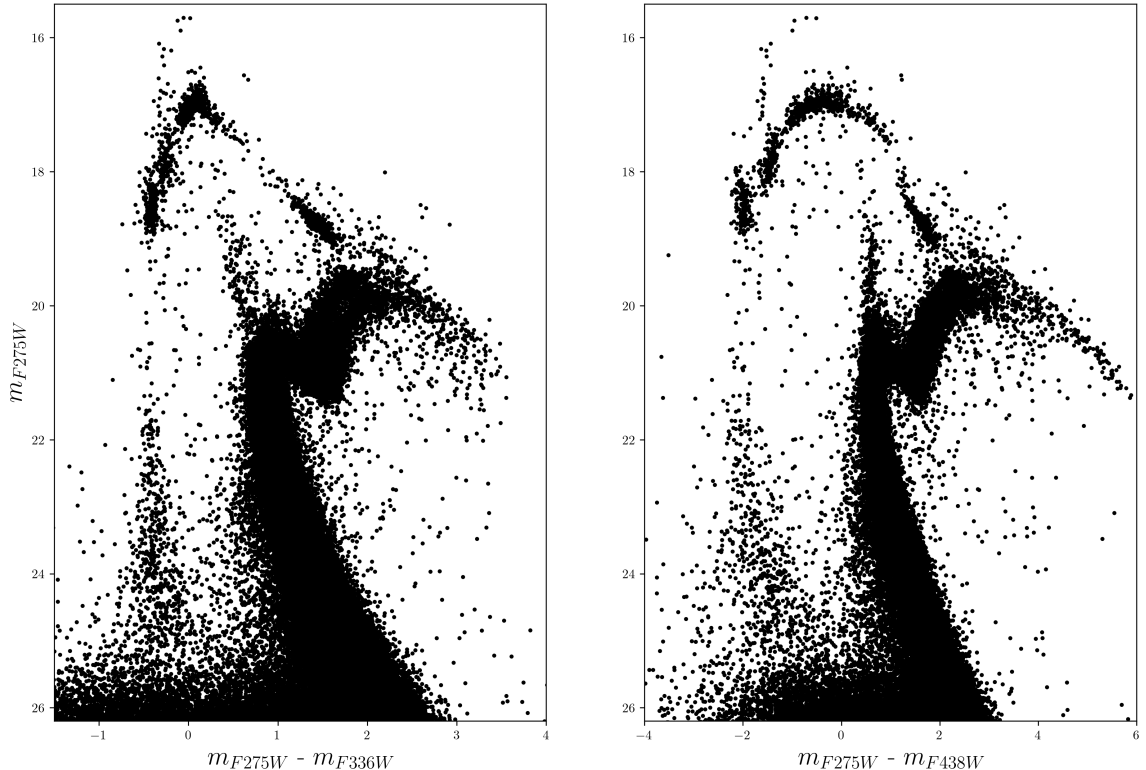


Figure 3.6: Figure shows the two CMDs which will be used for further analysis. The left CMD is a  $F275W - F336W$  vs.  $F275W$ , whereas the right CMD is a  $F275W - F438W$  vs.  $F275W$ . Same as figure 3.2, each plot has 343134 points.

## 3.2 Data Cleaning

Probability membership ( $P_\mu$ ) is a parameter defined for each object, which is calculated using the proper motion<sup>6</sup> data from different epochs. It tells how probable a star is to be a cluster member and can be used to remove spurious points on the CMD. To clean the photometric datasets, the traditional and the most undisputed method is to apply a probability membership cut to the objects that are to be plotted on the CMD, i.e., say the cut is 60%; all objects whose  $P_\mu$  is more than 60% are plotted. Figures 3.7 and 3.8 show that the total count reduces to almost one-third on applying a  $P_\mu$  cut. However, this parameter is calculated using bright stars only (Nardiello et al. 2018) and hence cannot be used to clean regions of the CMD where fainter objects are found. This is seen in the figures 3.7 and 3.8 since the WD sequence does not make any  $P_\mu$  cut. For such cases, a cut on s-param is used. Bedin et al. (2008) derived this parameter specifically for cleaning a CMD such that WDs were retained. This works since WDs are sharp objects Bedin et al. (2008) and could be well judged by a sharpness parameter. In addition to using s-param to clean the CMD for WD, this study also used d-param to clean the WDs. CMDs with these two cuts have been presented in the section 4.2.3 figure 4.8.

---

<sup>6</sup>motion of astrophysical object along the plane perpendicular to the line of sight of the observer

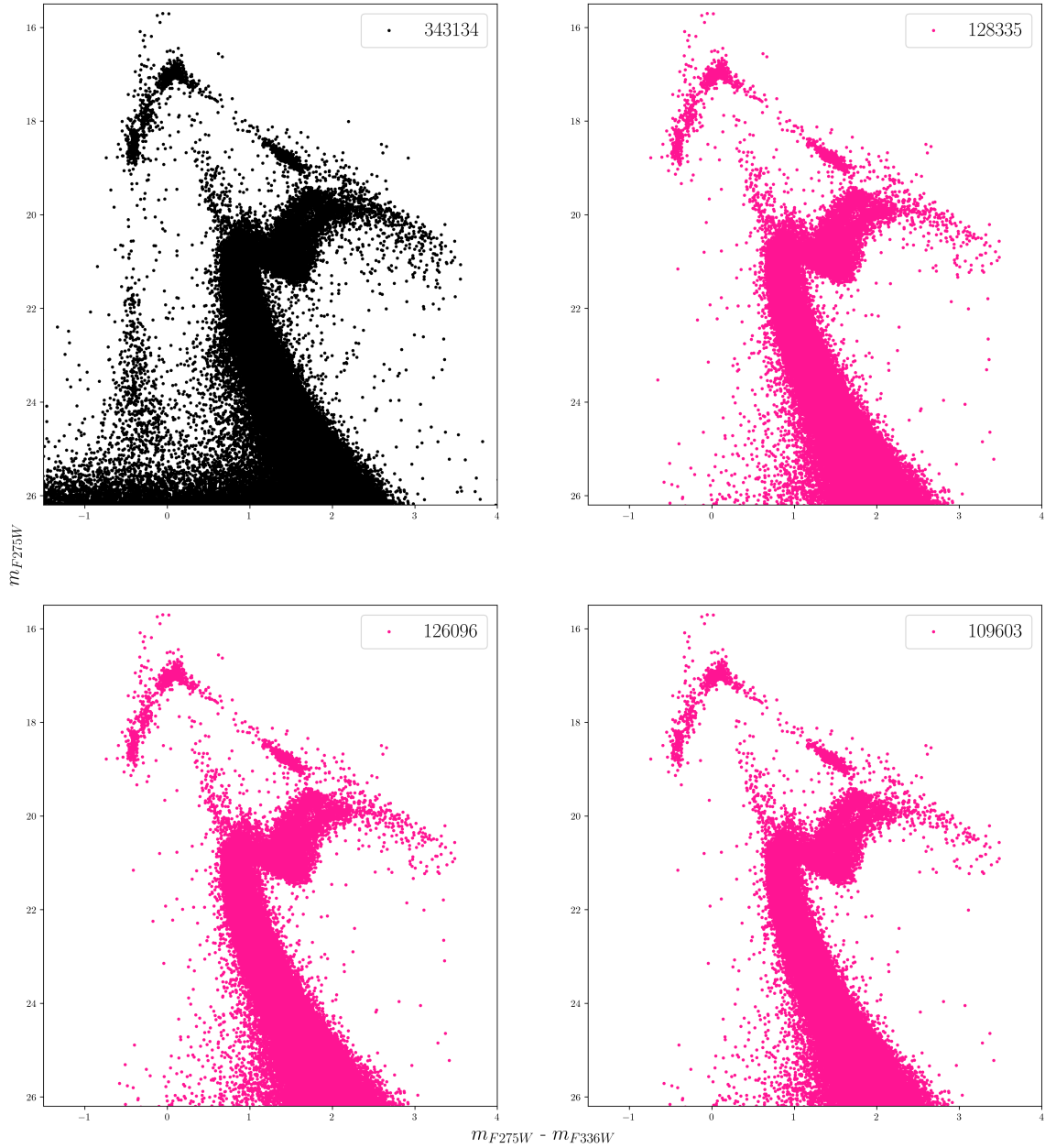


Figure 3.7: Top-left plot is the  $F275W - F336W$  vs.  $F275W$  CMD with no cuts. Other plots are of the same color and magnitude but with varying  $P_\mu$  cut as 60% (top-right), 80% (bottom-left), and 95% (bottom right). The number of objects retained in each case is noted in the respective plots.

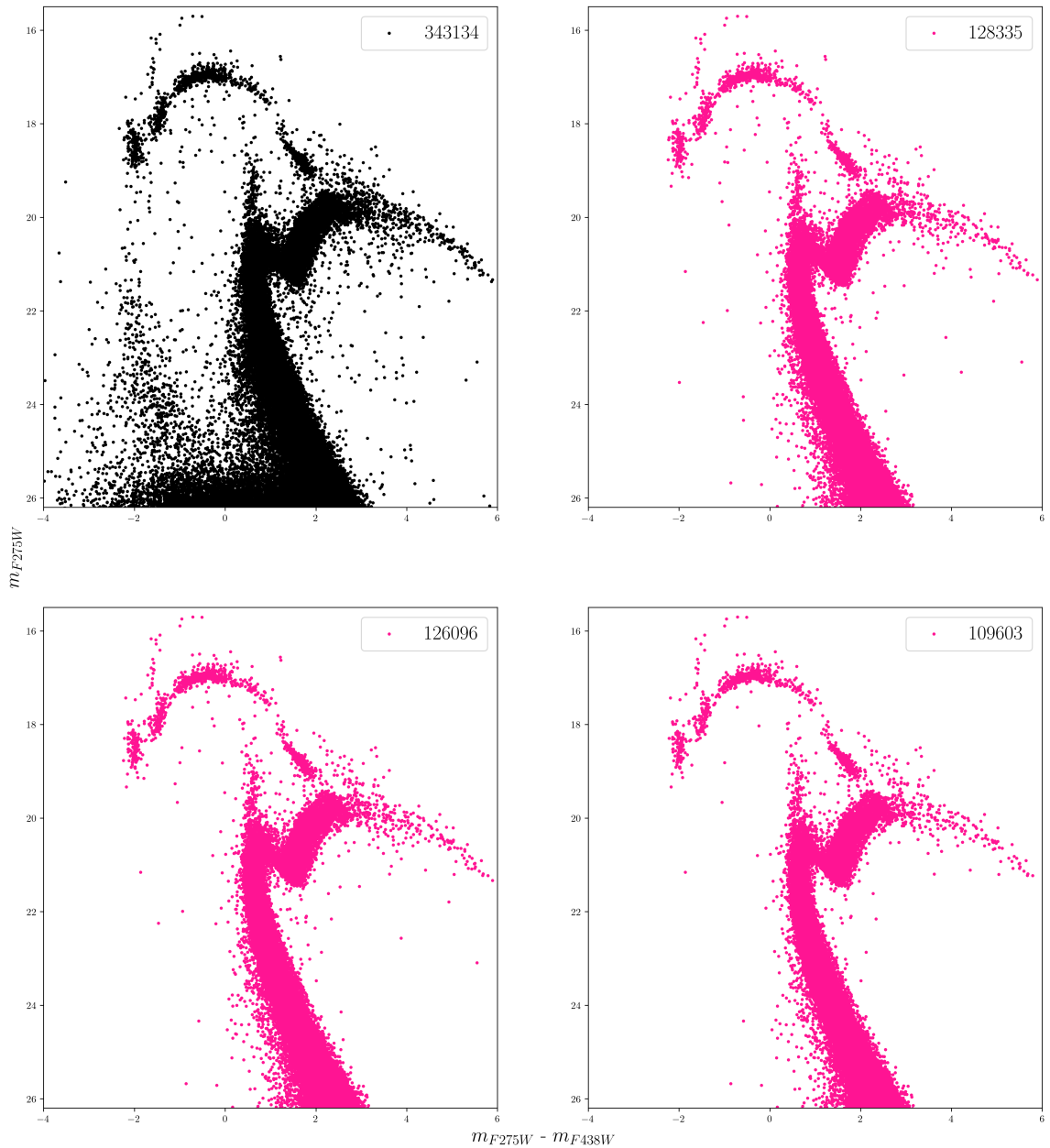


Figure 3.8: Same as figure 3.7 but with color F275W - F438W.

### 3.3 CMD Features of NGC2808

This section discusses the CMD features of NGC2808, which make this cluster unusual and, hence, an intriguing cosmic structure. Firstly, these features are discussed in detail through five key points elaborated upon in this section. The last two points are based on the literature review for this study. In the latter part, a spatial plot of NGC2808 has been presented. This cluster's important positional, photometric, and structural parameters have been summarised in table 3.1 below.

Parameter	Value	References
$\alpha$ (J2000)	138.0071	<a href="#">Gaia Collaboration et al. (2018)</a>
$\delta$ (J2000)	-64.8645	<a href="#">Gaia Collaboration et al. (2018)</a>
$\mu_\alpha$ (2015)	$0.994 \pm 0.024$	<a href="#">Vasiliev &amp; Baumgardt (2021)</a>
$\mu_\delta$ (2015)	$0.273 \pm 0.024$	<a href="#">Vasiliev &amp; Baumgardt (2021)</a>
$M_V$ (mag) <sup>a</sup>	-9.4	<a href="#">Harris (2010)</a>
$r_c$ (arcmin) <sup>b</sup>	0.26	<a href="#">Trager et al. (1995)</a>
$r_h$ (arcmin) <sup>c</sup>	0.86	<a href="#">de Boer et al. (2019)</a>
$r_t$ (arcmin) <sup>d</sup>	21.97	<a href="#">de Boer et al. (2019)</a>
$\log(t_h)$ <sup>e</sup>	8.9	<a href="#">McLaughlin &amp; van der Marel (2005)</a>
$E(B - V)$ <sup>f</sup>	$0.19 \pm 0.03$	<a href="#">Schlafly &amp; Finkbeiner (2011)</a>
$\mu_0$ (mag) <sup>g</sup>	15.05	<a href="#">Harris (2010)</a>

Table 3.1: Table shows the positional, photometric, and structural parameters of NGC2808. The subscripted parameters means: <sup>a</sup>Total visual magnitude, <sup>b</sup>Core radius, <sup>c</sup>Half-mass radius, <sup>d</sup>Tidal radius, <sup>e</sup>Log of relaxation time, <sup>f</sup>Reddening, <sup>g</sup>True distance modulus.

1. Split in the Main Sequence and Red Giant Branch: [Piotto et al. \(2007\)](#) discovered that the MS of NGC2808 splits into three separate main sequences (see figure 3.9) and [Milone et al. \(2015\)](#) found that the MS and RGB consists of five distinct stellar populations. All five stellar populations have different helium abundance. However, the scenario that each stellar population could be associated with a single period of stellar formation and that mass loss from stars could enhance the interstellar medium for the next period of stellar formation and, hence, enhancing the helium content in stars is a quantitatively very attractive scenario, but it fails. Simulations state that mass loss would have had to

be unusually large, and the initial mass function would be much flatter (Piotto et al. 2007). Another proposed scenario is that of the massive rotating stars that undergo mass loss. But this, too, fails to explain the presence of multiple stellar populations since the stellar winds they would generate would not be retained in a GC. This is just one fascinating reason to make globular cluster systems intriguing. The existence of multiple stellar populations is still under investigation and poses intriguing questions to astronomers.

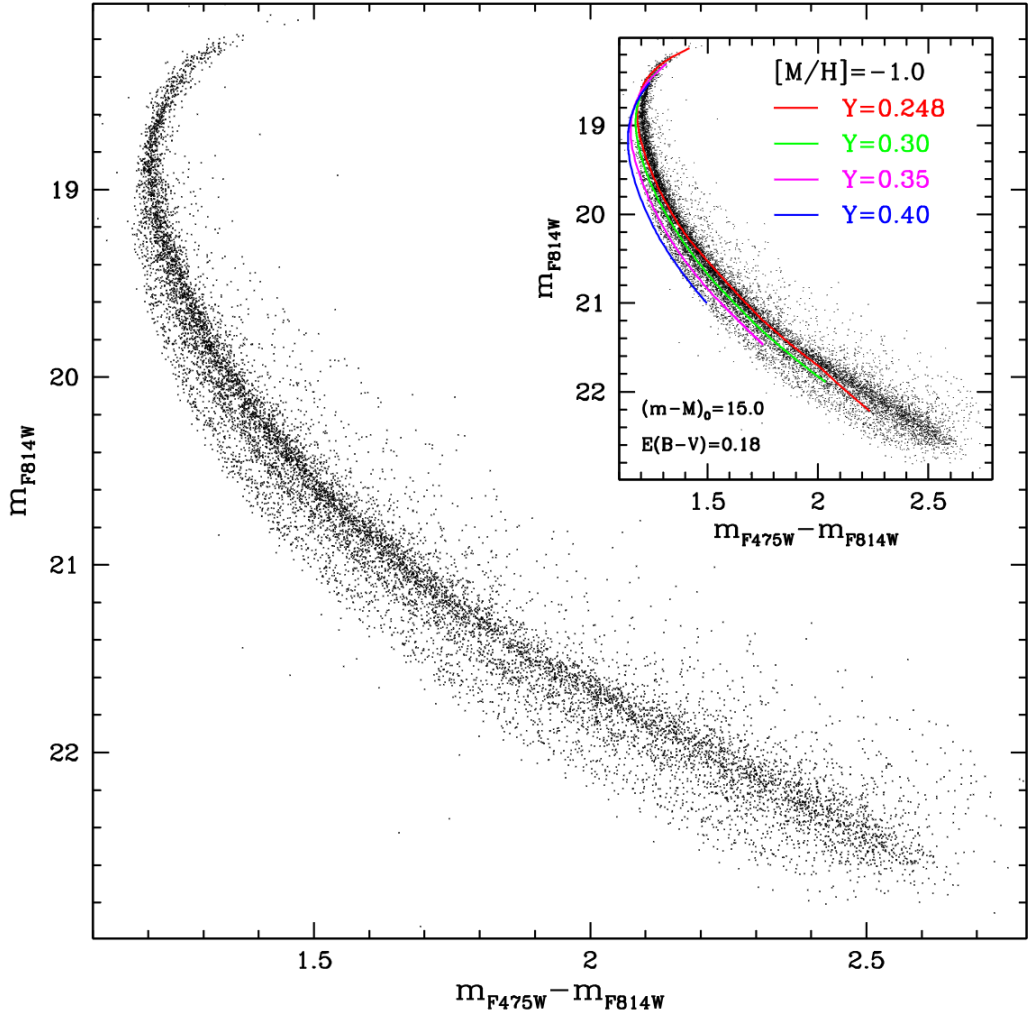


Figure 3.9: Figure shows a F475W - F814W vs. F814W CMD shows the split in the MS in three. (Adapted from Piotto et al. (2007, fig. 2)).

2. Blue Straggler Stars: These are the stars that are brighter and bluer than the MS on a CMD (see figure 3.10). BSS have more H-fuel and are thought to

be born either from mass-transfers in binary systems or due to stellar collision. Their formation and evolution is not completely understood.

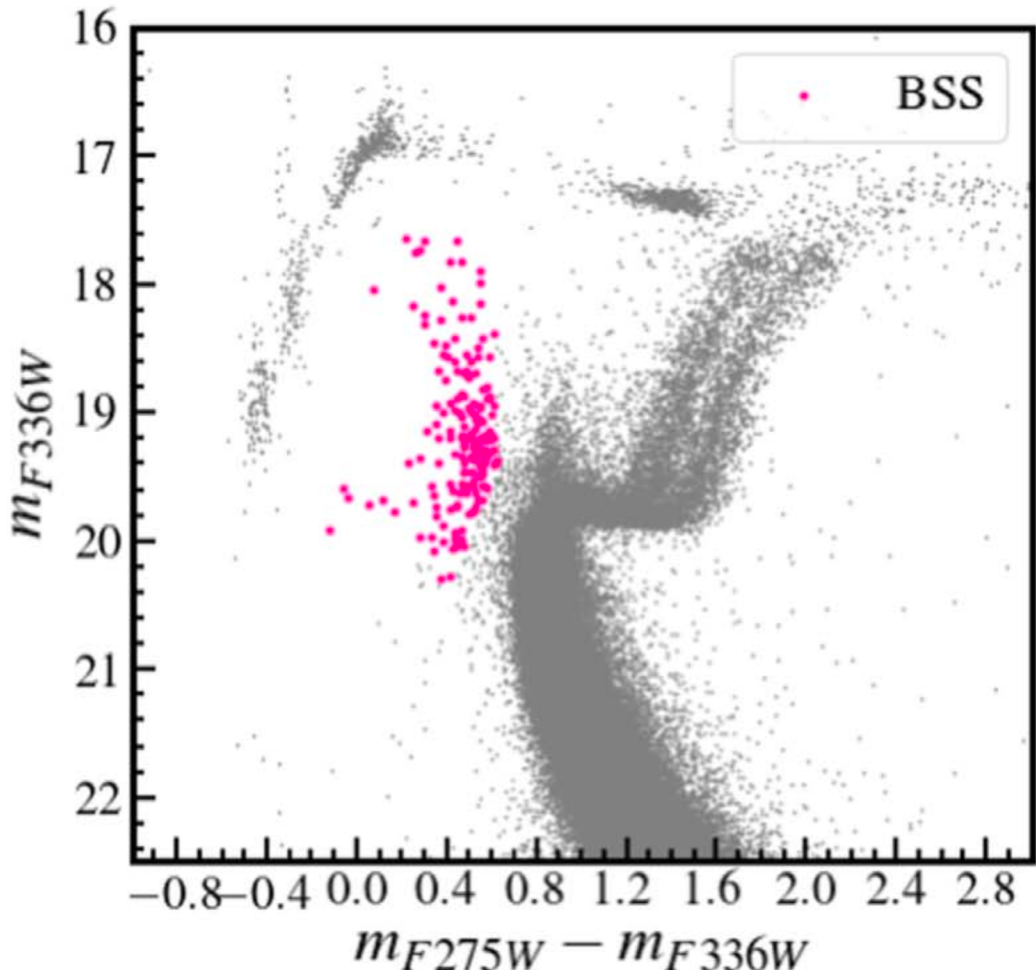


Figure 3.10: Figure shows an F275W - F336W vs. F336W CMD highlighting the blue straggler stars (pink colored) in NGC2808. (Adapted from [Prabhu et al. \(2021, fig. 3\)](#)).

### 3. Horizontal Branch Morphology

(a) UV-Bright Stars: A population of UV-bright stars (see figure 3.11) are found in the HB NGC2808. [Prabhu et al. \(2021\)](#) (and references therein) studied them using the Ultra-Violet Imaging Telescope (UVIT) onboard AstroSat. These stars have exhausted helium in their core (post-helium-core-burning / post-horizontal Branch stars) and are extremely luminous. They are found above the HB and left of the RGB on a CMD. These stars are important to study since the scrutiny of these stars could shed more light on the CO core size of WDs, since these stars could eventually become WDs.

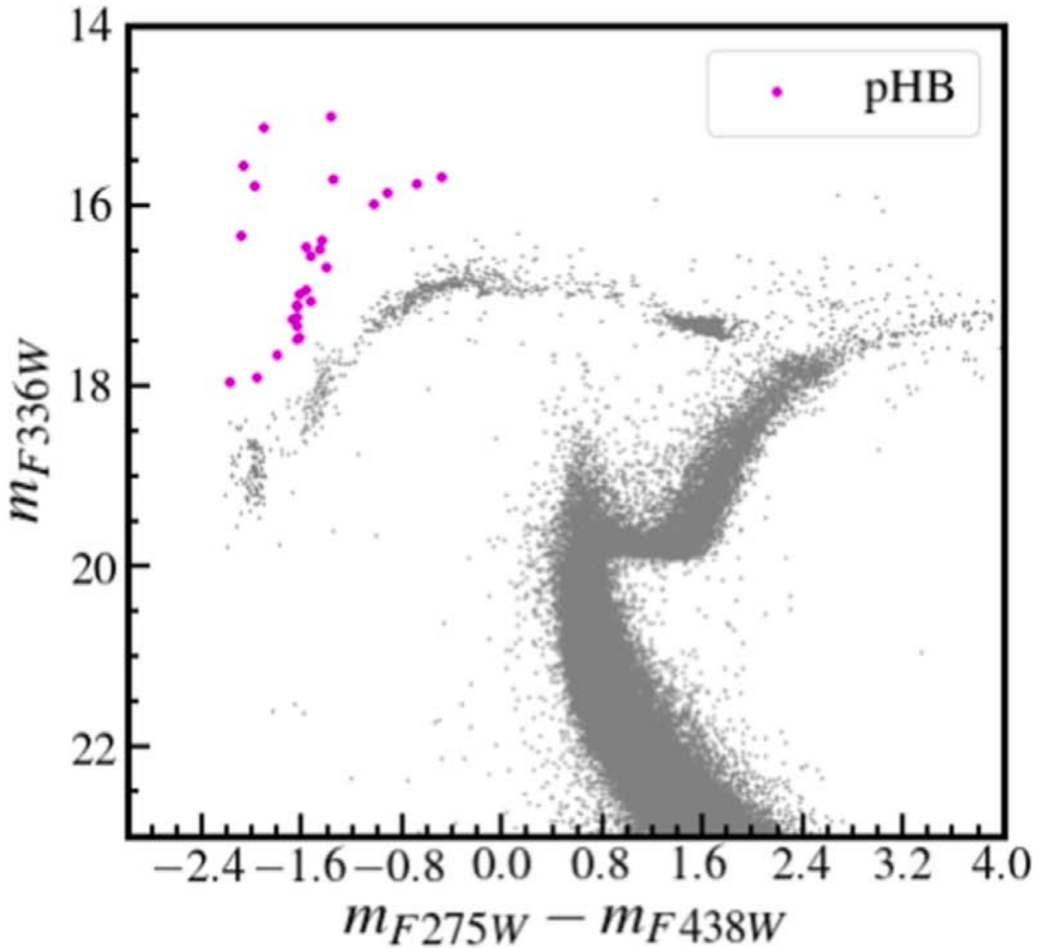


Figure 3.11: Figure shows a F275W - F438W vs. F336W CMD highlighting the UV-bright stars (purple coloured) in NGC2808 (Adapted from [Prabhu et al. \(2021, fig. 3\)](#)).

- (b) Extended Horizontal Branch Stars: Massive clusters such as NGC2808 tend to host significant populations of stars whose  $T_e > 20000$  K. These are called the extended horizontal branch (EHB) stars (see figure 3.12). These stars are the progeny of those RGB stars which retained thin envelopes ( $10^{-3}$  to  $10^{-2} M_\odot$ ) after undergoing mass loss on the RGB (Brown et al. 2012). A sub-variety of such stars are called the blue hook stars, which manifest as a hook at the end of the bluer EHB (see figure 3.12). Their origin is explained by the late-hot flasher scenario (Brown et al. 2001).
- (c) Gaps in the Horizontal Branch: Discontinuities (also called gaps or jumps) in the horizontal branch of massive clusters are common (see figure 3.12) and have been known since the 1970s (Harris 1974). For a recent discussion on these discontinuities, refer to Brown et al. (2016).

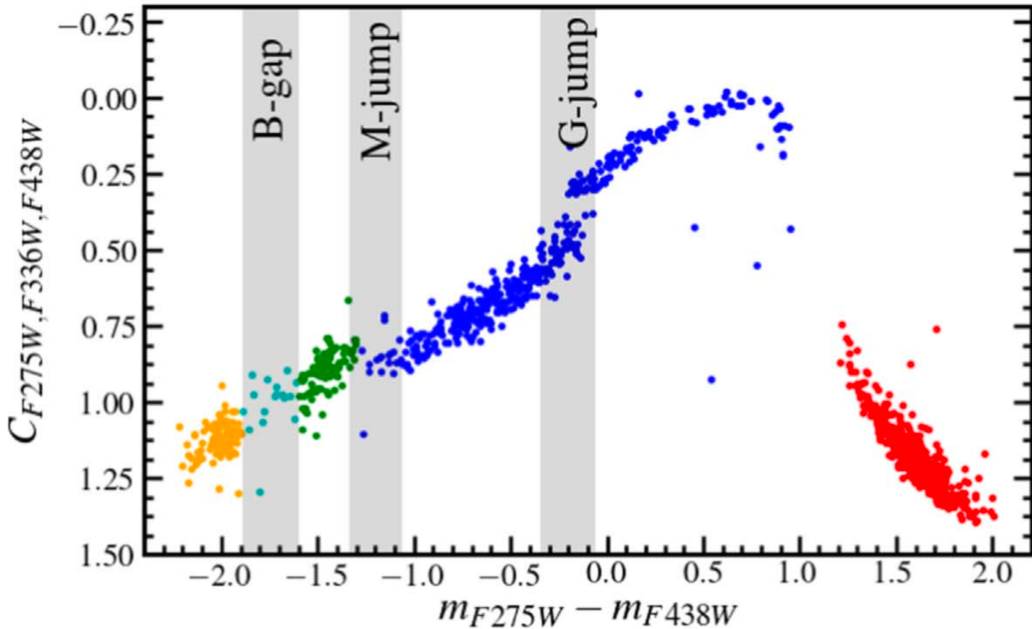


Figure 3.12: Figure shows a plot with a “special” plotted on both the y-axis and highlights the three gaps in the HB of NGC2808. Additionally, various varieties of HB stars, such as red horizontal branch (RHB) stars (in red), blue horizontal branch (BHB) stars (in blue), extreme horizontal branch (EHB) stars (in green), B-gap objects (in cyan) and blue hook (BHk) stars (in yellow). (Adapted from Prabhu et al. (2021, fig. 3)).

4. Bimodality in NGC2808 WD Sequence? Seeking inspiration from Bellini et al. (2013), this study aims to search for a split in the observed WD sequence. Bellini

et al. (2013) found a split (see figure 3.13) in the WD sequence (WDS) of the most massive GC that the Milky Way galaxy hosts,  $\omega$  Centauri. They found that the redder split of the WDS comprised 90% He-core WDs + 10% CO-core, and the bluer split hosted all CO-core WDs. Since NGC2808 and  $\omega$  Centauri are massive GCs and hence more prone to host binaries and, in turn, He-core WDs. A bimodality check could shed more light on this.

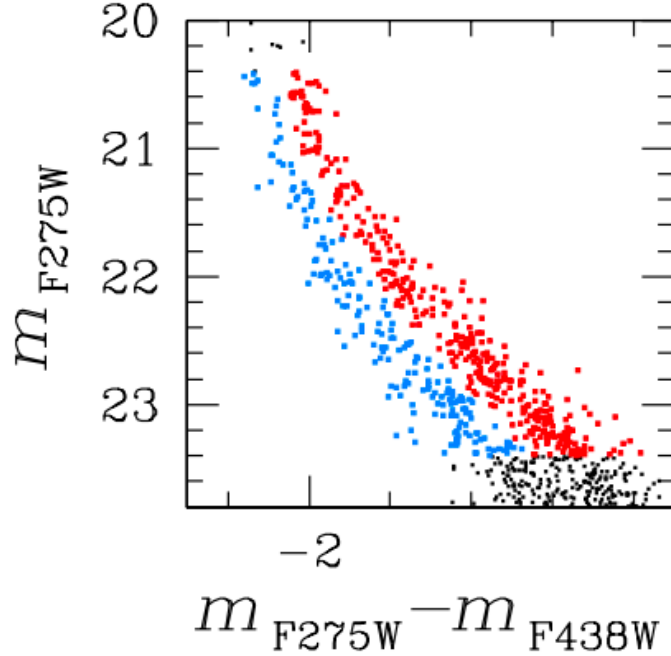


Figure 3.13: Figure shows a F275W - F438W vs. F275W CMD showing the spilted WD sequence in  $\omega$  Centauri. (Adapted from Bellini et al. (2013, fig. 3)).

5. A newly found variety of WDs —Slowly Cooling WDs (SCWDs): Chen et al. (2021) found a new variety of WDs, called slowly cooling WDs. These kinds of WDs skip the third dredge-up phase along the AGB and hence allow quiescent thermonuclear burning from the leftover hydrogen in their envelopes, thereby delaying cooling rates. This shows up in the luminosity function (magnitude histogram) since they “come down” the WD sequence very slowly. They are the progenies of EHB stars, and since NGC2808 hosts EHB stars, this cluster could be hosting SCWDs (see Chen et al. (2022) for more on SCWDs).

## Spatial Plot of NGC2808

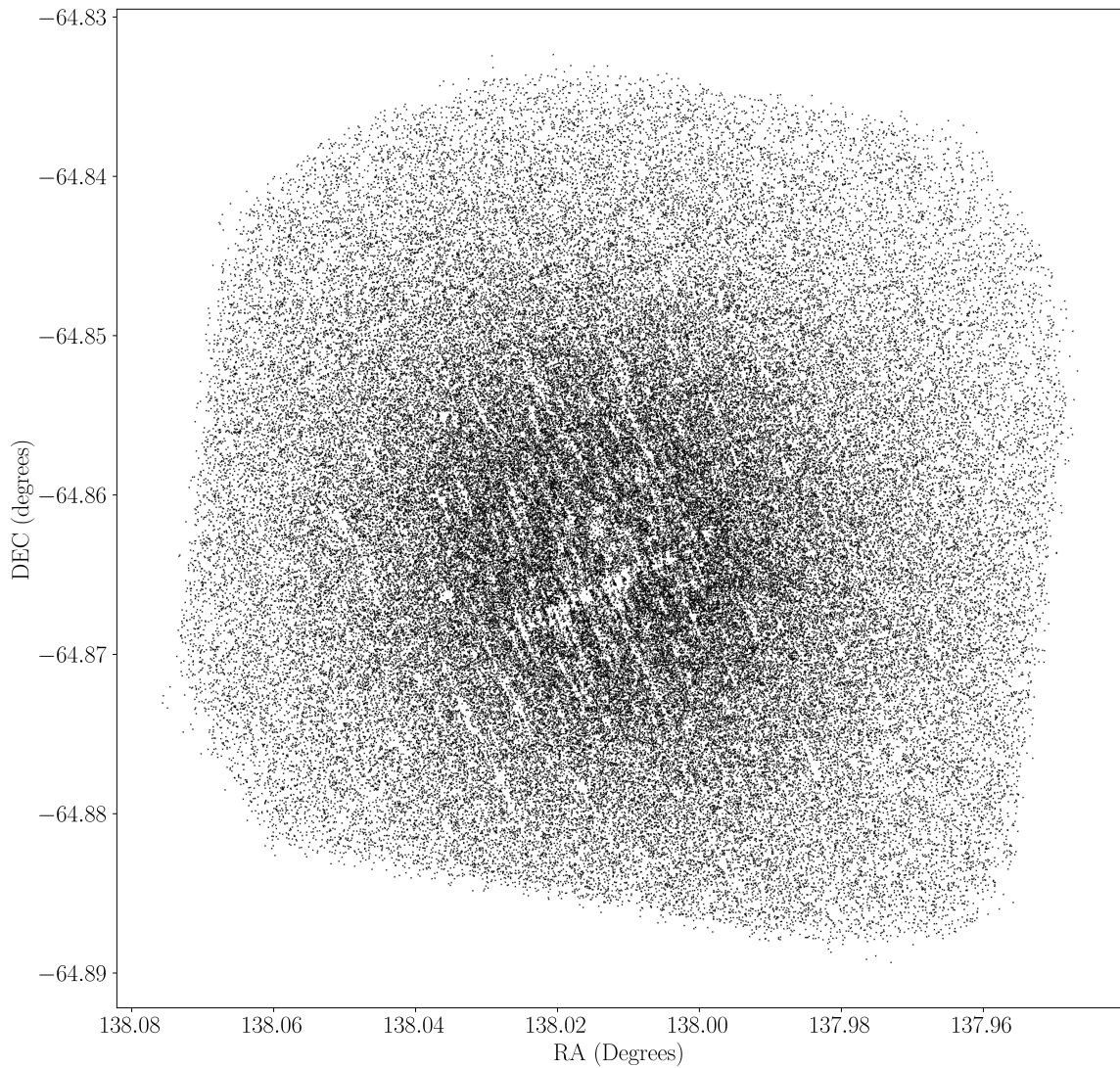


Figure 3.14: Figure shows an RA vs DEC plot of objects retained after a 60% cut on  $P_\mu$ .

# Chapter 4

## Methodology and Analysis

### 4.1 Introduction

The methodology of this study deals with the analysis of the CMD of NGC2808. As stated in [Renzini & Fusi Pecci \(1988, eqn. 1\)](#) the number of stars ( $N$ , star counts), in an evolutionary phase  $j$  and the time duration of the phase  $\tau_j$  are proportional.

$$N_j \propto \tau_j \quad (4.1)$$

This can be understood through analysis of globular cluster CMDs. In figure [3.7](#), the number of stars in the horizontal branch phase is higher than in the main sequence phase. This is because the core-helium burning (horizontal branch phase) occurs for a shorter time (see section [2.2.2](#)) compared to core-hydrogen burning, and hence, stars tend to “stay” on the main sequence for a longer time. Using equation [4.1](#), it is possible to relate the number of stars and the corresponding time duration of two evolutionary phases, say  $j$  and  $k$ , respectively, in the following way.

$$\boxed{\frac{N_j}{N_k} = \frac{\tau_j}{\tau_k}} \quad (4.2)$$

A phase’s time duration ( $\tau$ ) is also called the crossing time since it is the time it takes a star to cross a certain unit of color and magnitude on the CMD. Now, let

$$N_{\text{Obsv}} = \frac{N_j}{N_k} \quad (4.3)$$

and

$$\tau_{\text{Theo}} = \frac{\tau_j}{\tau_k}. \quad (4.4)$$

Once the star counts and crossing times have been computed for two evolutionary phases, the  $N_{\text{Obsv}}$  and  $\tau_{\text{Theo}}$  should be comparable.  $N_{\text{Obsv}}$  will also be referred as **observed ratio** and  $\tau_{\text{Theo}}$  as **theoretical ratio** in the sections below. Hence, the aim is to first perform star counts and calculate crossing times presented in the next section. In the latter half of this chapter, the ratios have been presented.

#### 4.1.1 Artificial Star Tests

Artificial Star Test (AST) is a statistical technique used to account for the completeness of data, especially when performing star counts, as in this study. This test gives a completeness parameter that tells how complete the data is for specific kinds of stars at a particular magnitude. The smaller the completeness parameter, the poorer the completeness. For this study, the AST for the MS & RGB (MS-RGB) stars and WD stars was done separately, and the corresponding completeness parameter value was plotted against  $m_{F275W}$  (see figures 4.2 and 4.1). A function was then fit to these plots, which are referred to as  $\Phi_{\text{MSTO-RGB}}$  and  $\Phi_{\text{WD}}$  for MSTO-RGB and WD stars, respectively. Both figures show that the completeness parameter worsens for fainter magnitudes. Hence, the magnitudes corresponding to 0.75 and 0.5 completeness levels were chosen as the faintest allowed magnitudes for which the star counts were performed for MSTO-RGB and WDs, respectively.

The luminosity functions (magnitude histograms) were plotted for the respective evolutionary phase star count selection to correct the star counts for completeness. Then, these stars were binned in magnitude, and the  $\Phi_{\text{MSTO-RGB}}$  was calculated by subtracting the values at the magnitude bin limits. This is elaborated in the following

section, where the completeness corrected star counts and crossing times for the main sequence, red giant branch, and WD sequence have been presented. From the figure 4.2, it is clear that the completeness of WDs brighter than 21 could not be accounted for.

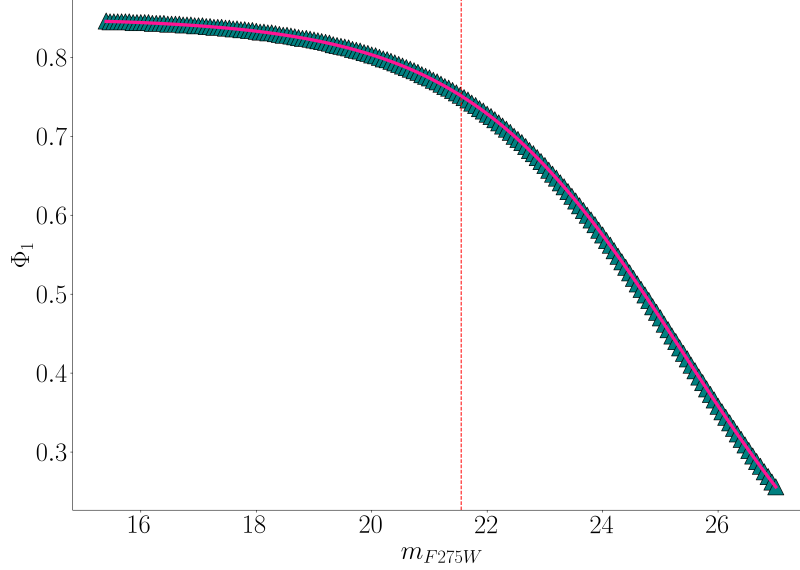


Figure 4.1: The teal-colored triangles are the completeness parameter for the MS-RGB ( $\Phi_1$ ) artificial star test corresponding to the  $m_{F275W}$ . A function ( $\Phi_{\text{MS-RGB}}$ ) was fit to this and is highlighted as the pink curve. A red dashed-dot vertical line shows the magnitude of the completeness at 0.75, i.e., 75%.

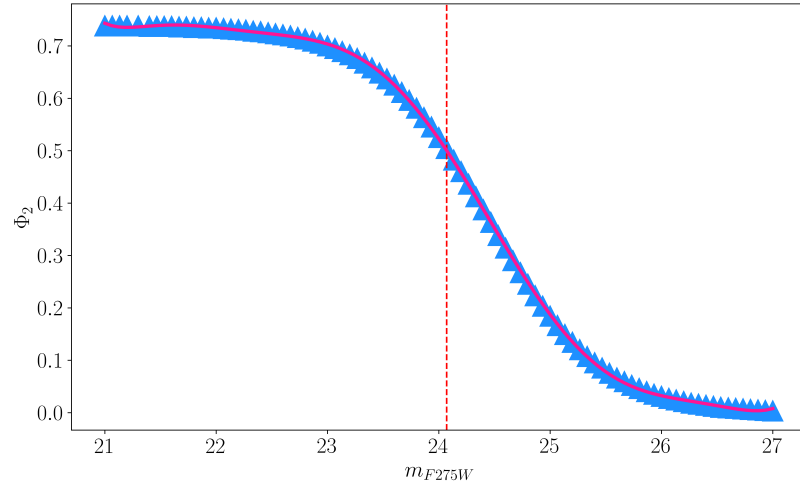


Figure 4.2: The blue-colored triangles are the completeness parameter ( $\Phi_2$ ) for the WD artificial star test corresponding to the  $m_{F275W}$ . A function ( $\Phi_{\text{WD}}$ ) was fit to this and is highlighted as the pink curve. A red dashed-dot vertical line shows the magnitude of the completeness at 0.5, i.e., 50%.

## 4.2 Star Counts and Crossing Times

### 4.2.1 Main Sequence Stars

To sample main sequence stars, MSTO stars were chosen. This was due to two reasons. Firstly, the population of stars of this region is minimally affected by the initial mass function, which has been proven observationally and theoretically (Zoccali & Piotto 2000). Secondly, this region is least affected by completeness problems (Castellani et al. 2007), and after inculcating artificial star test results, the counts are reliable. Figure 4.4 shows the selection of MSTO counts by the method explained below. We have used a similar technique as Calamida et al. (2008) used to perform star counts.

1. Select a CMD: 438CMD was selected with objects whose  $P_\mu > 60\%$  (see figure 4.3 bottom left plot).
2. Fitting<sup>1</sup> an isochrone<sup>2</sup>: A 10.9 Gyr isochrone was fitted on the 438CMD, using which the turnoff mass was calculated to be  $0.82 M_\odot$ , i.e., the mass of the bluest point on the isochrone. In figure 4.3, the blue curve on the bottom left plot is the 10.9 Gyr isochrone.
3. Employ a magnitude width: The limits of the magnitude width were decided by varying the turnoff mass by  $0.0030 M_\odot$ . This is referred to as the varying mass. The magnitude of the point on the isochrone of mass  $0.82 \pm 0.0030 M_\odot$  were selected to be the limits corresponding to 0.04 mag. In figure 4.3, the pink points on the left CMDs were selected in this manner. The selection has been intentionally slid into the sub-giant branch to highlight the point below.
4. Employ a color width: As is clear from the MSTO star selection in the figure, some sub-giant branch stars are also counted. To account for this, a color histogram (right plots of figure 4.3) was plotted, and all stars within  $2\sigma$  were

---

<sup>1</sup>all models which were fit to the CMDs were corrected for distance and reddening; both values mentioned in table 3.1

<sup>2</sup>Isochrone is a theoretical model which joins all points on the CMD with the same age.

selected (blue lines on the plot mark the  $\pm 2\sigma$  respectively). The color width was 1.34 mag.

5. Division into two bins: The rectangle drawn out of such magnitude and color width was divided into two bins and will be referred to as the *upper bin* and the *lower bin* further. This was done to constrain the dependence on the adopted MSTO sample.
6. Generalizing the technique: The varying mass, choice of CMD, and  $P_\mu$  were varied as discussed below, making this technique more general and less input physics dependent. Table 4.1 gives all the star counts.
  - (a) Varying Mass: The varying mass value was taken to be 0.0035 and 0.0040  $M_\odot$ , other than 0.0030, to constrain the dependence on the sample.
  - (b)  $P_\mu$  Cut: As shown in figures 3.7 and 3.8, the total number of objects on the CMD does not differ by a huge margin when 60 % and 80 % membership cut is applied. Hence,  $P_\mu$  cuts of 60 % and 95 % were employed to constrain the dependence on the sample.
  - (c) CMD selection: Both 336CMD and 438CMD were used. This will be clear once ratios of different evolutionary phases are compared.

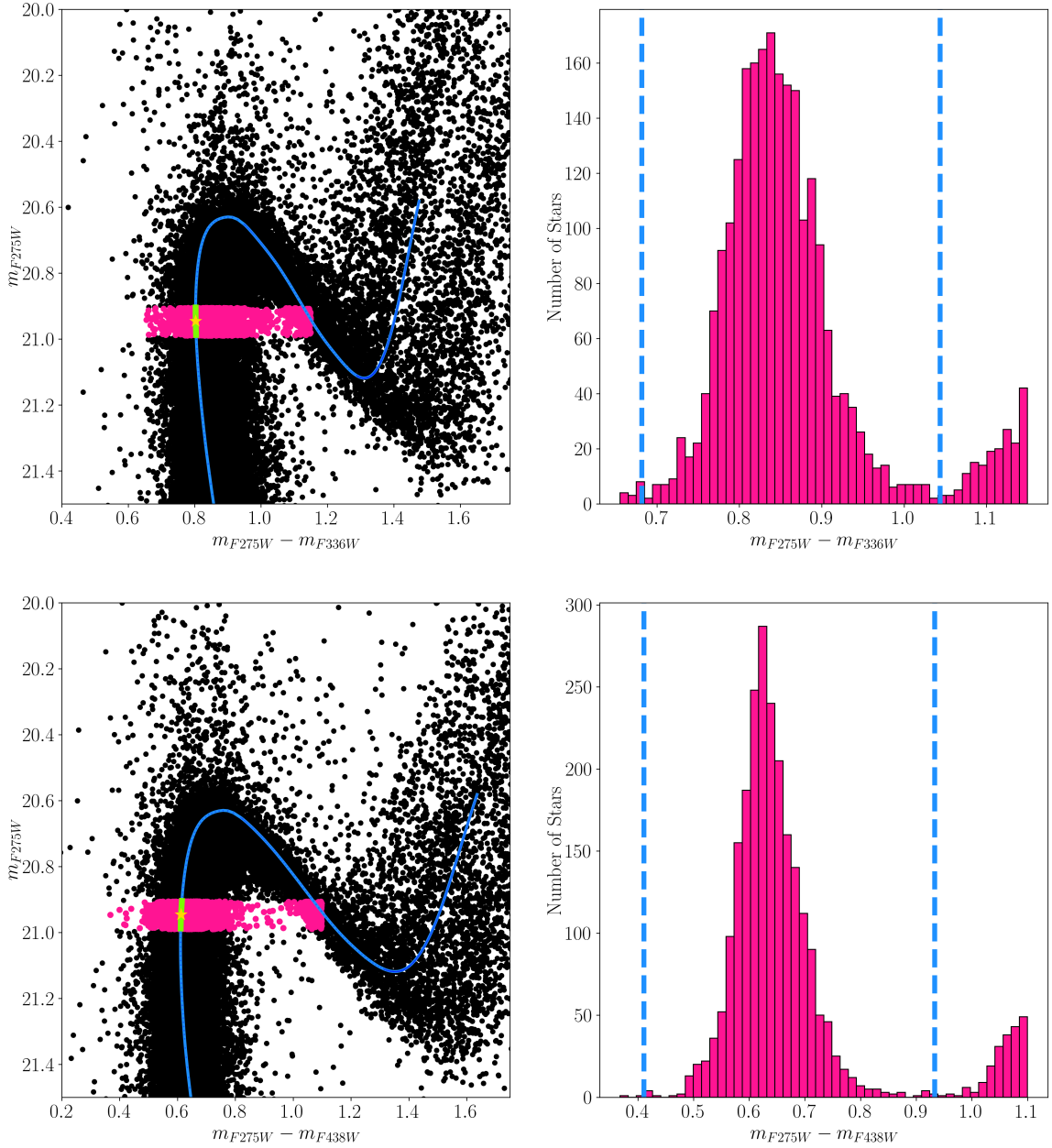


Figure 4.3: Left plot are the 336CMD and 438CMD from top to bottom respectively, with a  $P_\mu \geq 60\%$  cut. The blue curve is a 10.9 Gyr isochrone. The objects in pink lie between  $0.82 \pm 0.0030 M_\odot$ . The lime green region has been highlighted since this is the varying mass region, i.e., mass corresponding to these points lies between  $0.82 \pm 0.0030 M_\odot$ . The golden-colored star is the theoretical MSTO point on the CMD, better visible in the figure 4.4. The right plots are color histograms of the pink objects in the respective CMDs. All objects in  $2\sigma$  of the highest point on the histogram were considered MSTO stars.

7. Crossing Times: To calculate the crossing time across the magnitude bin for a star of mass  $0.82 M_{\odot}$ , an evolutionary track<sup>3</sup> of  $0.82 M_{\odot}$  from the BaSTI dataset was plotted. The corresponding magnitude limits of the bins were found on the evolutionary track, the corresponding time of which was then calculated from the evolutionary track table data. Crossing times corresponding to different counts is given in table 4.1.
8. Since the magnitude bin sizes were small, accounting for MSTO was straightforward. The  $\Phi_{\text{MS-RGB}}$  was used to count the completeness in a given magnitude bin as the difference of  $\Phi_{\text{MS-RGB}}$  at the lower magnitude bin limit and upper magnitude bin limit.

Varying Mass ( $M_{\odot}$ )	CMD	Bin	Star Counts		Crossing Time (Myrs)
			60%	95%	
0.0030	336	Upper	1398	1245	202.49
		Lower	1456	1241	283.68
	438	Upper	1416	1259	202.49
		Lower	1472	1254	283.68
0.0035	336	Upper	1867	1664	283.45
		Lower	1871	1608	364.77
	438	Upper	1880	1673	283.45
		Lower	1885	1619	364.77
0.0040	336	Upper	2367	2108	364.40
		Lower	2293	1967	422.11
	438	Upper	2376	2117	364.40
		Lower	2315	1985	422.11

Table 4.1: Counts and crossing times of MSTO stars for various varying mass values in the 336CMD and 438CMD with probability membership cut of 60% & 95% have been presented. Note that these star counts are accounted for completeness.

---

<sup>3</sup>a model which joins all those points which a particular mass star goes through in its lifetime.

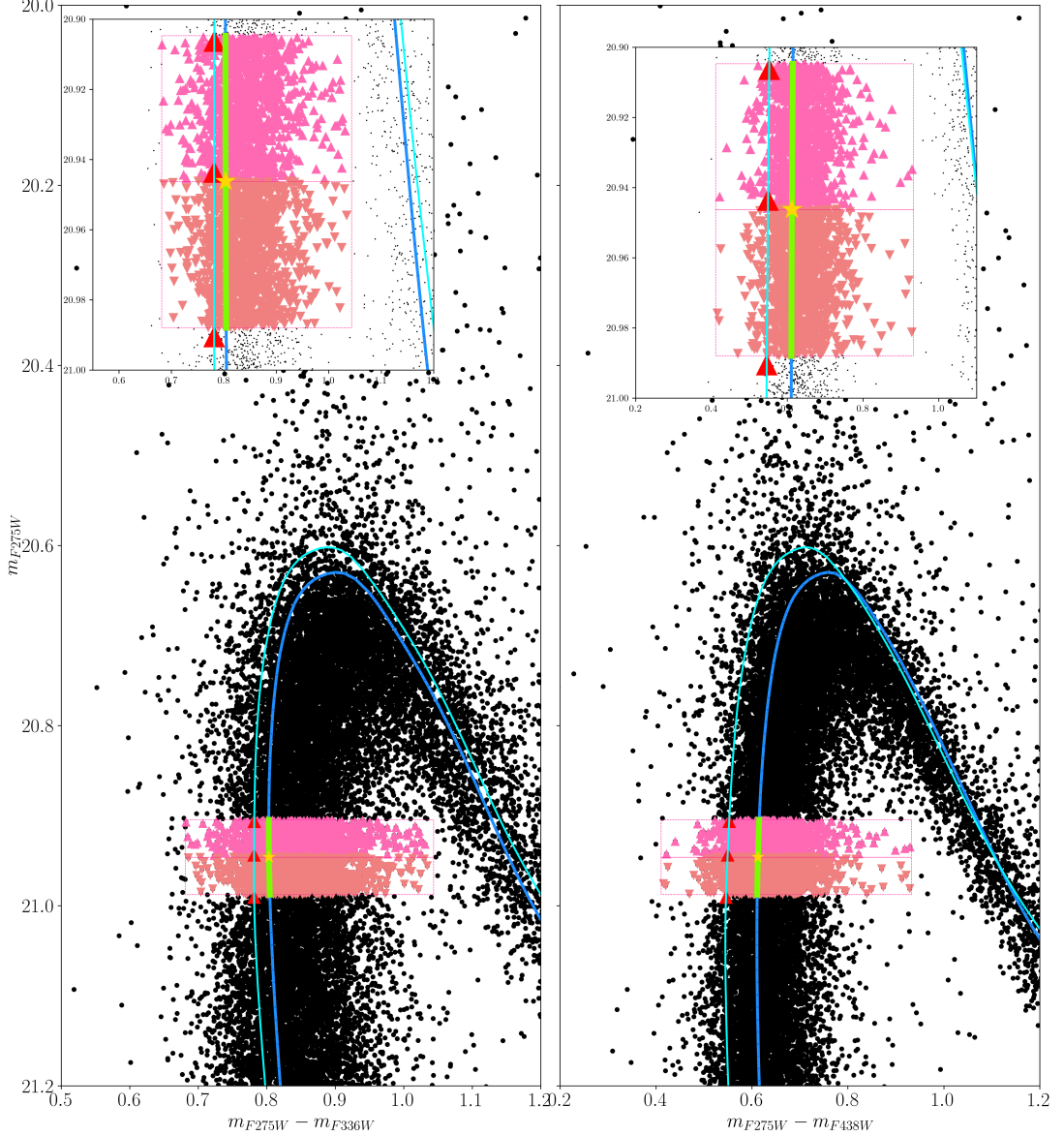


Figure 4.4: Plotted are two CMDs, cleaned with a  $P_\mu \geq 60\%$  cut. In the left panel is the 336CMD. The blue and cyan lines represent the 10.9 Gyr isochrone and evolutionary track of mass  $0.82 M_\odot$ , respectively. The lime-green line on the CMD is the part on the isochrone where the mass is  $0.82 \pm 0.0030 M_\odot$ . A gold-colored star (better visible in the inset plot) is the theoretical MSTO derived from the isochrone. The light-pink (1086 and 1100 star counts in the 336CMD and 438CMD, respectively) and coral-brown (1129 and 1141 star counts in the 336CMD and 438CMD, respectively) triangles are the *upper bin* and *lower bin* stars, respectively. These have been zoomed into and are presented in the inset plot. Overplotted on the evolutionary track (red-colored) are three teal-colored triangles denoting the corresponding magnitude limits on the evolutionary track. The right panel has the 438CMD with the same analysis. For completeness corrected star counts and corresponding lifetimes refer to the 0.0030 rows of table 4.1 for this plot.

### 4.2.2 Red Giant Branch Stars

The method to count red giant branch (RGB) stars and the calculations of the corresponding crossing times have been elaborated upon in the following points.

1. The evolutionary track of mass, the same as of the MSTO ( $0.82 M_{\odot}$ ), was plotted (see figure 4.5).
2. From the [BaSTI webpage](#), the theoretical foot of the RGB point was noted, which was found to be 490<sup>th</sup> point of the dataset. The tip of the RGB was found to be at the 1290<sup>th</sup> point of the dataset. RGB phase has been highlighted as the thick blue curve on the CMD in figure 4.5.
3. A vertical line was drawn from the theoretical foot of the RGB, and all the points redder than this were selected for further analysis.
4. To select the RGB stars from this selection, luminosity function was plotted for these selected stars (see figure 4.5). A dip in number of stars is seen at  $\sim 19.4$  mag and  $\sim 21.4$  mag. All objects within this magnitude range from the selection are the RGB stars (see figure 4.6). This could be considered as the brighter and the fainter ends of the RGB.
5. Crossing time for RGB was the time at the foot of the RGB and the tip of the RGB on the CMDs (see figure 4.6).

CMD	Star Counts		Crossing Time (in Myrs)
	60%	95%	
336	6234	5583	538.62
438	6402	5723	538.62

Table 4.2: Counts and crossing times of RGB stars in the 336CMD and 438CMD with probability membership cut of 60% & 95% have been presented. Note that these star counts are accounted for completeness.

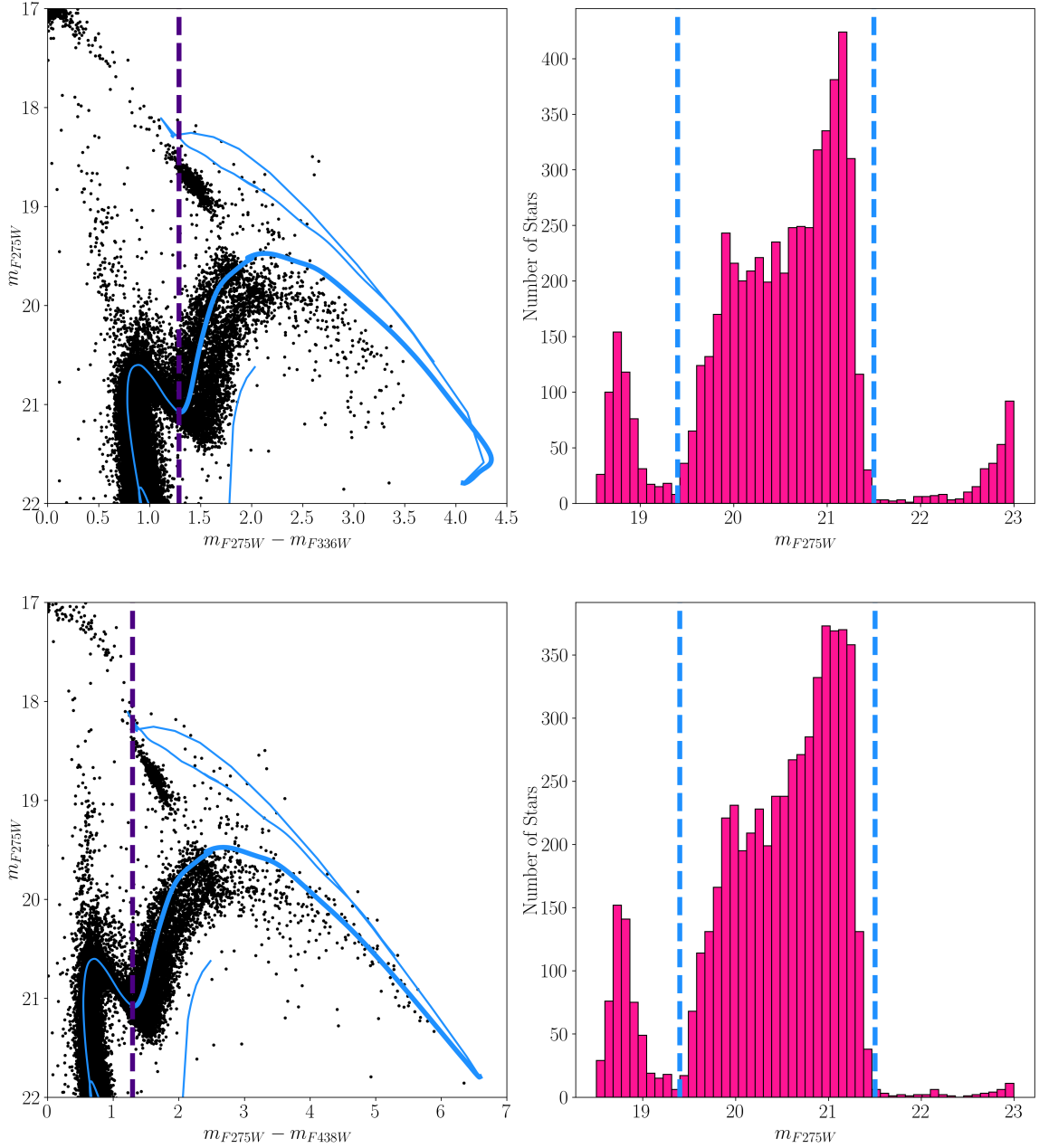


Figure 4.5: Both CMDs (left plots) have been cleaned with a  $P_\mu \geq 60\%$  cut. They are the 336CMD and 438CMD from top to bottom respectively. The blue curve is a 10.9 Gyr isochrone. The curve is thicker from the 490<sup>th</sup> to the 1290<sup>th</sup> point (see text for detail). The purple vertical dashed line goes through the theoretical foot of the RGB (see text for detail). The right plots are color histograms of objects from 18 to 23 mag in the respective CMDs. All objects between 19.4 and 21.4 color values on the histogram were considered RGB stars since a “dip” is seen at these values.

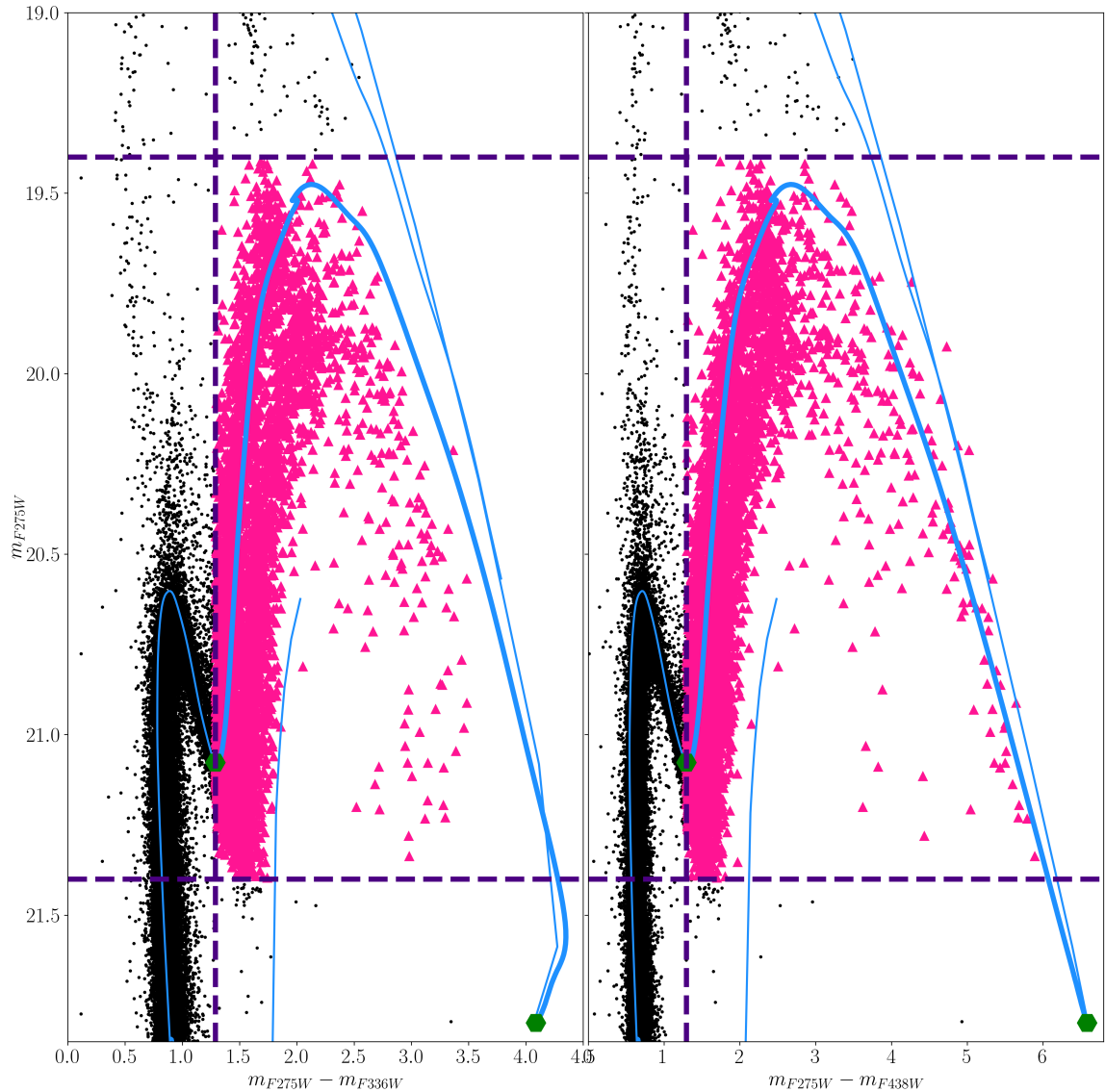


Figure 4.6: Plotted are two CMDs, cleaned with a  $P_\mu \geq 60\%$  cut. In the left panel is the 336CMD. The blue curve is the same as in figure 4.5. The purple dashed lines were drawn to select RGB stars highlighted in pink (4895 objects in 336CMD and 5027 objects in 438CMD; note that these are not completeness corrected counts.). The green-colored hexagon is the point corresponding to which time was calculated. The right panel has the 438CMD with the same analysis, not completeness corrected. For star counts and corresponding lifetimes, refer to the 60% column of table 4.2.

### Accounting for completeness

Accounting for completeness for the RGB stars was done in the following way. The CMD was binned in magnitude with bin size 0.35. Then, the lower and upper bin value

for a particular magnitude bin was used to calculate the value of the  $\Phi_{\text{MS-RGB}}$  function at those points, and the difference was taken. The same procedure was repeated for all bins. Figure 4.7 presents the completeness corrected luminosity function (magnitude histograms).

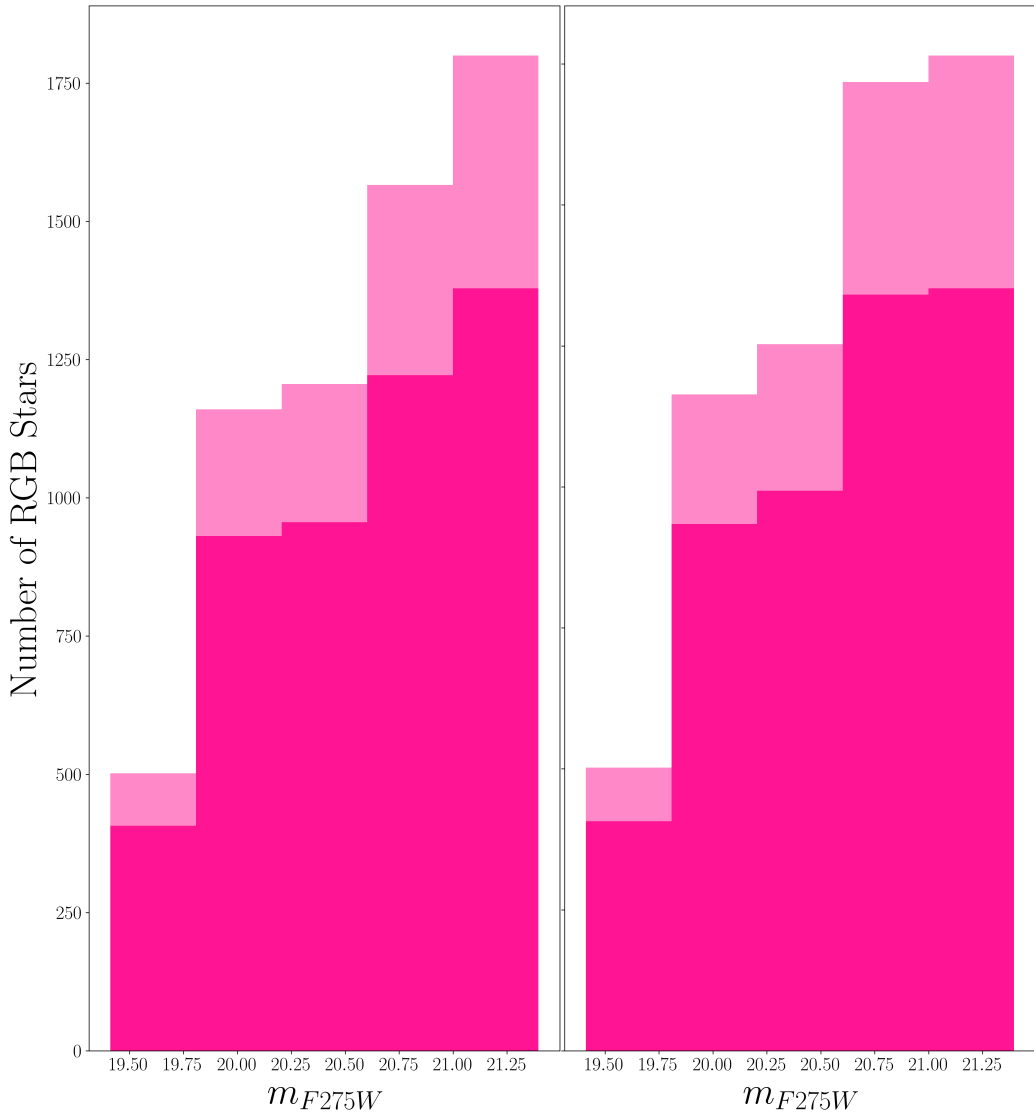


Figure 4.7: The plots are the luminosity functions of RGBs as selected by the method elaborated above. The left plot corresponds to the 336CMD, whereas the right one corresponds to the 438CMD. The dark pink-colored bars are without completeness accountability (for 336CMD, the cumulative star count is 4895; for 438CMD, the cumulative star count is 5027). In contrast, the light pink bars are completeness accounted counts (for 336CMD, the cumulative star count is 6234; for 438CMD, the cumulative star count is 6402). The completeness corrected counts are given in table 4.2.

### 4.2.3 WD Stars

#### Cleaning Criterion for WDs

In section 3.2, it was discussed why the probability membership cuts are an unsuitable choice for cleaning CMD for faint objects and WDs being faint, using quality parameters (except the q-param) to clean the CMD was decided.

The d-param cut was kept to be 1/3 for F275W and F336W filters, whereas for F438W, it was 1/2. The s-param cut was kept to be  $\pm 0.5$  for all the three filters. This has been summarized in table 4.3. Since plotting a CMD requires two filters, the common stars in the four sub-datasets (2 for each filter) were finally used to plot the CMD. These have been presented in figure 4.8. A clean and distinct WD sequence is obtained in both the CMDs; hence, the WD selection was made visually.

	336CMD		438CMD	
	F275W	F336W	F275W	F438W
d-param	$\leq 1/3$	$\leq 1/3$	$\leq 1/3$	$\leq 1/2$
s-param	$\pm 0.5$	$\pm 0.5$	$\pm 0.5$	$\pm 0.5$

Table 4.3: Summary of the d-param and s-param values for the 336CMD and 438CMD.

#### Star Counts

In the 336CMD and 438CMD, without completeness correction, the count is 122 and 48 WDs, respectively (see figure 4.8, pink and teal colored stars). However, particular attention was focused on inculcating the completeness of these numbers. This is because the AST results for WDs start at 21 mag (see figure 4.2), and therefore, star counts fainter than 21 mag can only be completeness corrected. Hence, for 336CMD and 438CMD, 113 and 42 stars were used to build the WD luminosity functions (WDLFs), which have been presented in figure 4.9 (only pink-colored stars). The counts after completeness correction in 336CMD and 438CMD were 176 and 64, respectively. Finally, when the WDs brighter than 21 mag were included, the count increased to 185 and 72 in the 336CMD and 438CMD, respectively.

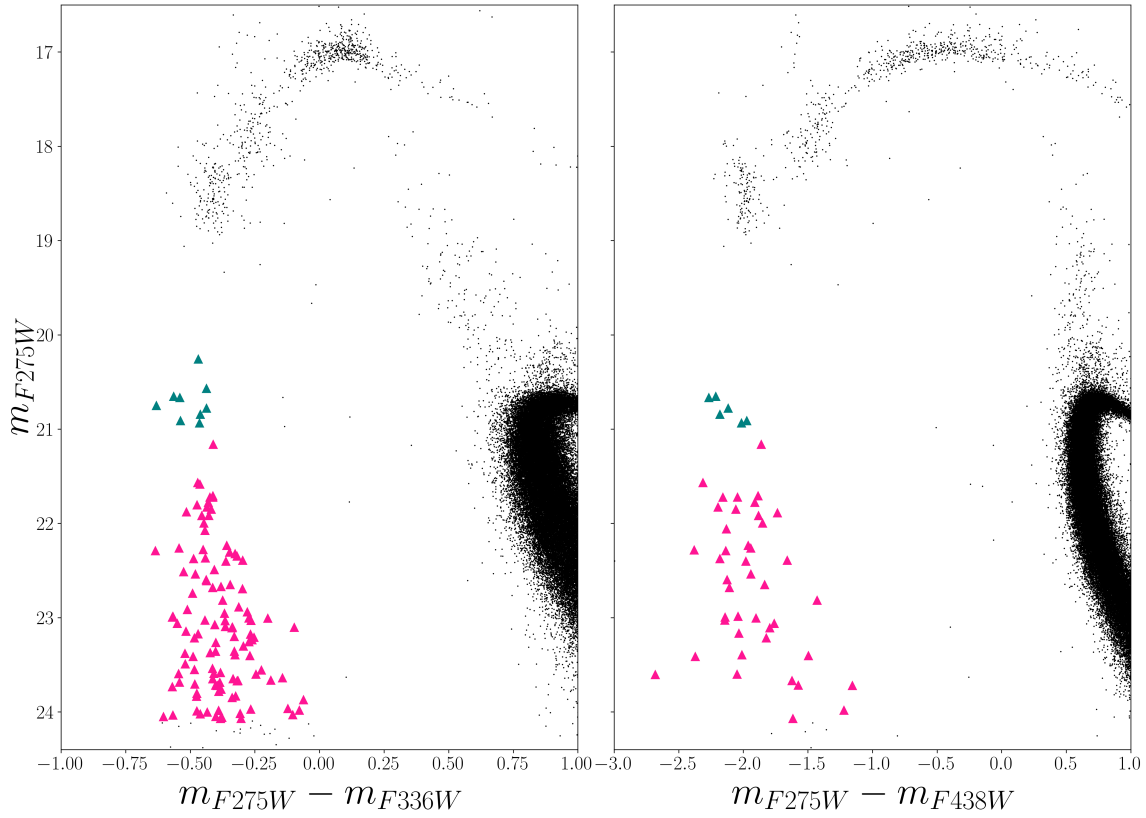


Figure 4.8: The CMDs were cleaned as discussed in the text above. The left plot is the 336CMD, where all stars in triangles are WDs. Teal-colored triangles are WDs brighter than 21 mag, whereas pink triangles are fainter than that. This distinction was made to explain completeness counts. The right plot is 438CMD with the understanding.

### Crossing Times

To find the crossing times, 75 different WD cooling models from the [BaSTI dataset](#) were plotted (see figure 4.10), but unfortunately only 20 were retained (see figure 4.11) since not all models spanned the same area on the CMD as the WDs. The crossing time was calculated in the same manner as for the MSTO and RGB stars. The magnitude of the brightest WD (including the teal-colored ones) and the faintest WD were selected to find the corresponding points on the WD cooling models (top-most teal-colored and bottom-most pink-colored triangle, see figure 4.8). Crossing times from the 20 models have been summarised in table 4.4 (which are also given in the same order in the legend in figure 4.11).

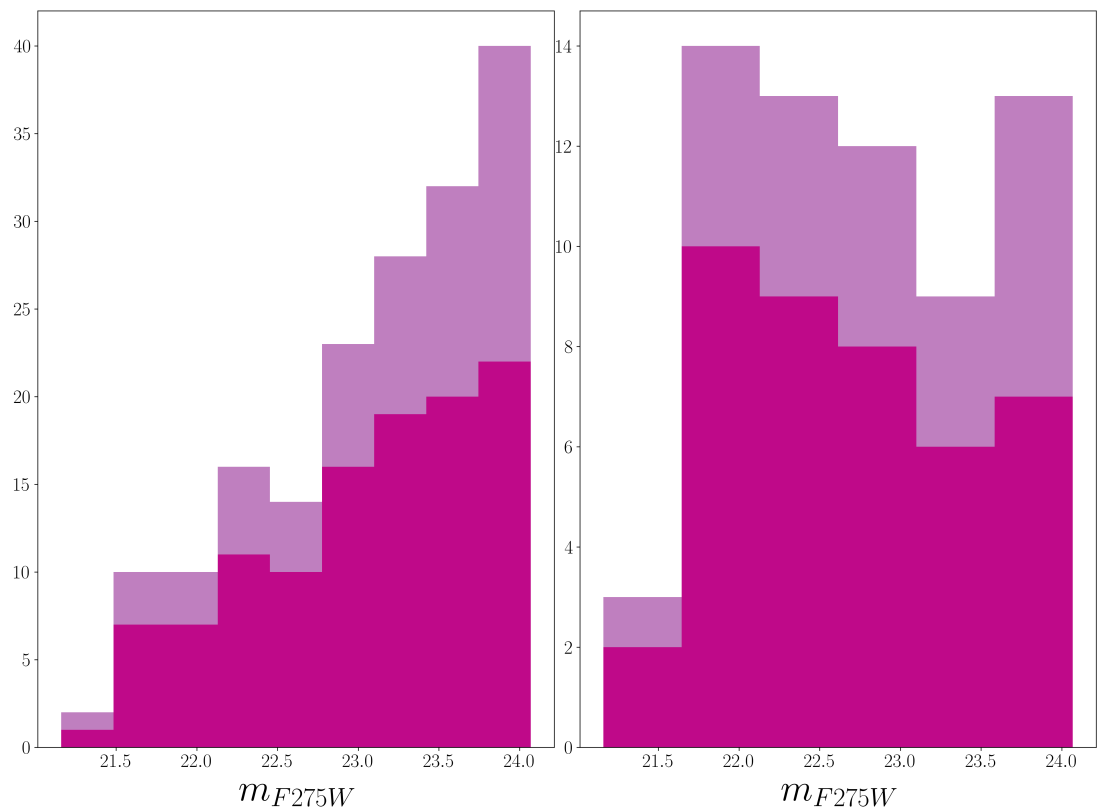


Figure 4.9: Plots are WD luminosity functions of 336CMD and 438CMD from left to right. The dark pink is the observed data number, whereas the light pink is the corrected completeness (see text for counts).

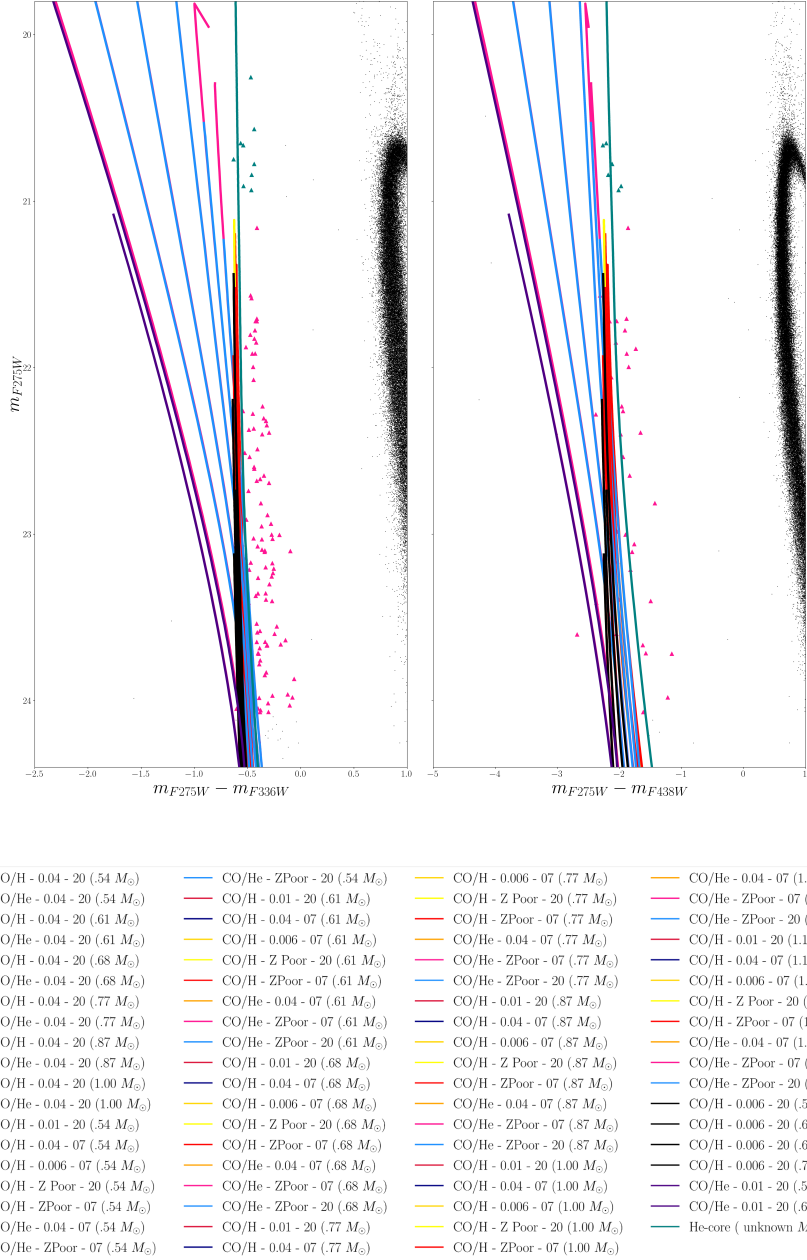


Figure 4.10: To understand the different parameters of each model which the legend contains first the core of the WD model is written (say CO-core), then followed by a “/” is the envelope type of the model (say He) followed by a “-” and metallicity of the model (say 0.04), followed by another model parameter, called the electron conduction opacity. “20” (Blouin et al. (2020)) or “7” (Cassisi et al. (2007)) are the choices for the same, which refer to the year of the paper from which they were adopted to generate these plots by BaSTI (see (Pietrinferni et al. 2021) and (Salaris et al. 2022)). Then, in brackets is the mass of the WD model. For figure 4.11, the corresponding crossing is also given following the mass. These 20 models are given model numbers, which will be used to find ratios in the next section.

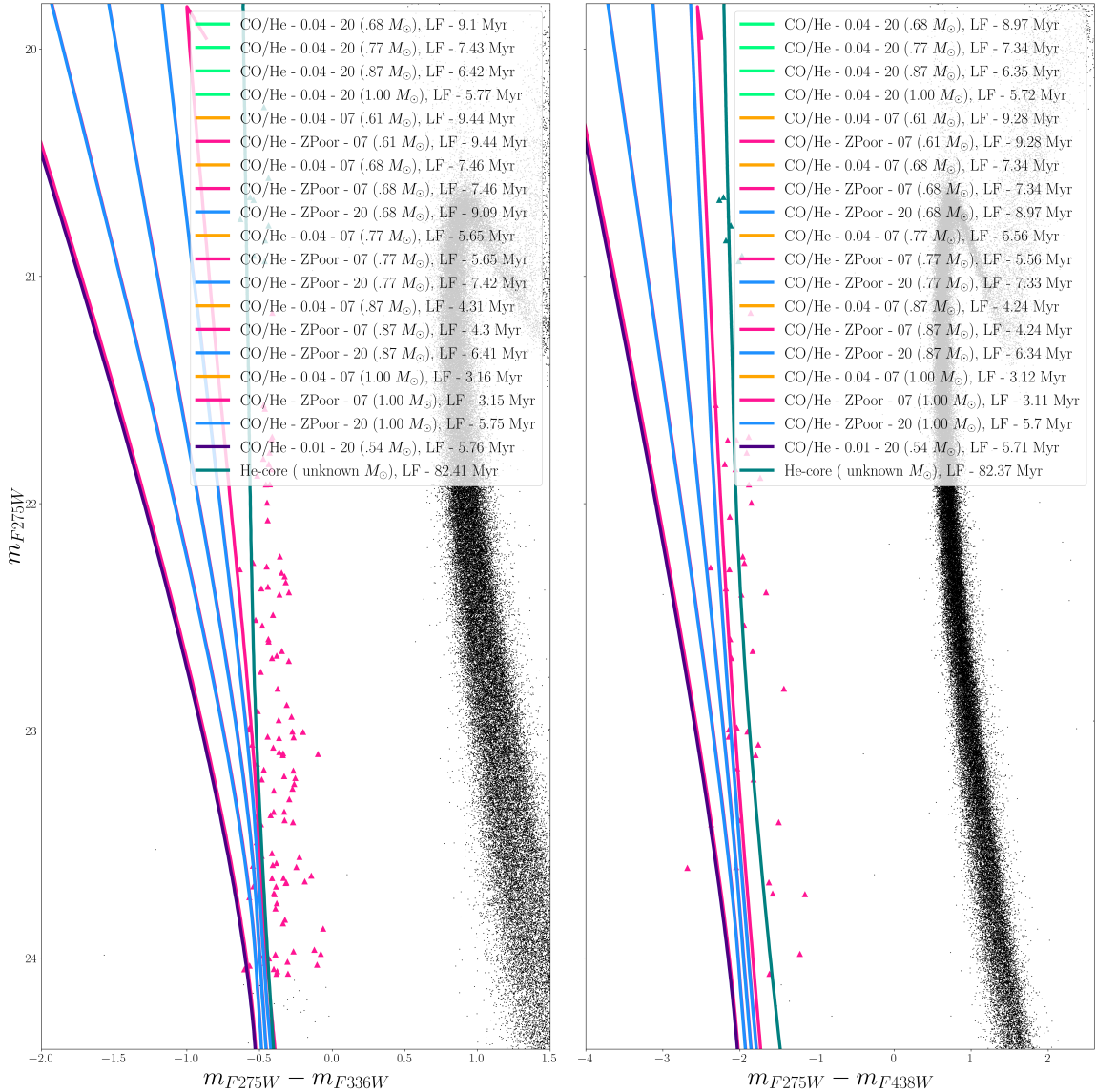


Figure 4.11: 336CMD and 438CMD with those models for which crossing time could be found for both CMDs. Pink and teal-colored triangles are the same stars as in previous plots.

Model No.	Core	Envelope	Metallicity	Opacity	WD Mass	Crossing Time (Myrs)	
						336CMD	438CMD
1	CO	He	0.04	20	0.68	9.10	8.97
2	CO	He	0.04	20	0.77	7.43	7.34
3	CO	He	0.04	20	0.87	6.42	6.35
4	CO	He	0.04	20	1.00	5.77	5.72
5	CO	He	0.04	07	0.61	9.44	9.28
6	CO	He	ZPoor	07	0.61	9.44	9.28
7	CO	He	0.04	07	0.68	7.46	7.34
8	CO	He	ZPoor	07	0.68	7.46	7.34
9	CO	He	ZPoor	20	0.68	9.09	8.97
10	CO	He	0.04	07	0.77	5.65	5.56
11	CO	He	ZPoor	07	0.77	5.65	5.56
12	CO	He	ZPoor	20	0.77	7.42	7.33
13	CO	He	0.04	07	0.87	4.31	4.24
14	CO	He	ZPoor	07	0.87	4.30	4.24
15	CO	He	ZPoor	20	0.87	6.41	6.34
16	CO	He	0.04	07	1.00	3.16	3.12
17	CO	He	ZPoor	07	1.00	3.15	3.11
18	CO	He	ZPoor	20	1.00	5.75	5.70
19	CO	He	0.01	20	0.54	5.76	5.71
20	He	H	*	*	*	82.41	82.37

Table 4.4: Crossing Times of Various WD Cooling Models. ZPoor refers to metallicity values < 0.01. '\*' parameters are to be taken from literature

#### 4.2.4 Horizontal Branch Stars

Horizontal branch (HB) stars were counted (see table 4.5) via manual selection (highlighted in blue in figure 4.12) on both 336CMD and 438CMD. First, the CMDs were cleaned using a  $P_\mu \geq 60\%$  cut. Then, to confirm if these are real horizontal branch stars, they were plotted again on a “special” CMD proposed by Brown et al. (2016) since it makes only the HB stars pronounced. The match is reasonably well (see figure 4.12).

CMD	Star Count	
	60%	95%
336CMD	1229	1079
438CMD	1230	1079

Table 4.5: Star counts of HB stars in the 336CMD and 438CMD with probability membership cut of 60% & 95% have been presented. Note that these star counts are not completeness accounted for since the AST for these stars wasn’t performed.

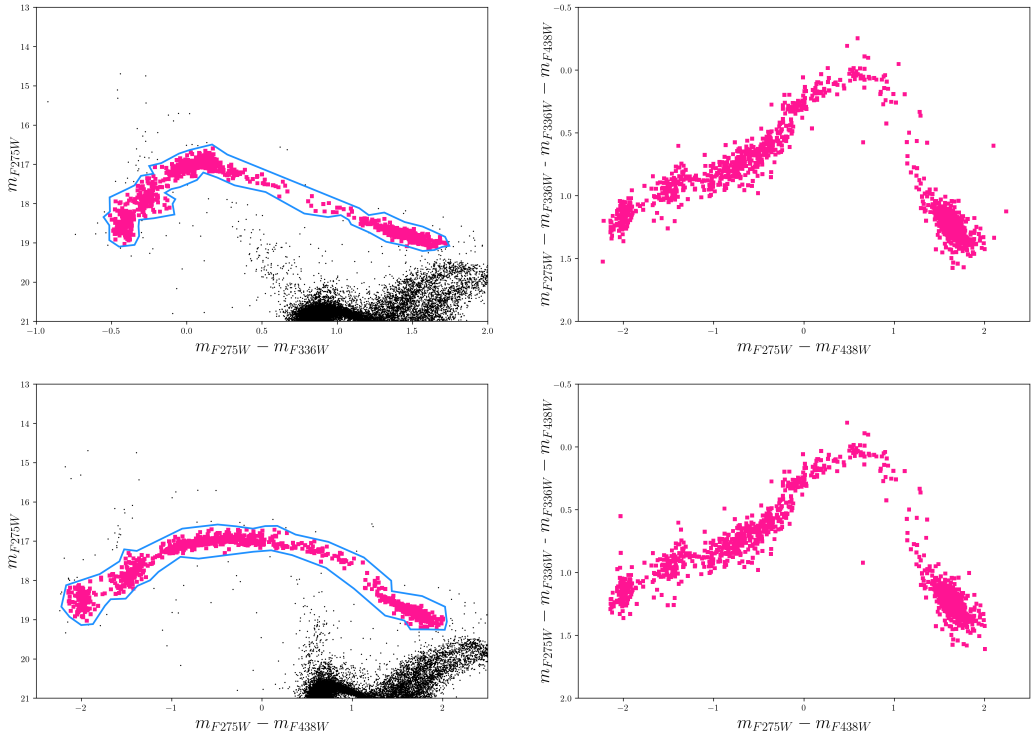


Figure 4.12: The left plots show 336CMD and 438CMD from top to bottom respectively. The blue cutout is the manual selection made to select the HB stars. On the right are the pink stars from 336CMD and 438CMD plotted to check if they belong to the horizontal branch.

## 4.3 Ratios

Since AST for HB was not available, these stars were not inculcated in calculating ratios. Hence, the  $N_{\text{Obsv}}$  and  $\tau_{\text{Theo}}$  for 3 pairs of evolutionary phases are compared, i.e., MSTO-RGB, WD-RGB, and WD-MSTO.

### 4.3.1 MSTO:RGB

From tables 4.1 and 4.2,  $N_{\text{Obsv}}$  and  $\tau_{\text{Theo}}$  were calculated for MSTO and RGB stars. Since two different CMDs and two different cleaning criteria were used to calculate the star counts for both the RGB and MSTO stars,  $N_{\text{Obsv}}$  is obtained as four sets of observed ratios. The  $\tau_{\text{Theo}}$  remains the same for all the four sets. These have been presented below. Hence, for MSTO-RGB, 4 observed ratios were calculated with the same theoretical ratio (see table 4.6 row-wise).

Ratio Number	336CMD/60%	336CMD/95%	438CMD/60%	438CMD/95%	$\tau_{\text{Theo}}$
	$N_{\text{Obsv}}$				
1	0.224	0.223	0.221	0.220	0.376
2	0.234	0.222	0.230	0.219	0.527
3	0.299	0.298	0.294	0.292	0.526
4	0.300	0.288	0.294	0.283	0.677
5	0.380	0.378	0.371	0.370	0.677
6	0.368	0.352	0.362	0.347	0.784

Table 4.6: 4 sets of  $N_{\text{Obsv}}$  and the corresponding  $\tau_{\text{Theo}}$  values have been presented. Note that all these ratios are  $\frac{\text{MSTO}}{\text{RGB}}$ .

### 4.3.2 WD:RGB

From tables 4.2 and 4.4,  $N_{\text{Obsv}}$  and  $\tau_{\text{Theo}}$  were calculated for RGB and WD stars. Since two different CMDs and two different cleaning criteria were used to calculate the star counts for RGB, whereas, for WDs, only singular criteria were used,  $N_{\text{Obsv}}$  is obtained as 4 different ratios presented in table 4.7. For example, from the 438CMD, 72 WDs were calculated. This number was compared to the RGB count of 438CMD with  $P_\mu \geq 60\%$  and to the RGB count of 438CMD with  $P_\mu \geq 95\%$ , resulting in two

ratios. Hence, if one includes 336CMD comparisons too, four ratios were found and presented in table 4.7. The  $\tau_{\text{Theo}}$  was calculated for all 20 WD cooling models (see table 4.4 for crossing times). These have been presented in table 4.8.

	336CMD	438CMD
60%	0.030	0.011
95%	0.033	0.013

Table 4.7:  $\frac{\text{WD}}{\text{RGB}} N_{\text{Obsv}}$  (observed) values

Model Number	336CMD	438CMD
1	0.017	0.017
2	0.014	0.014
3	0.012	0.012
4	0.011	0.011
5	0.018	0.017
6	0.018	0.017
7	0.014	0.014
8	0.014	0.014
9	0.017	0.017
10	0.010	0.010
11	0.010	0.010
12	0.014	0.014
13	0.008	0.008
14	0.008	0.008
15	0.012	0.012
16	0.006	0.006
17	0.006	0.006
18	0.011	0.011
19	0.011	0.011
20	0.153	0.153

Table 4.8:  $\frac{\text{WD}}{\text{RGB}} \tau_{\text{Theo}}$  (theoretical) values

### 4.3.3 WD:MSTO

From tables 4.1 and 4.4,  $N_{\text{Obsv}}$  and  $\tau_{\text{Theo}}$  were calculated for MSTO and WD stars. Since two different bins, two different CMDs, and 3 different varying mass values were used to count the MSTO stars, an average of star counts and corresponding crossing times was taken for a particular bin in each CMD across the varying mass values.

To elaborate on this; the average of all *upper bin* star counts from the 336CMD

	Bin	336CMD	438CMD
60%	Upper	0.099	0.038
	Lower	0.099	0.038
95%	Upper	0.111	0.043
	Lower	0.115	0.044

Table 4.9:  $\frac{\text{WD}}{\text{MSTO}}$   $N_{\text{Obsv}}$  values

Model Number	336		438	
	Upper	Lower	Upper	Lower
1	0.032	0.026	0.032	0.025
2	0.026	0.021	0.026	0.021
3	0.023	0.018	0.022	0.018
4	0.020	0.016	0.020	0.016
5	0.033	0.026	0.033	0.026
6	0.033	0.026	0.033	0.026
7	0.026	0.021	0.026	0.021
8	0.026	0.021	0.026	0.021
9	0.032	0.025	0.032	0.025
10	0.020	0.016	0.020	0.016
11	0.020	0.016	0.020	0.016
12	0.026	0.021	0.026	0.021
13	0.015	0.012	0.015	0.012
14	0.015	0.012	0.015	0.012
15	0.023	0.018	0.022	0.018
16	0.011	0.009	0.011	0.009
17	0.011	0.009	0.011	0.009
18	0.020	0.016	0.020	0.016
19	0.020	0.016	0.020	0.016
20	0.291	0.231	0.291	0.231

Table 4.10:  $\frac{\text{WD}}{\text{MSTO}}$   $\tau_{\text{Theo}}$  values

with the same cleaning criterion (say,  $P_\mu \geq 60\%$ ) was taken. The same could be done for the 95% cleaning criterion (+1) and the *lower bins* (+2); hence, from a particular CMD, four star counts were calculated. Now, since WD counts were singular (for example, 185 for 336CMD), 4  $N_{\text{Obsv}}$  (observed) ratios were calculated from the 336CMD (see column 2, figure 4.9). Therefore, when including 438CMD too, the total  $N_{\text{Obsv}}$  (observed) ratios become 8 (see column 2, figure 4.9). For the  $\tau_{\text{Theo}}$  calculations, the table is similar to table 4.8 with the only difference that it now has 5 rows, 2 additional ones since MSTO stars were counted in two different (upper and lower) bins. These have been presented in table 4.10.

# Chapter 5

## Results and Discussions

In this chapter, the ratios which were calculated in the last section of the previous chapter will be discussed followed by a brief discussion on bimodality in the WD cooling sequence on the CMD. In the latter half of the chapter future scope of this work has been presented.

### 5.1 Ratios

1. For the MSTO-RGB ratios, it is seen that the numbers (observational and theoretical ratios, i.e.,  $N_{\text{Obsv}}$  and  $\tau_{\text{Theo}}$  respectively) do not match well. The discrepancy is almost 2 times (see figure 5.1). The  $N_{\text{Obsv}}$  are less than their corresponding  $\tau_{\text{Theo}}$  values. This implies that RGB stars are present in excess since the contrary would further decrease the  $N_{\text{Obsv}}$  value. This is expected in NGC2808 and has been previously studied ([Castellani et al. 2007](#)). However, NGC2808 has a deficiency of bright RGB stars ([Sandquist & Martel 2007](#)). This is thought to be the explanation of why this cluster has an extended HB, i.e., extensive mass loss events could have led the bright RGB stars to become EHB stars since the core was extensively exposed. This is intriguing as far as this study is concerned since missing bright RGB could also be progenitors of He-core WDs since mass loss could have occurred via mass transfer which is one of the formation scenarios of He-core WDs. Hence, with the current MSTO-RGB

ratios, it would be difficult to estimate the missing RGB number which could be linked to He-core WDs. A separate calculation of MSTO-RGB ratios must be done for the bright portions of the RGB to further comment on He-core WDs in this regard.

2. See figure 5.2 for a graphical view of how the WD-RGB ratios compare. It seems from the figure that ratios from the 438CMD (green and blue triangles) seem to match almost all models except the 20th model which is the only He-core white dwarf cooling model, whereas ratios from the 336CMD (red and pink triangles) do not match any model well. But both of them are far from the He-core model ratio (the ones in the top right, model number 20). This does suggest that the objects seen might not be He-core WDs. To make this argument stronger, one needs to plot more He-core WD models.
3. See figure 5.3 for a graphical view of how the WD-MSTO ratios compare. Again, it was seen that the He-core WD model ratios (top right) do not match the observational ratio (corresponding to the -1 and 0 on the x-axis). Additionally, the ratios from the 438CMD (green circles and blue stars) match much better than compared with 336CMD ratios (brown and black circles).

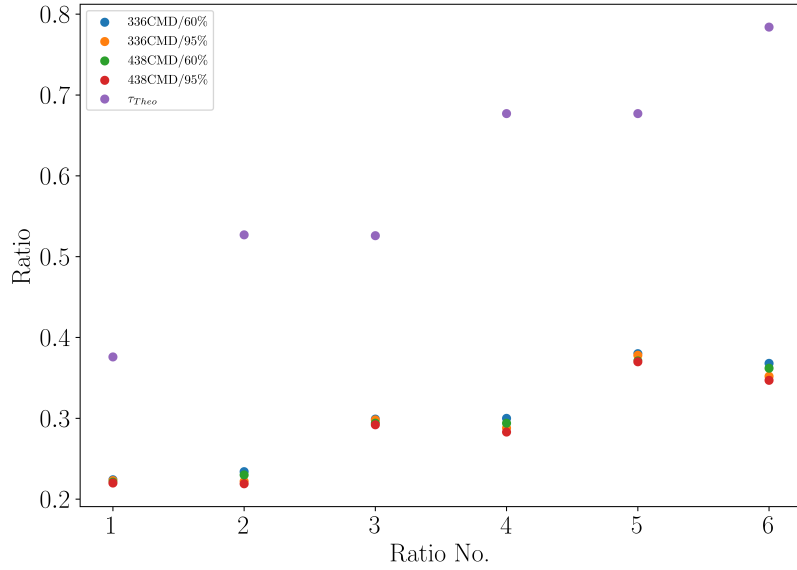


Figure 5.1: Values from the table 4.6 have been plotted. On the y-axis are the various  $N_{\text{Obsv}}$  (all colors circles except purple circles) and  $\tau_{\text{Theo}}$  (purple circles) values, whereas on the x-axis are the ratio number from table 4.6.

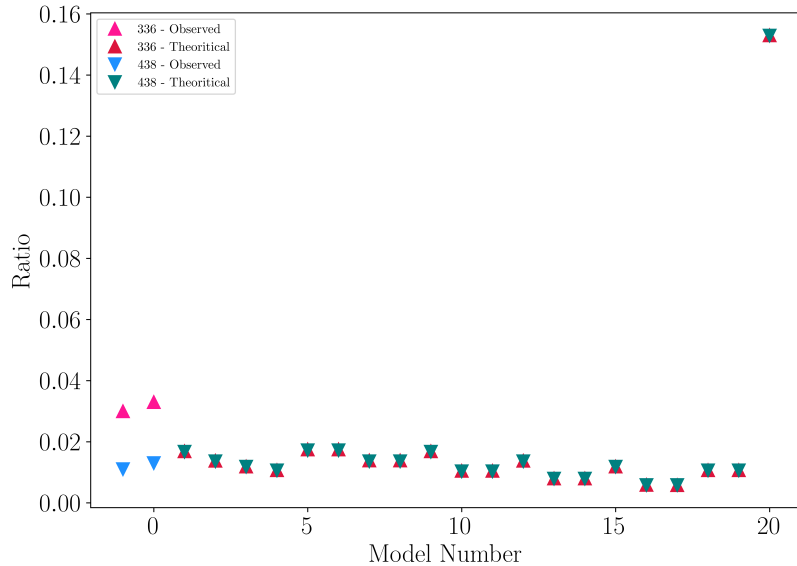


Figure 5.2: Values from the tables 4.7 and 4.8 have been plotted. “Observational” and “theoretical” in the legend mean  $N_{\text{Obsv}}$  (-1 and 0) and  $\tau_{\text{Theo}}$  (1 to 20) ratios respectively. In table 4.8, model number starts from 1 till 20, but in the above plot, the x-axis (model number) starts from -1; -1 and 0 are the  $N_{\text{Obsv}}$  values and do not indicate any model number whereas 1 to 20 are the  $\tau_{\text{Theo}}$  values from the table 4.8. The last model number corresponds to the He-core model and the others to the CO-core with different parameters.

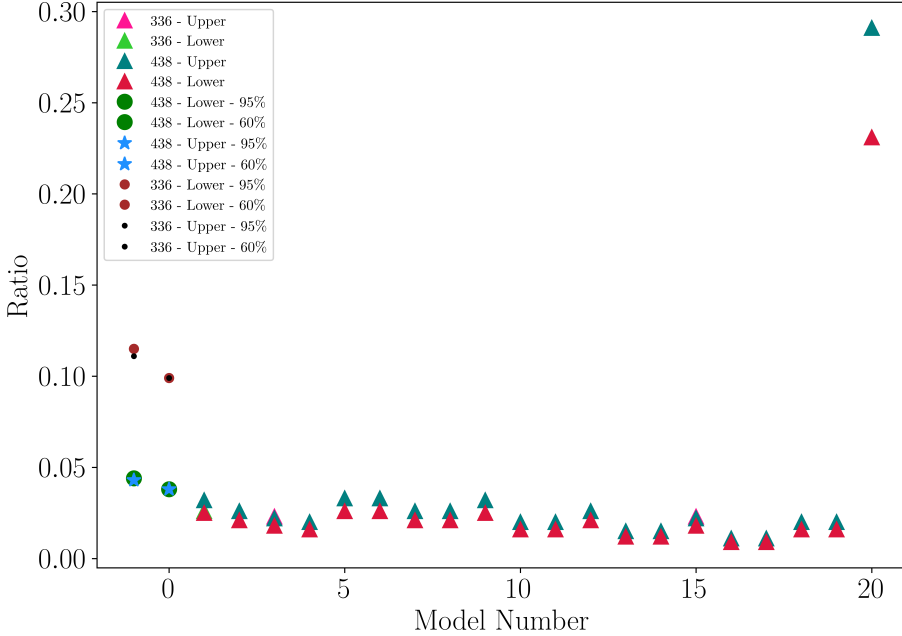


Figure 5.3: Values from the tables 4.9 and 4.10 have been plotted. -1 and 0 on the x-axis correspond to the same as in figure 5.2. Here also the last model number corresponds to the He-core model. Triangles are the various  $\tau_{\text{Theo}}$  ratios, whereas the circles and stars are the various  $N_{\text{Obsv}}$  values.

## 5.2 Bimodality in the White Dwarf Sequence

As mentioned in section 3.3, bimodality in the WD sequence could shed some light on the presence of He-core WDs. This is expected since CO-core WDs would be more hotter (hence bluer) than He-core ones. To find bimodality, first the WD sequence were straightened. This was done so that the spread could be contained only to one axis, which is the magnitude of stars. To straighten the WD sequence, stars were binned in magnitude, say 10 objects per bin, and the average color of objects in the bin was calculated, which was then subtracted from the color of each star. The resultant new color is called the straightened color; for corresponding plots see plot 5.4.

Next, histograms were plotted of the straightened sequences. Since 438CMD was very sparse, it was divided into two halves by in magnitude and color histograms were plotted. For 336CMD, three histograms were plotted. Following are the plots.

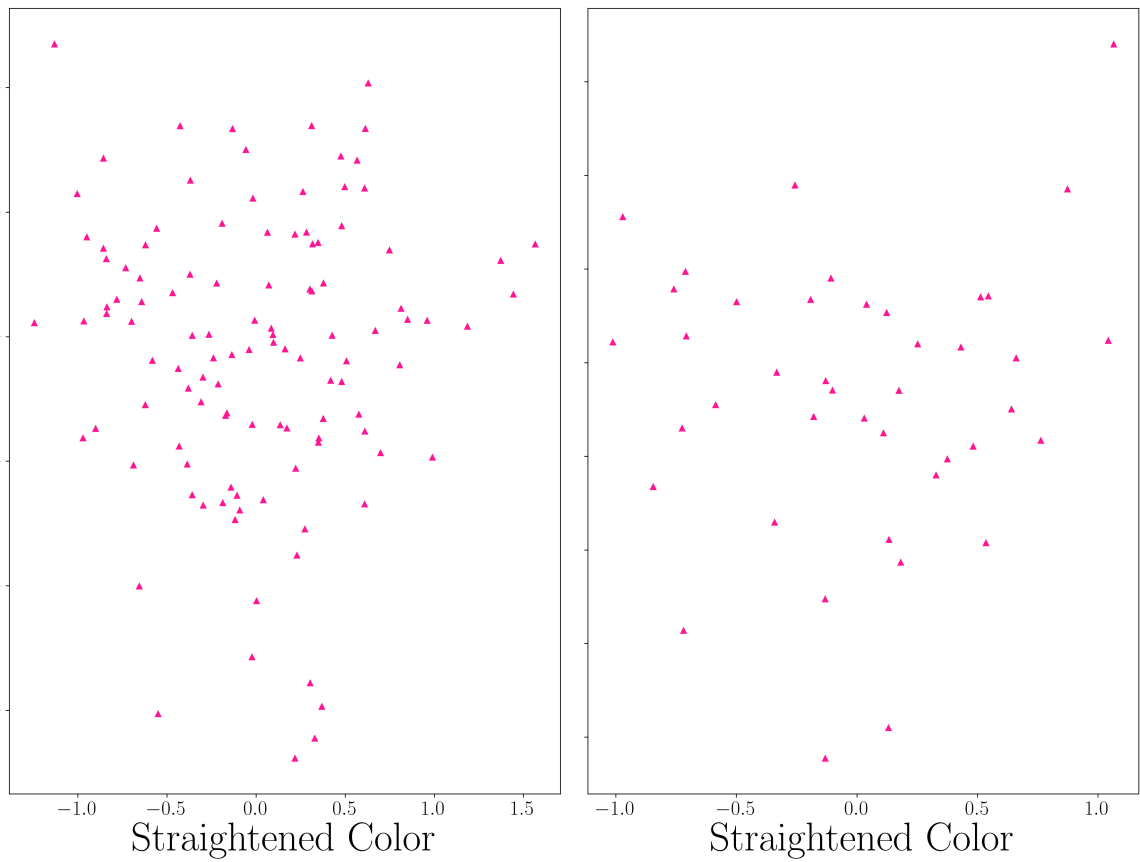


Figure 5.4: Straightened WD Sequence. The left plot corresponds to the 336CMD, whereas the right plot corresponds to the 438CMD.

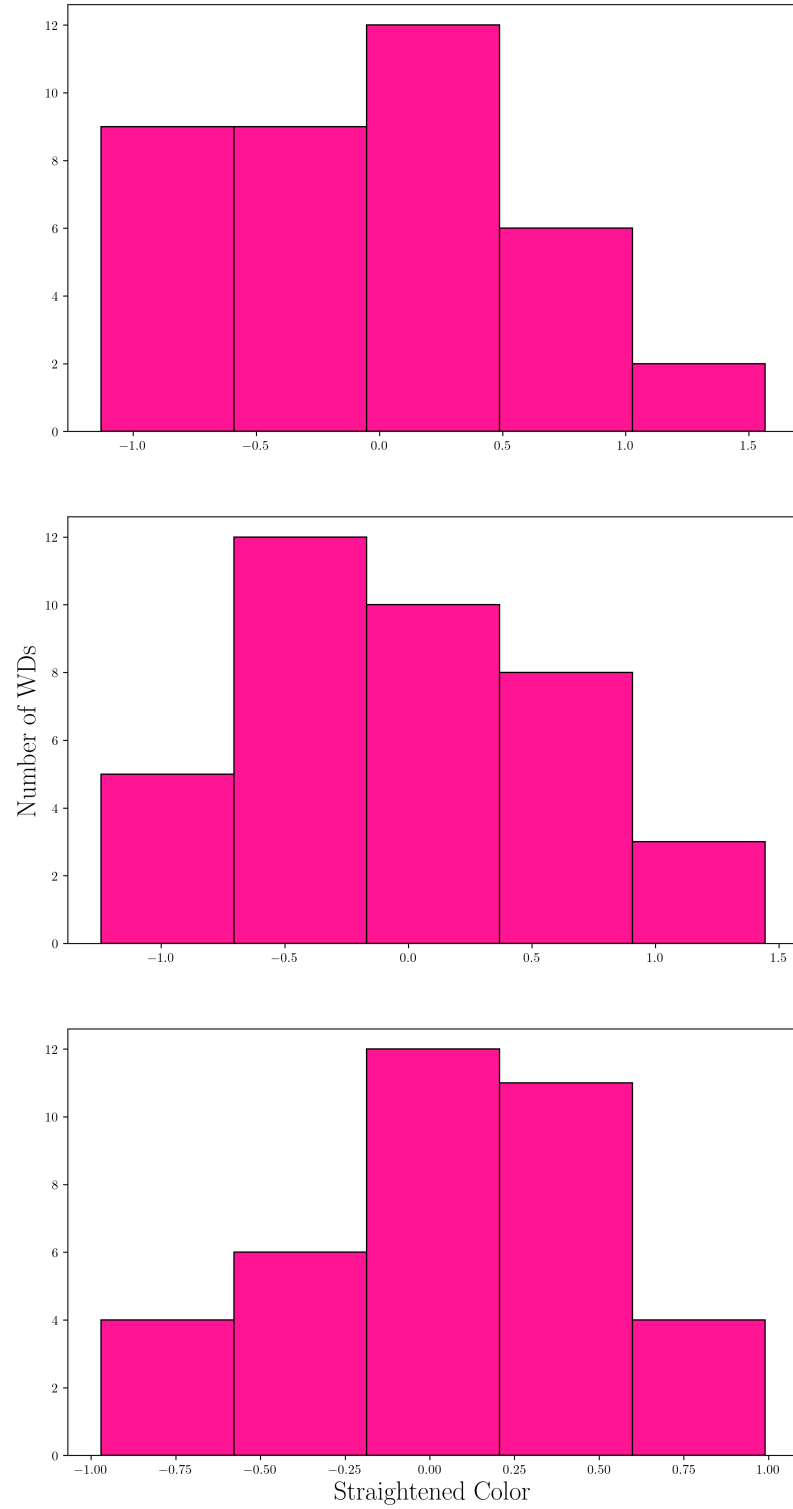


Figure 5.5: The 336CMD straightened WD sequence was divided into three halves and straightened color histogram for each case was plotted.

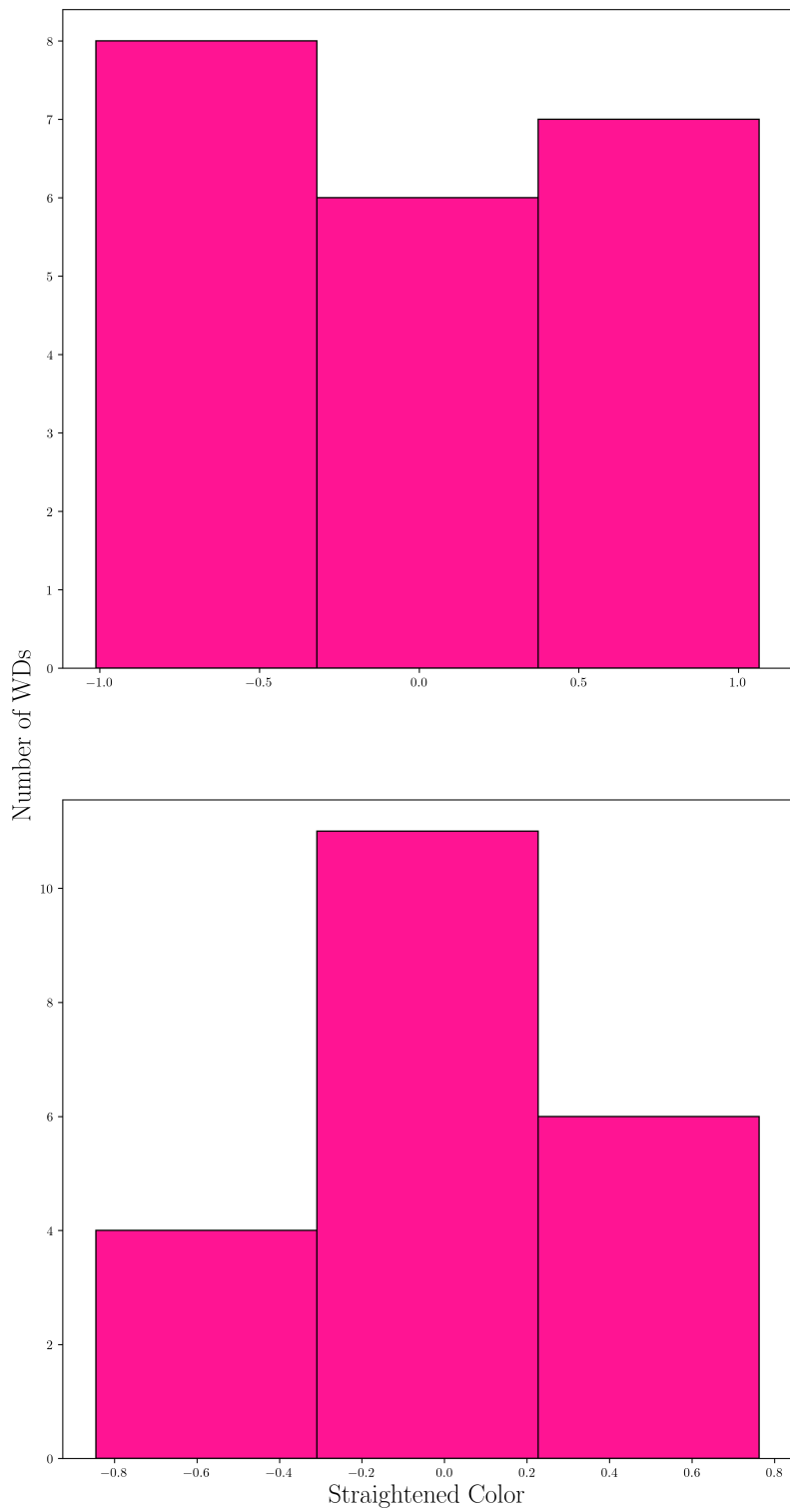


Figure 5.6: The 438CMD straightened WD sequence was divided into three halves and straightened color histogram for each case was plotted.

### 5.3 Conclusion

This study analysed the UV and optical CMDs of NGC2808 from the data fetched from the HUGS survey. The CMDs were cleaned systematically using d, q, and s quality parameters and probability membership to identify the cluster members. Various stellar evolutionary models and isochrones were fit to estimate the star counts and crossing times ratios of MS, RGB, and WD sequences (WD: MS, WD: RGB, and MS: RGB), which were systematically corrected using ASTs. The results suggest that the WD sequence primarily contains CO-core WDs since the observational and theoretical ratios match well. However, with the only He-core WD cooling model that was fit, it is suggestive that NGC2808 may not host He-core WDs. A bimodality analysis of the WD sequence (up to 24 magnitudes in UV) did not indicate any redder sequence corresponding to He-core WDs, as was discovered in Omega Centauri. This was contrary to our expectations since NGC2808 is a massive Globular Cluster. It is possible that the number of He-core WDs is smaller in fraction and mixed with the CO WD sequence or is fainter and redder than the limits analyzed in this study. Further studies, including fitting more He-core models and analyzing deeper photometric data NGC2808, could help conclude.

#### 5.3.1 Further Scope

1. The star counts could be made better by using more accurate techniques, such as fitting a fiducial to the entire CMD. A fiducial is an imaginary line that goes through the middle of a sequence, say the MS or the RGB. The benefit of using fiducials is that one can use fiducials to perform star counts without relying on theoretical models since relying on theoretical models for observational counts is not a good idea and defeats the idea of keeping the two sets of ratios (observational and theoretical) independent of each other. To elaborate more; after a fiducial is fit, say to the RGB, one could perform sigma cuts around the fiducial and count the stars then. This would be a better idea than selecting all of RGBs

as done in this study.

2. In section 4.2.3, 76 models were fit, but only 20 were as brighter as 21 mag in  $m_{F275W}$  out of which only one was He-core WD. More models, especially the He-core ones, are required to arrive at any conclusion. A single He-core model fails to justify, though the temptation is strong to suggest that NGC2808 holds no He-core WDs (seeing the difference in observed and predicted ratios (see figure 5.3)).
3. Careful error analysis must be done to understand the sensitivity of equation 4.2 and thereby of the conclusions made using this methodology.
4. Deeper photometry is required to reach the end of the WD sequence to see if a split in WD exists or not and also to provide a constraint to theoretical WD models.
5. To search for SCWDs Chen et al. (2021) used a technique in which the authors normalized the white dwarf luminosity function by the number of RGB stars in the GC. Hence, to use the same technique, the correct RGB counts must be found which could only be done decisively once better RGB counting techniques are employed.
6. Spectral Energy Distribution could be fit to the 21 mag brighter WDs since these could be objects that are proto-white dwarfs, less luminous Blue Hook Stars or cataclysmic variables.
7. Equation 4.2 is derived by Renzini & Fusi Pecci (1988) for simple stellar populations, but as is well known now, GCs host multiple stellar populations, and using this equation might not illustrate the exact picture of He-core WDs or other stars.
8. AST for WDs could be done for  $m_{F275W}$  brighter than 21 which would help provide a good estimate of WDs in NGC2808.

NGC2808 is a highly unusual globular cluster system and attaining the knowledge of its history and sub-stellar population could help our understanding of stellar evolution and globular cluster birth & evolution immensely, in general.

This page was intentionally left blank.

## Appendix A

# Sommerfeld's Free Electron Approximation

Consider  $n$  boxes in 3D. Each box is a cube of side length  $L$ . Writing periodic boundary conditions as Born-von Karman boundary conditions (Box normalization),

$$L_x = n_x \lambda \quad L_y = n_y \lambda \quad L_z = n_z \lambda$$

Each mode can be written as the following, where  $k_x$  is the wave number,

$$n_x \lambda = L_x \implies n_x = L_x \frac{k_x}{2\pi} \implies dn_x = L_x \frac{dk_x}{2\pi}$$

Hence, writing the total number of modes as,

$$dn = dn_x dn_y dn_z \implies dn = \frac{V dk_x dk_y dk_z}{8\pi^3} \implies \frac{dn}{V} = \frac{dk_x dk_y dk_z}{8\pi^3}$$

Assuming spherical symmetry,

$$\frac{dn}{V} = \frac{4\pi k^2 dk}{8\pi^3}$$

Writing  $\frac{dn}{V}$  as total number of modes per volume,

$$N(k) = \frac{4\pi k^2 dk}{8\pi^3}$$

To find the number of particles per volume occupying the momentum space, substituting  $p = \hbar k$  as,

$$N(k) = \frac{4\pi p^2 dp}{8\pi^3 \hbar^3}$$

$$N(k) = \frac{4\pi}{8\pi^3 \hbar^3} \int_0^{p_F} p^2 dp \implies N(k) = \frac{(2\pi)^3 p_F^3}{6\pi^2 \hbar^3} \implies N(k) = \frac{4\pi p_F^3}{3\hbar^3}$$

Since electron are fermions, two electrons can take the same state with opposite spin, and hence,

$$N(k) = \frac{8\pi p_F^3}{3\hbar^3} \quad (\text{A.1})$$

### Fermi Energy

Write definition: Fermi energy is the energy of the highest occupied state of degenerate matter. Hence, it is given by,

$$E_F = \frac{p_F^2}{2m} \quad (\text{A.2})$$

It can be written as,

$$E_F = \frac{(\hbar k_F)^2}{2m} \quad (\text{A.3})$$

Also,

$$N(k_F) = \frac{8\pi(\hbar k_F)^3}{3\hbar^3} \implies N(k_F) = \frac{8\pi \hbar^3 k_F^3}{8\pi^3 \cdot 3\hbar^3} \implies N(k_F) = \frac{k_F^3}{3\pi^2} \quad (\text{A.4})$$

Hence,

$$E_F = \frac{\hbar^2}{2m} (3\pi^2 N(k_F))^{2/3} \quad (A.5)$$

# Bibliography

- Althaus, L. G., Córscico, A. H., Isern, J., & García-Berro, E. 2010, *A&A Rev.*, **18**, 471
- Baumgardt, H. & Hilker, M. 2018, *MNRAS*, **478**, 1520
- Bedin, L. R., Salaris, M., Piotto, G., et al. 2008, *ApJ*, **678**, 1279
- Bellini, A., Anderson, J., Salaris, M., et al. 2013, *ApJ*, **769**, L32
- Blouin, S., Shaffer, N. R., Saumon, D., & Starrett, C. E. 2020, *ApJ*, **899**, 46
- Brown, T. M., Cassisi, S., D'Antona, F., et al. 2016, *ApJ*, **822**, 44
- Brown, T. M., Lanz, T., Sweigart, A. V., et al. 2012, *ApJ*, **748**, 85
- Brown, T. M., Sweigart, A. V., Lanz, T., Landsman, W. B., & Hubeny, I. 2001, *ApJ*, **562**, 368
- Calamida, A., Corsi, C. E., Bono, G., et al. 2008, *ApJ*, **673**, L29
- Cardelli, J. A., Clayton, G. C., & Mathis, J. S. 1989, *ApJ*, **345**, 245
- Carroll, B. W. & Ostlie, D. A. 1996, An Introduction to Modern Astrophysics
- Cassisi, S., Potekhin, A. Y., Pietrinferni, A., Catelan, M., & Salaris, M. 2007, *ApJ*, **661**, 1094
- Castellani, V., Calamida, A., Bono, G., et al. 2007, *ApJ*, **663**, 1021
- Chandrasekhar, S. 1984, *Rev. Mod. Phys.*, **56**, 137
- Chen, J., Ferraro, F. R., Cadelano, M., et al. 2022, *ApJ*, **934**, 93
- Chen, J., Ferraro, F. R., Cadelano, M., et al. 2021, *Nature Astronomy*, **5**, 1170
- Choudhuri, A. R. 2010, *Astrophysics for Physicists*
- Córscico, A. H., Althaus, L. G., Miller Bertolami, M. M., & Kepler, S. O. 2019, *The Astronomy and Astrophysics Review*, **27**, 7
- De Becker, A. 2020, An Analysis of the Red Giant Bump
- de Boer, T. J. L., Gieles, M., Balbinot, E., et al. 2019, *MNRAS*, **485**, 4906
- Gaia Collaboration, Helmi, A., van Leeuwen, F., et al. 2018, *A&A*, **616**, A12

- Harris, W. E. 1974, *ApJ*, 192, L161
- Harris, W. E. 2010, arXiv e-prints, arXiv:1012.3224
- Iben, I. & Webbink, R. F. 1989, in IAU Colloq. 114: White Dwarfs, ed. G. Wegner, Vol. 328, 477
- Kippenhahn, R., Weigert, A., & Weiss, A. 2012, Stellar structure and evolution, Astronomy and Astrophysics Library (Springer)
- McLaughlin, D. E. & van der Marel, R. P. 2005, *ApJS*, 161, 304
- Milone, A. P., Marino, A. F., Piotto, G., et al. 2015, *ApJ*, 808, 51
- Nardiello, D., Libralato, M., Piotto, G., et al. 2018, *Monthly Notices of the Royal Astronomical Society*, 481, 3382
- Pietrinferni, A., Hidalgo, S., Cassisi, S., et al. 2021, *ApJ*, 908, 102
- Piotto, G., Bedin, L. R., Anderson, J., et al. 2007, *ApJ*, 661, L53
- Piotto, G., Milone, A. P., Bedin, L. R., et al. 2015, *AJ*, 149, 91
- Prabhu, D. S., Subramaniam, A., & Sahu, S. 2021, *The Astrophysical Journal*, 908, 66
- Renzini, A. & Fusi Pecci, F. 1988, *ARA&A*, 26, 199
- Russell, H. N. 1914, Popular Astronomy, 22, 275
- Salaris, M. & Cassisi, S. 2005, Evolution of Stars and Stellar Populations
- Salaris, M., Cassisi, S., Pietrinferni, A., & Hidalgo, S. 2022, *MNRAS*, 509, 5197
- Salaris, M., Cassisi, S., & Weiss, A. 2002, *PASP*, 114, 375
- Sandquist, E. L. & Martel, A. R. 2007, *ApJ*, 654, L65
- Schlafly, E. F. & Finkbeiner, D. P. 2011, *ApJ*, 737, 103
- Shu, F. H. 1982, The Physical Universe
- Strickler, R. R., Cool, A. M., Anderson, J., et al. 2009, *The Astrophysical Journal*, 699, 40–55
- Trager, S. C., King, I. R., & Djorgovski, S. 1995, *AJ*, 109, 218
- Vasiliev, E. & Baumgardt, H. 2021, *MNRAS*, 505, 5978
- Webbink, R. F. 1975, *MNRAS*, 171, 555
- Winget, D. & Kepler, S. 2008, *Annual Review of Astronomy and Astrophysics*, 46, 157
- Woosley, S. E. & Heger, A. 2015, *The Astrophysical Journal*, 810, 34
- Zoccali, M. & Piotto, G. 2000, *A&A*, 358, 943